Microgrid Modeling, Planning and Operation

Wencong Su

Thesis submitted to the faculty of the Virginia Polytechnic Institute and State University in partial fulfillment of the requirements for the degree of

Master of Science

In

Electrical Engineering

Virgilio A. Centeno, Co-Chair

Yilu Liu, Co-Chair

Richard W. Conners

November 18th, 2009

Blacksburg, Virginia

Keywords: Distributed Generation, Microgird, MATLAB/SIMULINK, Simulation

Microgrid Modeling, Planning and Operation

Wencong Su

ABSTRACT

As distributed generations and renewable energy are becoming the fastest growing segment of the energy industry, the technical issues and environmental impacts have to be studied and understood. The large number of small-scale Microgrid components with their own characteristics is a big challenge for Microgrid modeling, simulation, planning and operation.

The major goal of this thesis is to build a library of various Microgrid components. First, the thesis is going to present a detailed description of Microgrid models with moderate complexity. Next, it will present the modeling of loads, utility grid and transmission lines. Then, the paper will discuss the distributed generation models that have been developed in Matlab/Simulink including Diesel Engine, Fuel Cell, Micro Gas Turbine, Wind Turbine, Photovoltaic Cell, along with the detailed modeling of short-term storage (Battery, Pumped Hydro Storage, Flywheel, and Supercapacitor). It will also discuss the hybrid sample systems that are built to investigate their transient responses.

To enhance the simulation performance, some improvements on modeling and simulation will be introduced as well. To accommodate the high demand of renewable energy and the environment policy, the planning and operation the of Micro-source generators has been studied using HOMER. Sensitivity variables are specified to examine the effect of uncertainties. Also, demand side management plays an important role in the operation of Microgrid. Case studies are carried out to investigate and validate the demand response methods. Finally, the philosophy for Microgrid protection, especially Time-delay overcurrent protection, will be briefly introduced in both gird-connected and islanding modes.

Dedication and Acknowledgements

This thesis is dedicated to the memory of my grandfather Yiwan Su (1925-2008). In my early years, he nurtured me with his great care and love. His strength during the last year of his life gave me a new appreciation for the meaning of family and love. Throughout my life, his authority as a role model in my heart has never being changed.

I would also like to thank my parents Hua Yu and Zhijiang Su for their never-ending encouragement, support, and unwavering love, which makes my dream come true. I also appreciate my other family members and all other friends for their love and support; and all other close ones, present and past, whose unconditional love make my journey possible.

I would like to express my sincere gratitude to my original academic advisor, Dr. Yilu Liu and current committee chairman, Dr. Virgilio Centeno, for helping me complete this research and write the master thesis. I will never forget all your contribution to my career, especially in internship hunting and PhD applications.

The members of my defense committee, Dr. Richard Conners, Dr. Virgilio Centeno, Dr. Yilu Liu, have generously given their time and expertise to refine my work. I thank all of them for their contribution and support.

I would also give my appreciation to my mentor Prof. Thomas Ortmeyer, who contributed the most to my growth and success in my undergraduate career at Clarkson University with the encouragement and emotional support.

I am also grateful for the support and advice from Jim Stoupis and Salman at USCRC ABB Inc. I would like to give special thanks to Dr. Le Tang. I really appreciate all your kind words to help me get through tough times. Especially you help me maintain positive attitude when I almost gave up.

I need to thank especially Zhiyong(Alan) Yuan for your special help, technical support and wise advice. I would like to thank all my friends and colleagues in FNET research group for the tremendous support they offered me in the course of my graduate study.

I am grateful to many people who shared their memories and experiences with me. Lastly, my special thanks go to my high school friends who encouraged my study and made valuable suggestions since 2001. Our friendship will remain forever.

List of Figures

List of Tables

Chapter 1
Introduction to Microgrid

1.1 Motivations

Economic, technology and environmental incentives are changing the features of electricity generation and transmission. Centralized generating facilities are converging to smaller and more distributed generation partially in the purpose of deducing the loss from traditional economies of scale. Distributed generation encompasses a wide range of prime mover technologies, such as internal combustion (IC) engines, gas turbines, microturbines, photovoltaic, fuel cells and wind-power. These emerging technologies have the potential to have lower cost negating traditional economies of scale. The applications include power support at substations, deferral of T&D upgrades and onsite generation [1]. Small-scale generators typically are located at users' sites where the energy they generate is used to meet growing customer needs of higher reliability and power quality. Since the local loads are close to distributed generators, sometimes even in the same building, the waste heat can be used in addition to electrical energy. Most existing power plants are central or distributed power plants. They deliver electricity to user sites at an overall fuel-to-electricity efficiency in the range of 28-32%. This represents a loss of around 70% of the primary energy provided from the generator. There are a couple ways to reduce this energy loss: increase the fuel-to-electricity efficiency of the generation plant and/or use the waste heat [1]. The growing need of reducing Carbon emissions makes the concept of Microgrid more attractive. Microgrid has the ability to reduce emissions compared to centralized utility systems. Many countries and research groups have involved in Microgrid projects.

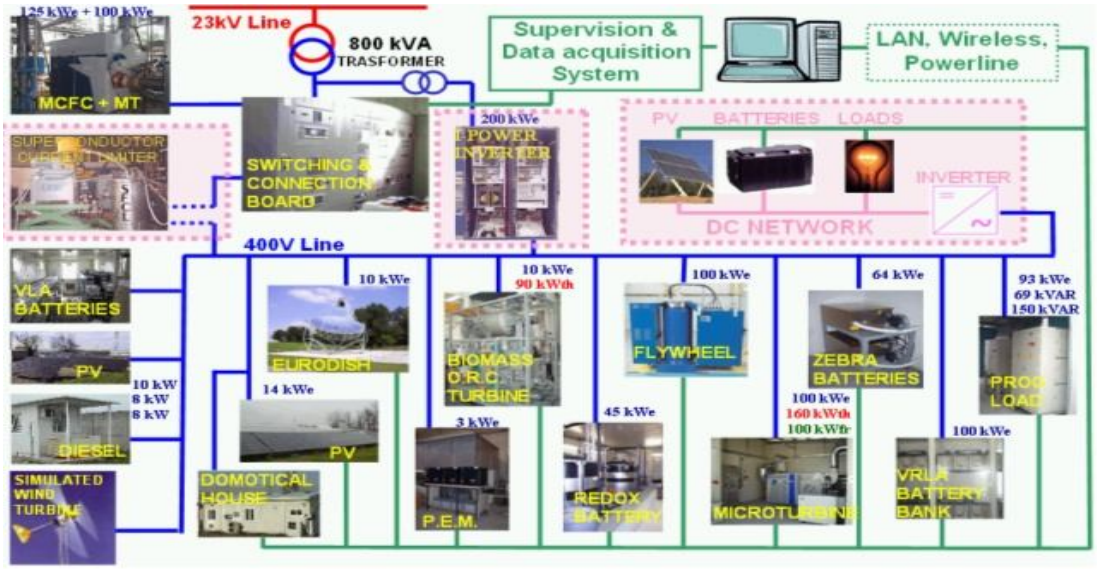

Figure 1-1. CESI RICERCA DER test facility [2]

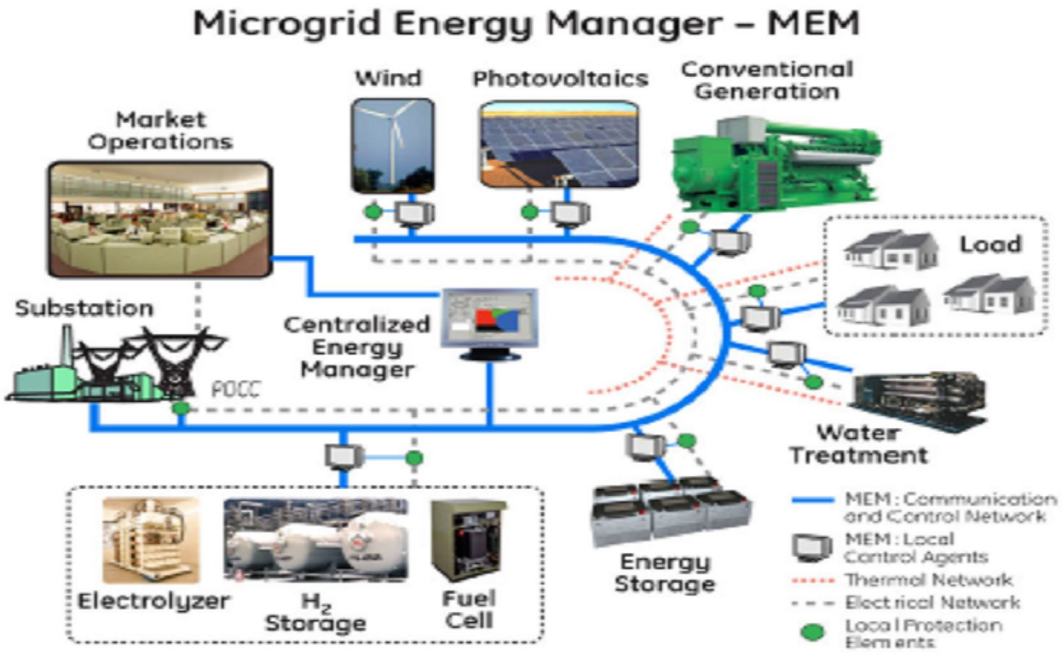

Figure 1-2. GE Microgrid demo [3]

1.2 Definition

A Microgrid could be defined as a low-voltage distribution network with distributed energy sources altogether with storage devices and loads. Generally speaking, Microgrid could

be operated in either grid-connected or islanding mode. A typical Microgrid architecture diagram is illustrated in Figure 1-3. In reference [4], the Microgrid structure assumes an aggregation of loads and microsources operating as a single system providing both power and heat. The majority of the microsources must be power electronic based to provide the required flexibility to insure controlled operation as a single aggregated system. This control flexibility allows the Microgrid to present itself to the bulk power system as a single controlled unit, have plug-and-play simplicity for each microsource, and meet the customers' local needs. There are a cluster of radial feeders in the basic Microgrid architecture. The connection point to utility grid is called point of common coupling (Lasseter 2002). Critical loads on feeders A-B require local generation (diesel generator, PV cell, wind turbine, Micro-turbine and fuel cell etc).

As local control of distributed generations dominate in power system, the conventional central dispatch is not necessary. During disturbances, the static switch is able to autonomously separate the subsystem from the distribution system to isolate the microgrid from the disturbance without harming the transmission grid's integrity. As you can see in Figure 1-3, feeders A-B can switch to off-grid mode using the static switch. The non-critical loads on feeder C can only be supported in grid-connected mode. The static switch recloses immediately after the fault is cleared. The size of emerging generation technologies permits generators to be placed optimally in relation to heat loads allow for use of waste heat [1].

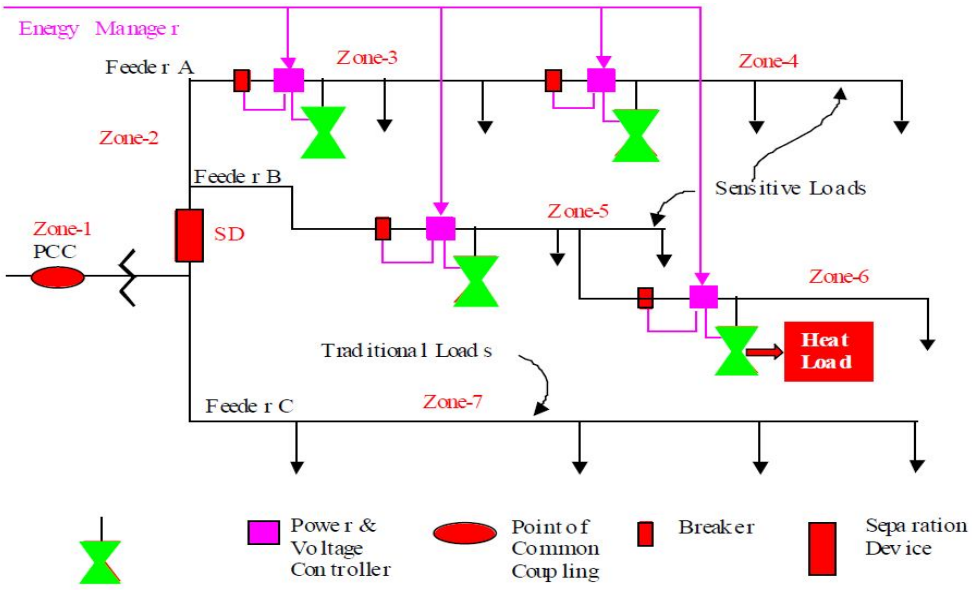

Figure 1-3. Microgrid architecture diagram [4]

1.3 Scope of Work

The subsequent content is structured as follows:

Chapter 2: Microgrid Modeling. The electric power system is an enabling infrastructure that supports the continuous operation of various mission critical facilities, both at the component and the systems levels. At present, there is a need to build an extensive library of Microgrid components in the standard simulation environment. This involves the development of adequate models for simulation the operation of a variety of distributed generators (Diesel Engine, Fuel Cell, Micro Gas Turbine, Wind Turbine, Photovoltaic Cell) and short-term storage (Battery, Pumped Hydro Storage, Flywheel, and Supercapacitor), including the corresponding control and power electronic interface. The thesis also compares the characteristics of different technologies for providing local generation and energy storage, along with the modeling of loads, utility grid and transmission lines. Dynamics loads are modeled as well as constant electrical loads. PI lines are typically adapted for Microgrid simulation for some reasons. A generic model with moderate complexity is preferable to enable the integration of control and protection strategies. The Matlab/Simulink models of each Microgrid component are able to describe their steady-state and dynamic behaviors. Finally a simulation platform is developed to simulate the steady-state and dynamic operation of Microgrid. In addition to study individual Microgrid component, the hybrid sample systems are built to analyze their transient responses to disturbance or configuration change. Several case studies are carried out to perform the testing evaluation of the developed simulation platform.

Chapter 3: Improvement on Microgrid Modeling and Simulation. This chapter will introduce some improvements on modeling and simulation to enhance the simulation performance. For example, the selected models are modified to fit a real-time simulator, which can run Simulink model down to 5 us. The interface developed between Matlab/Simulink and PSS/E allows the models to be used directly in PSS/E dynamic simulation. The developed models might be co-simulated by PLECS and Matlab/Simulink to reduce the running time. In addition, it is possible to include the thermal design with the electrical design. Many other benefits will also be presented in the chapter and will be implemented in future work.

Chapter 4: Microgrid Planning. HOMER is applied to study the planning and operation of Micro-source generators to accommodate the high demand of renewable energy and the

environmental requirement. Simulation results show a case study of an optimal microgrid configuration on Ontario area in Canada. Sensitivity variables are specified to examine the effect of uncertainties (e.g. diesel price and average wind speed), especially in a long-term planning. HOMER allows the modeler to compare many different design options based on their technical and economic merits. Many other factors have been taken into consideration such as the cost of Carbon emissions and thermal energy onsite when combined heat and power (CHP) is employed. The effect of air emission penalties on Microgrid planning is also well presented.

Chapter 5: Demand Side Management. Demand side management is playing an important role in the operation of Microgrid. It is obvious from RTP schedule that the customers get financial benefit as long as the load demand is flexible. Utilities also get financial benefit by cutting down the extremely high generating cost in the peak period. In other words, the load demand at the peak period declines significantly so as to reduce the generating cost. Accordingly, the power system reliability will be improved as well. Based on raw data from Ontario area, case studies are carried out to analyze and validate the demand response methods.

Chapter 6: Protection in Microgrid. Technical challenges can reduce the operating efficiency and the significant benefits Microgrid brings to us. Microgrid protection is considered as one of important issues that has to be addressed. Finally, Chapter 6 will briefly introduce the philosophy for Microgrid protection, especially Time-delay overcurrent protection in both gird-connected and islanding modes.

Chapter 2
Microgrid Modeling

2.1 Introduction

This chapter discusses the detailed modeling of Microgrid components. Typical power sources, loads, and transimision lines have been modeled individually and tested well in MATLAB/SIMULINK. And then a variouty of Microgrid models are selected to build combined systems. Both the steady-state condition and dynamic behavior will be analyzed in more details.

There are many types of renewable energy. Wind power is the conversion of wind energy into electrical energy using wind turbines. In a wind farm, individual turbines are interconnected with a medium voltage (usually 34.5 kV) power collection system and communications network. Then large-scale wind farms are connected to the power grid. The total amount of economically extractable power available from the wind is considerably more than present human power use from all sources [5]. An estimated 72TW of wind power on the Earth potentially can be commercially viable [6]. Hydroelectricity is electricity generated by the production of power through use of the gravitational force of falling or flowing water. It is the most widely used form of renewable energy. Solar energy is the radiant light and heat from the sun. Solar power provides electrical generation by means of heat engines or photovoltaic.

A detailed of description of Microgrid models with moderate complexity will be presented in this chapter. First of all, a list of DG models, short-term storage models, load models, utility grid model and transmission line models is given as below.

Load and Utility Grid:

- Utility grid
- Three phase constant/dynamic load

Transmission Line:

Distributed Generators:

- Photovoltaic Cell (PV Cell)

- Micro Gas Turbine
- Diesel Generator
- Wind Turbine
- Fuel Cell

Short-term Storage:

- Flywheel
- Pumped Hydro Storage
- Battery Storage
- Supercapacitor

2.2 Load and Utility Grid Modeling

The utility grid is modeled as a 3 phase ideal voltage source with infinite power rate. This simplified model is only used for analyzing the dynamic behavior of the proposed systems. A 120kV utility grid model is shown in Figure 2-1. The models of three dynamic load and three phase fixed load with constant impedances are available in the standard SimPowerSystems library. The active power and reactive power can be controlled via the external control signals. It is especially useful when the demand response or demand side management is taken into account, which is included in next chapter. The application of one phase load will not be covered in my Thesis.

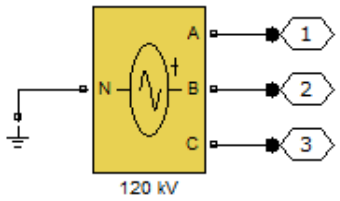

Figure 2-1. 120kV utility grid model in Matlab/Simulink

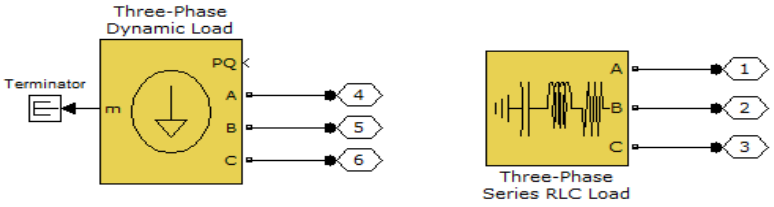

Figure 2-2. Three phase load model in Matlab/Simulink

2.3 Transmission Line Modeling

In the simulation, most transmission lines are represented by the three phase PI section line model which is available in the standard SimPowerSystems library. The three phase PI section line model is chosen to implement a balanced three-phase transmission line model with parameters lumped in a PI section. On contrary to the distributed parameter line model where the resistance, inductance, and capacitance are uniformly distributed along the line, the Three-Phase PI Section Line block lumps the line parameters in a single PI section. The three phase PI section line model is shown in Figure 2-3.

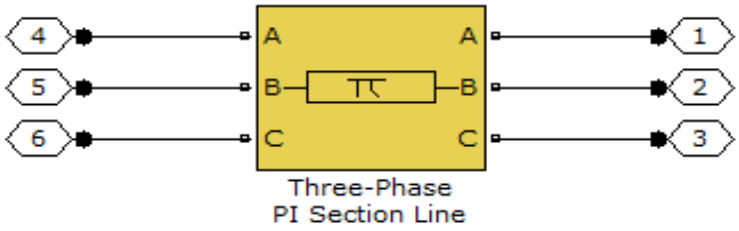

Figure 2-3. Three phase PI section line model in Matlab/Simulink

2.4 DG Modeling

2.4.1 Photovoltaic Cell (PV Cell)

The simplest model can be considered as a diode. When exposed to light, the electrons and holes are separated when the photos energy is greater than the band gap energy. Under the influence of the electric field of the p-n junction diode, the electrons and holes flow through an external circuit. Finally, the light energy can be converted into the electrical energy.

The behavior of photovoltaic (PV) cells can be modeled with an equivalent circuit shown in Figure 2-4 (Duffie and Beckman, 1991). The letter “V” represents the voltage at the load. The accurate PV model is presented based on 5-Parameter or 4-Parameter equations. The basic model includes a photocurrent source, a single diode junction and a series resistance and a shunt resistance. It has to be mentioned here the shunt resistance in parallel with the diode is ignored in 4-parameter model.

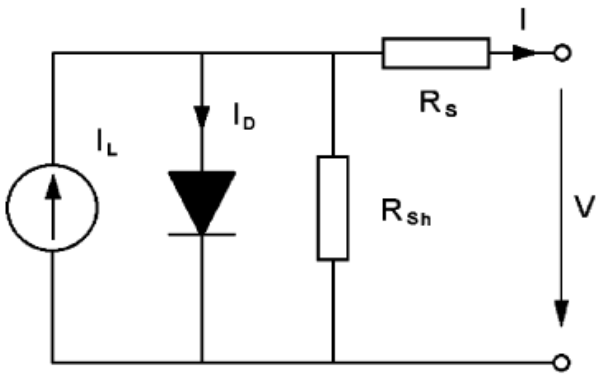

Figure 2-4. Equivalent circuit of PV cells

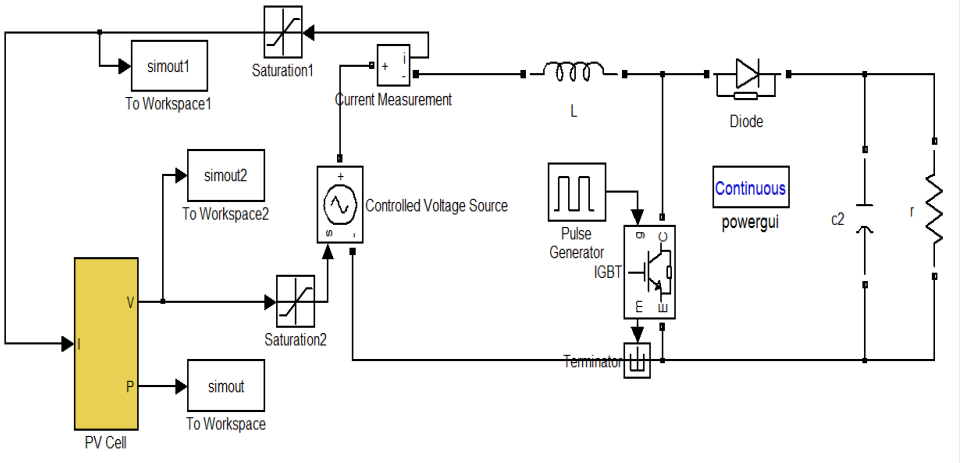

Figure 2-5. PV cell Simulink model

The equations which describe the characteristics of PV cell are presented below. The corresponding Matlab/Simulink model of the PV cell is shown in Figure 2-5. the implementation of these equations in Matlab/Simulink is really straightforward. Thus the details of Simulink modeling will not be discussed in more details. Current I is described as:

$$I = I_L - I_D \times (e^{\frac{V+I\times R_S}{n\times V_{th}}} - 1) - \frac{V + I \times R_S}{R_{Sh}} \qquad (2.1)$$

Where I_L is the photocurrent; I_D is the reverse saturation current of the equivalent diode; R_S and R_{Sh} are the series and shunt resistances of the PV cell, respectively; and n is the diode quality factor. V_{th} is the temperature dependent thermal voltage given by

$$V_{th} = \frac{K \times T}{q} \qquad (2.2)$$

Where V_{th} is temperature dependent variable; the Boltzmann constant K is $1.3806\times10^{-23}\,J/K$; T is the operating temperature in Kelvin degrees; the electron charge q is $1.6022\times10^{-19}\,C$.

$$I_L = \frac{G_T}{G_{T,ref}} \times \left[I_{L,ref} + \mu_{I_{sc}} \times (T_C - T_{C,ref}) \right] \tag{2.3}$$

Where G_T is the actual irradiance; $G_{T,ref}$ is the reference irradiance; $\mu_{I_{sc}}$ is the temperature coefficient for short circuit current; T_C is the operating temperature; and $T_{C,ref}$ is the reference temperature.

$$I_D = I_{D,ref} \times (\frac{T_C}{T_{C,ref}})^3 \times e^{\frac{-q\theta}{nK}(\frac{1}{T_C} - \frac{1}{T_{C,ref}})} \tag{2.4}$$

Band gap energy θ is assumed as 1.12eV in this case.

For modeling the modules under non-standard conditions, the series and shunt resistances have to be taken care. These values are not provided by manufactures. They are not easy to estimated with enough accuracy. The shunt resistance R_{Sh} controls the slope of the I-V curve at short circuit condition. R_S gives a more accurate shape between the maximum power point and the open circuit voltage. According to Equation (2.1), the derivative of current with respect to voltage is

$$\frac{dI}{dV} = -\frac{I_D e^{\frac{V+IR_S}{nKT/q}} + \frac{1}{R_{Sh}}}{1 + \frac{R_S}{R_{Sh}} + \frac{R_S I_D q}{nKT} e^{\frac{V+IR_S}{nKT/q}}} \tag{2.5}$$

The Equations (2.1) and (2.5) are recurrence equations. The current is dependent on several variables such as voltage, irradiation, temperature, etc. As a result, each term of the equation is defined as a function of the preceding terms. The Newton-Raphson method is used here. It is perhaps the best known method for finding successively better approximations to the zeroes of a real-valued function. Newton's method can often converge remarkably quickly, especially if the iteration begins with a good initial guess. Newton's method involves the idea of an error in a function $f(I)$ being driven to zero by making adjustments ΔI to the independent variable associated with the function. This is discussed in detail below. Unfortunately, when

iteration begins far from the desired root, Newton's method can easily lead an unwary user astray with little warning. Thus, good implementations of the method embed it in a routine that also detects and perhaps overcomes possible convergence failures.

In Newton's methods, I pick up a starting point of I which is the initial guess of I.

$$f(I) = 0 \tag{2.6}$$

Then we use a Taylor expansion of the function of I

$$0 = f(I_0 + h) = f(I_0) + hf'(I_0) + \frac{h^2}{2} f''(I_0) + H.O.T. \tag{2.7}$$

Where H.O.T. stands for higher order terms. The term h is usually pretty small. Thus $\frac{h^2}{2} f''(I_0) \approx 0$, then

$$I_1 = I_0 - \frac{f(I_0)}{f'(I_0)} \tag{2.8}$$

Then compute successively more accurate estimates of the x until the error between the last two estimations is less than the pre-defined tolerance. In the Matlab/Simulink model, the equation can solved using Newton-Raphson method.

The following simulation was performed to model BP MSX 60 PV cells with specification shown in Table 2-1.

Table 2-1. BP MSX60 Specification [7]

	BP MSX 60	BP MSX 64[4]
Maximum power (P_{max})[2]	60W	64W
Voltage at P_{max} (V_{mp})	17.1V	17.5V
Current at P_{max} (I_{mp})	3.5A	3.66A
Minimum P_{max}	58W	62W
Short-circuit current (I_{sc})	3.8A	4.0A
Open-circuit voltage (V_{oc})	21.1V	21.3V
Temperature coefficient of I_{sc}	(0.065±0.015)%/°C	
Temperature coefficient of V_{oc}	-(80±10)mV/°C	
Temperature coefficient of power	-(0.5±0.05)%/°C	
NOCT[3]	47±2°C	
Maximum system voltage	600V (U.S. NEC rating) 1000V (TÜV Rheinland rating)	
Maximum series fuse rating	20A	

The P-V curve and I-V currve with various irradiance at SRC are shown in Figures 2-6 and 2-7, respectively. At the maximum power point, the maximum power is gained from the PV cell. At a lower irradiation, the maximum power of PV cell decreases by a large amount. The

short-circuit current decreases, while the open-circuit voltage does not change too much.

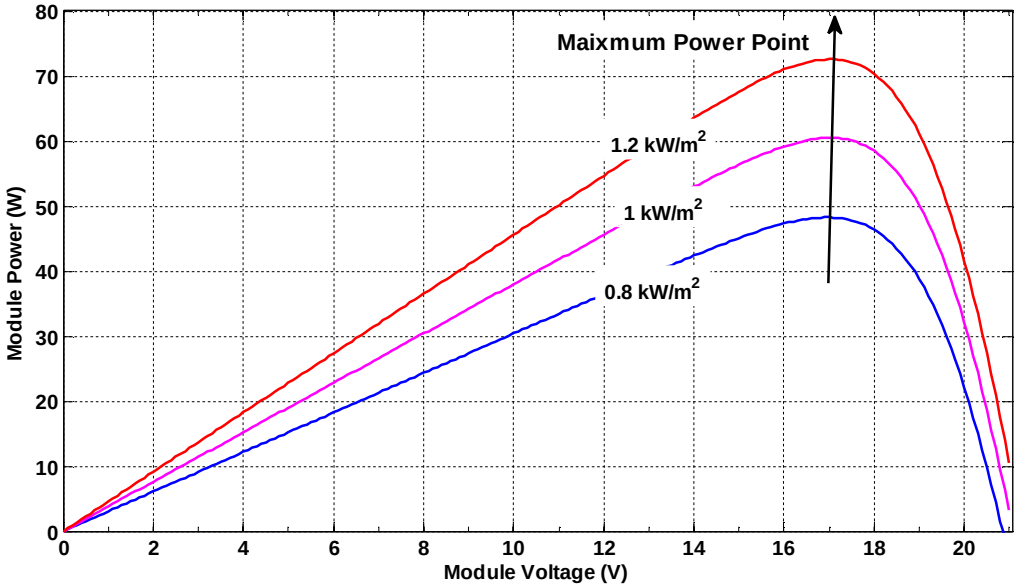

Figure 2-6. P-V curve of BP MSX60 PV cell at 298K

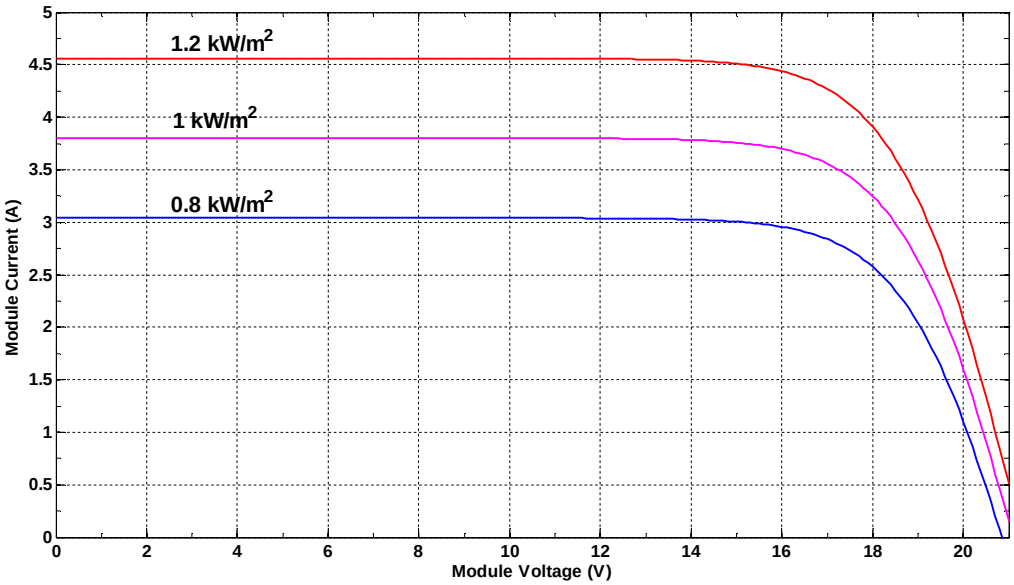

Figure 2-7. I-V curve of BP MSX60 PV cell at 298K

However, the open circuit voltage is much more sensitive to the temperature. Figures 2-8 and 2-9 show P-V and I-V characteristics with various temperature at the standard irradiation. At a higher temperature, the open-circuit voltage decreases significantly.

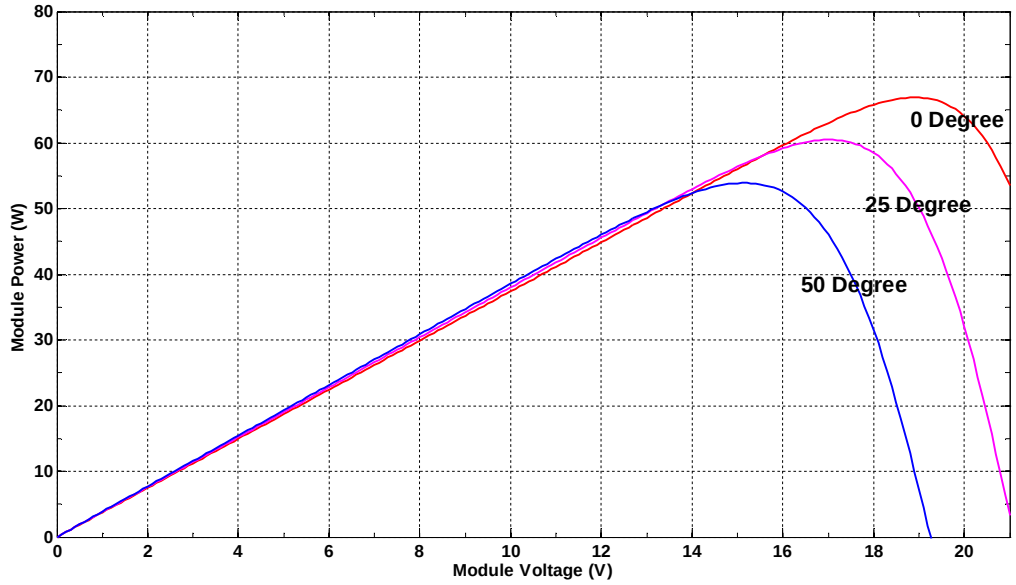

Figure 2-8. P-V curve of BP MSX60 PV cell at the standard irradiation

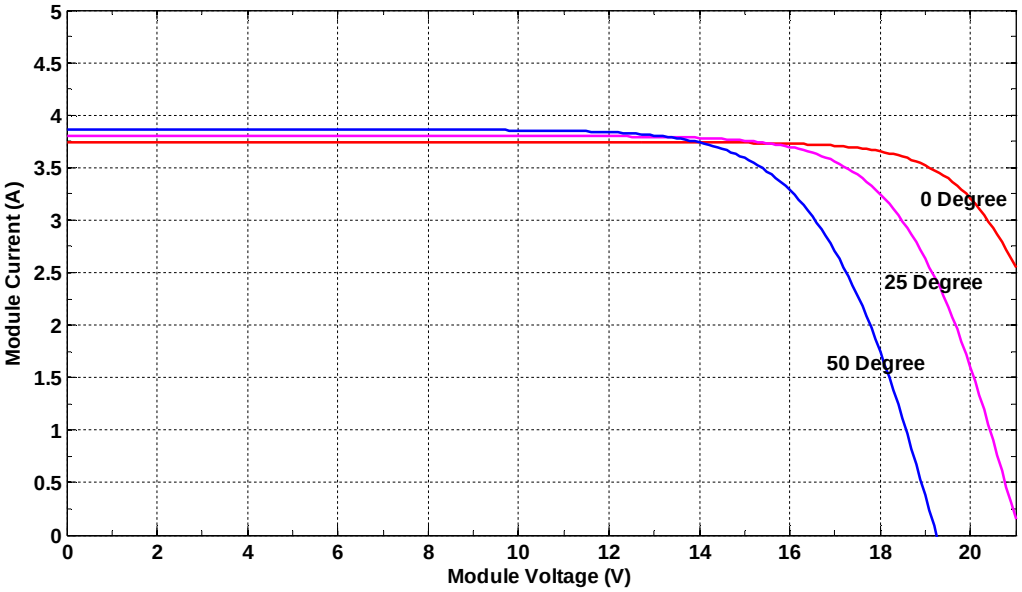

Figure 2-9. I-V curve of BP MSX60 PV cell at the standard irradiation

In 4-parameter model, a series resistance R_S is used but not a shunt resistance R_{Sh}. Although the model does not include the shunt resistance, the model is carried out by means of equations below that have a good approximation to a real device. Assuming an infinite value for the shunt resistance R_{Sh}, the 5-Parameter model is reduced to a 4-Parameter model. An alternate

equation for calculating *aref* is presented by Duffie and Beckman (1991) using the results of an analysis by Townsend. But it has to be mentioned that this equation is only valid when the shunt resistance R_{Sh} is assumed to infinite.

$$I_{L,ref} = I_{SC,ref} \tag{2.9}$$

$$a_{ref} = \frac{\mu_{V_{OC}} T_{C,ref} - V_{OC,ref} + \theta N_S}{\frac{\mu_{I_{SC}} T_{C,ref}}{I_{L,ref}} - 3} \tag{2.10}$$

$$a = a_{ref} \frac{T_C}{T_{C,ref}} \tag{2.11}$$

$$R_S = \frac{a_{ref} ln(1 - \frac{I_{MP}}{I_L}) - V_{MP} + V_{OC}}{I_{MP}} \tag{2.12}$$

Where $I_{L,ref}$ is the light current at SRC; $I_{SC,ref}$ is the short circuit current at SRC; a_{ref} is the ideality factor parameter at SRC; a is the ideality factor parameter; $\mu_{V_{OC}}$ is the temperature coefficient for open circuit voltage; N_S is the number of cells; I_{MP} is the current at maximum power point; and V_{MP} is the voltage at maximum power point. The ideality factor is a linear function of the cell temperature.

Another PV module is carried out with good performance. The data for Siemens Bin1/SP75 is used in the simulation to show the shapes of the P-V curves in Figures 2-10 and 2-12 and V-I curves in Figures 2-11 and 2-13 under various temperature and irradiation conditions.

Table 2-2. Specifications Siemens Bin1/SP75 PV cells provided by NIST [8]

Type of Cell	Astropower Apex Bin G/APX-90	Siemens Bin1/SP75 (average of 2)	Solarex MegaCell/MSX-64 (1997)	Uni-Solar US-64 Module (average of 3)
At Reference Conditions				
P_{mp0} (W)	103.96	133.40	125.78	57.04
I_{sc0} (A)	5.11	4.37	4.25	4.44
V_{oc0} (V)	29.61	42.93	41.50	23.16
I_{mp0} (A)	4.49	3.96	3.82	3.61
V_{mp0}(V)	23.17	33.68	32.94	16.04
NOCT (K)	316.15	316.85	316.45	311.05
NOCT (Ins) (K)	337.85	340.05	338.55	328.45
Temp. Coefficients				
α_{Isc} (A/°C)	0.00468	0.00175	0.00238	0.00561
α_{Isc} (1/°C)	0.000916	0.000401	0.000560	0.001263
α_{Imp} (A/°C)	0.00160	-0.00154	0.00018	0.00735
α_{Imp} (1/°C)	0.000358	-0.000390	0.000047	0.002034
β_{Voc} (V/°C)	-0.12995	-0.15237	-0.15280	-0.09310
β_{Voc} (1/°C)	-0.004388	-0.003549	-0.003682	-0.004021
β_{Vmp} (V/°C)	-0.13039	-0.15358	-0.15912	-0.04773
β_{Vmp} (1/°C)	-0.005629	-0.004560	-0.004830	-0.002976
Sandia National Lab Parameters				
a_0	0.938110	0.935823	0.918093	1.10044085
a_1	0.062191	0.054289	0.086257	-0.06142323
a_2	-0.015021	-0.008677	-0.024459	-0.00442732
a_3	0.001217	0.000527	0.002816	0.000631504
a_4	-0.000034	-0.000011	-0.000126	-1.9184E-05
b_0	0.998980	1.000341	0.998515	1.001845
b_1	-0.006098	-0.005557	-0.012122	-0.005648
b_2	8.117E-04	6.553E-04	1.440E-03	7.25E-04
b_3	-3.376E-05	-2.730E-05	-5.576E-05	-2.916E-05
b_4	5.647E-07	4.641E-07	8.779E-07	4.696E-07
b_5	-3.371E-09	-2.806E-09	-4.919E-09	-2.739E-09
C_0	0.9615	0.9995	1.0144	1.072
C_1	0.0368	0.0026	-0.0055	-0.098
C_2	0.2322	-0.5385	-0.3211	-1.8457
C_3	-9.4295	-21.4078	-30.2010	-5.1762
n	1.357	1.026	1.025	3.09
OTHER Parameters				
N_s	56	72	72	66
Slope at I_{sc} (A/V)	-0.008	-0.004	-0.003	-0.020
ε (eV)	1.12	1.12	1.14	1.6

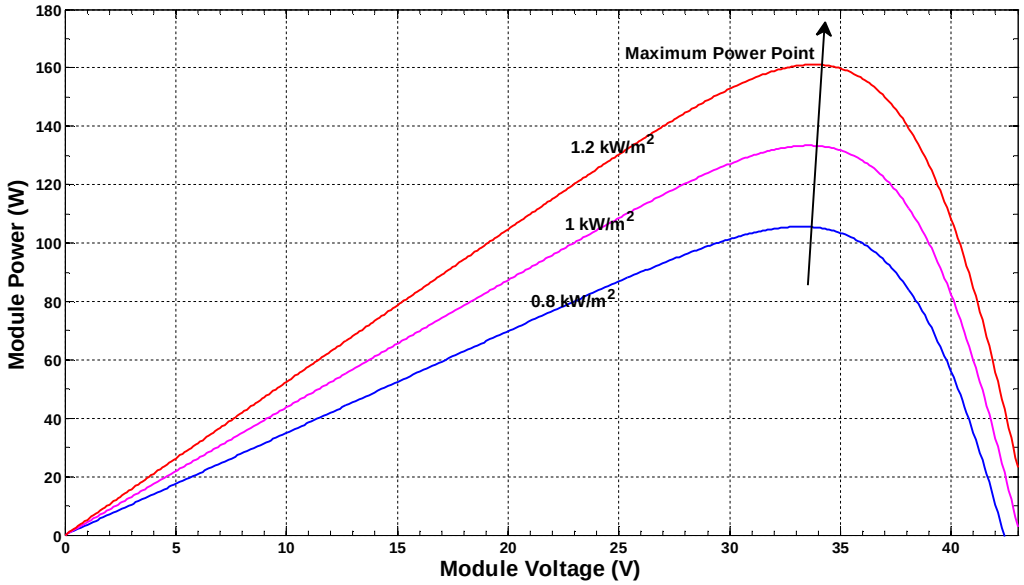

Figure 2-10. P-V curve of Siemens Bin1/SP75 PV cell at 298K

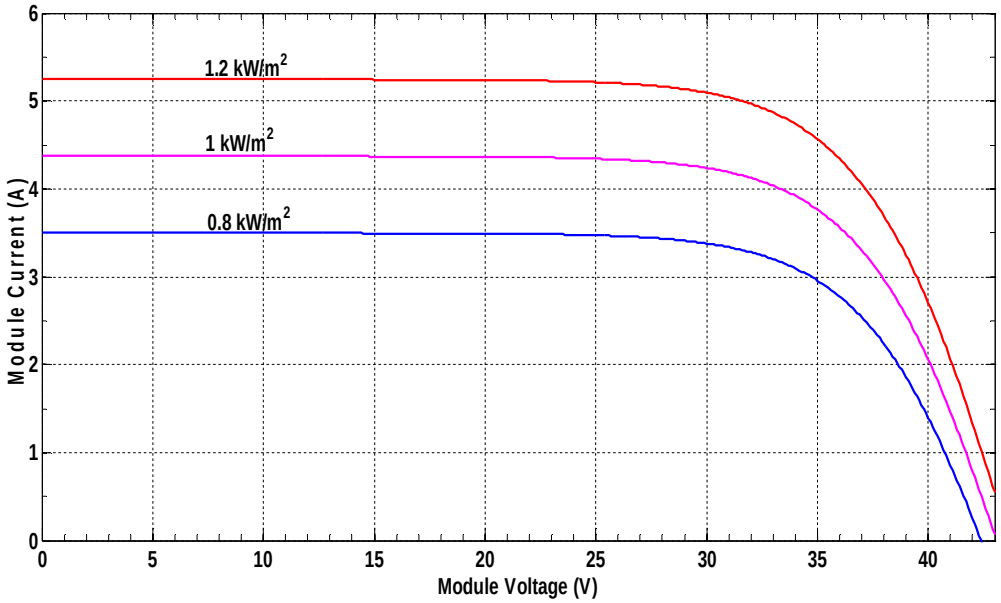

Figure 2-11. I-V curve of Siemens Bin1/SP75 PV cell at 298K

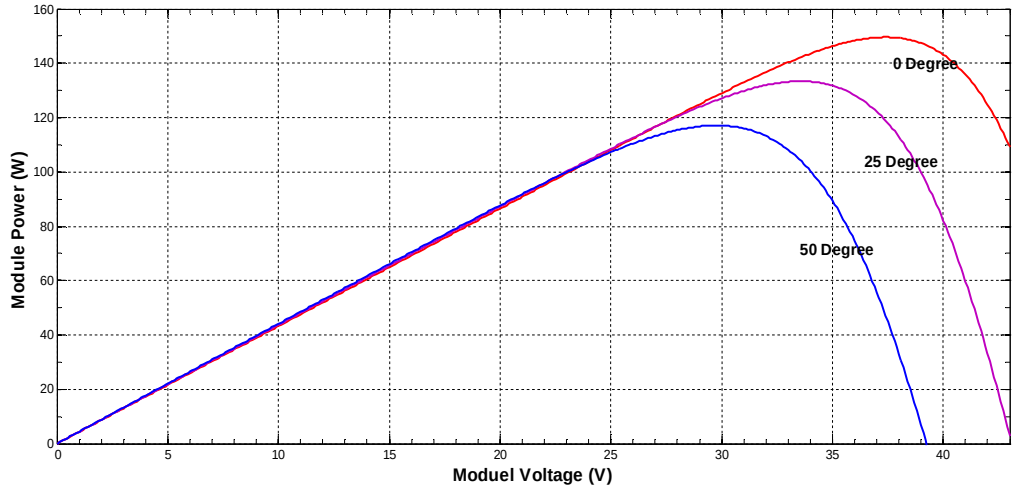

Figure 2-12. P-V curve of Siemens Bin1/SP75 PV cell at the standard irradiation

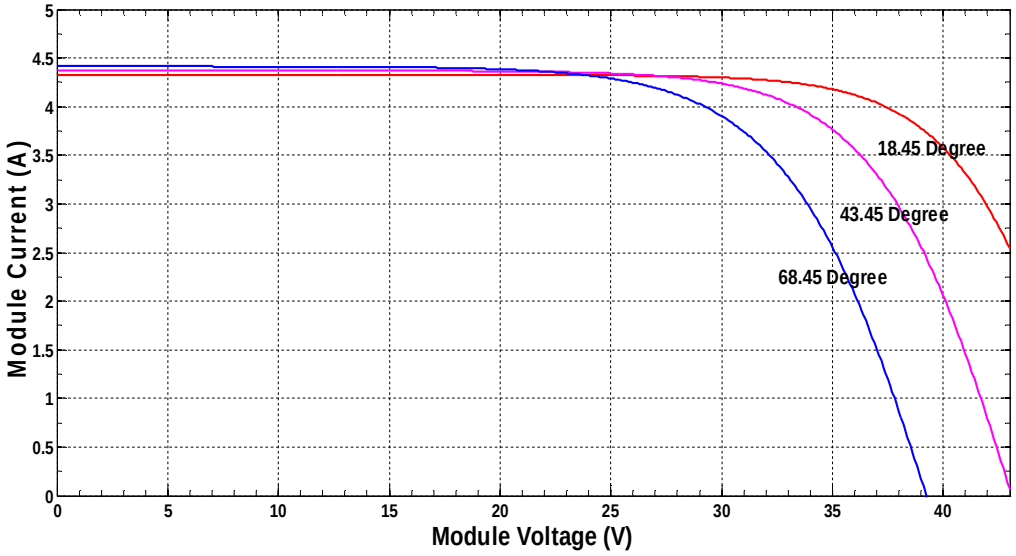

Figure 2-13. I-V curve of Siemens Bin1/SP75 PV cell at the standard irradiation

The simulation results show the excellent correspondence with the manufacture data. Also given different conditions of temperature and irradiation, the feasibility of the final models of moderate complexity has been studied. In addition, these models are used to analyze the temperature and irradiation effect on the maximum power point.

2.4.2 Diesel Generator

Diesel engines, developed more than 100 years ago, were the first generation among distributes generator technologies. The aim of the speed governor is to adjust the fuel flow in order to control the output torque and then regulate the desired power to meet the load demand. there are many methods already proposed for diesel generator modeling [9-12]. In the view of the control system, a diesel engine can be considered as a speed-feedback system.

The fuel actuator system is usually represented as a first order phase-lag sector, which is characterized by a gain K_2, the current driver constant K_3 and a time constant τ_2. The output of the actuator is the fuel flow $\Phi(s)$. while the input is the current $I(s)$. Typically K_2 and K_3 are considered to be constant values for a specific diesel engine. K_3 determines the amount of the mechanical torque obtained from per unit of fuel flow. The time constant τ_2 depends on the temperature of the oil flowing into the actuator.

$$\Phi(s) = \frac{K_2 K_3}{(1+\tau_2 s)} I(s) \tag{2.13}$$

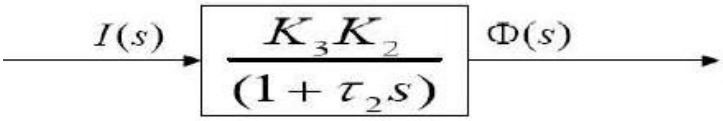

Figure 2-14. Transfer function of the actuator model in diesel engine

Then the fuel flow $\Phi(s)$ is converted into mechanical torque T(s) with a time delay τ_1 and an engine torque constant K_1.

$$T(s) = \Phi(s) K_1 e^{-\tau_1 s} \tag{2.14}$$

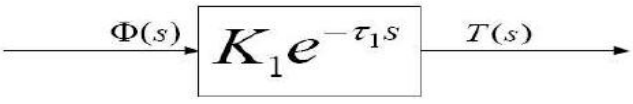

Figure 2-15. Transfer function of the engine model in diesel engine

The flywheel represents the complex dynamic effects of the engine inertia, the angular speed ω_W, the viscous friction coefficient ρ and the loaded alternator. The model is assumed to

have an integrator with flywheel acceleration constant J which serves to filter out a large proportion of the disturbance and noise. The noise itself is an inherent property of all internal combustion engines. As proposed in [10], an integrator is added between the reference signal *r* and the engine actuator. It is necessary to eliminate the speed droop in the steady-state operation by raising the order of the whole system. The typical set of per unit values are used in the simulation which is taken from [10].

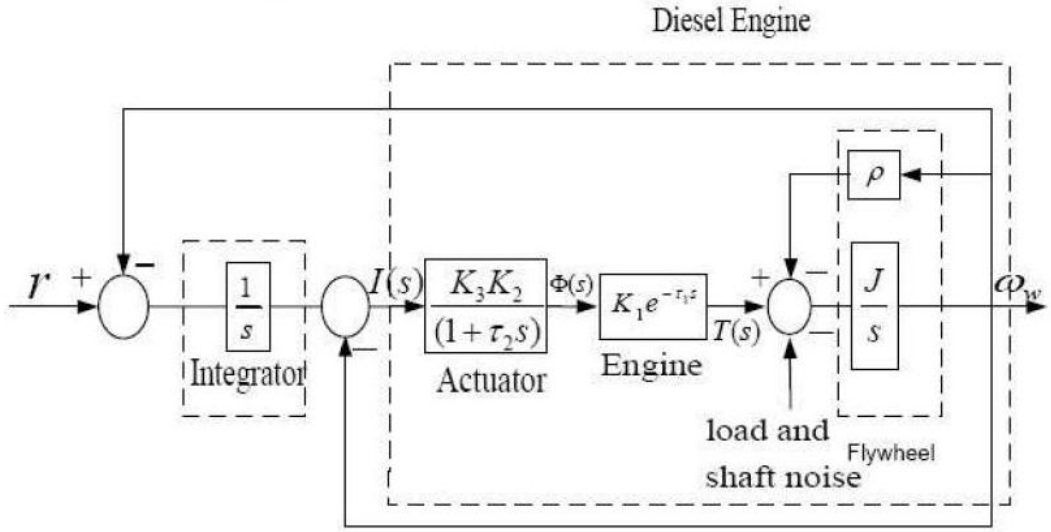

Figure 2-16. The block diagram of the diesel engine system

To sum up, the general structure of the fuel actuator system is usually represented as a first order phase-lag network. The output of the actuator, the fuel-flow, is then converted into mechanical torque after a pure time delay. In reference [13], the operation of diesel engine-driven wound-field synchronous generator sets as distributed generators is studied in more details. A new controller for the genset is proposed to alleviate these problems and enable the various sources to share power and maintain power quality within the system.

2.4.3 Micro Gas Turbine

Micro Gas Turbine can have many positive impacts on the operation of power systems. Detailed modeling of Micro Gas Turbine (MTG) helps us fully understand its own characteristics and dynamic behavior. The final model built in Matlab/Simulink is composed of a permanent magnet synchronous generator and a micro gas turbine which both are compatible with the power electronic controls. One of the significant benefits MTG could bring us is that it can start

very quickly at the peak load period to remedy the demand constraint. In addition, the combined heat and power (CCHP) system is able to reuse the waste heat.

There are basically two types of MTG: a high-speed single shaft model and a split shaft model. In a single shaft model, the compressor and a turbine are mounted on the same shaft. It can operate at a very high speed which can be converted into 50Hz or 60Hz voltage using AC-DC rectifier and DC-AC inverter. In a spilt shaft model, a power turbine turns a compressor on one shaft and a turbine on another shaft rotates a induction generator via a gearbox. In this section, the non-linear MTG model developed in Matlab/Simulink can simulate the basic dynamic behavior of a single shaft micro-turbine generator. The power electronic interface between MTG and three phase AC load is required. The basic MTG configuration is shown in Figure 2-17.

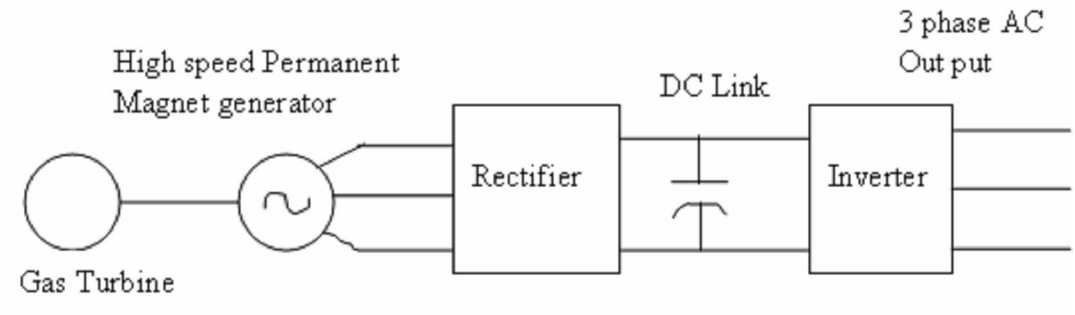

Figure 2-17. The block diagram of Micro-turbine generation system [14]

MGT model consists of temperature control, fuel control, and speed governor and acceleration control systems [15-16].

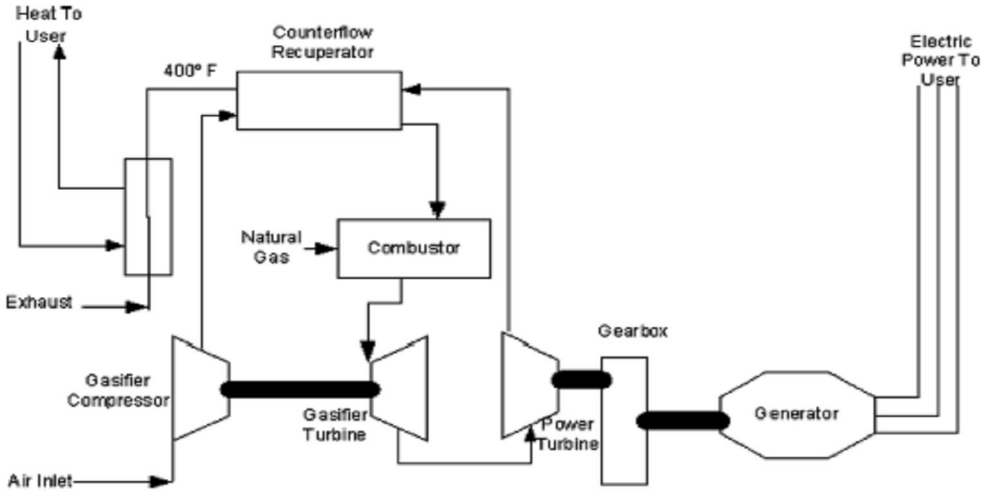

Figure 2-18. The block diagram of a split-shaft MGT

The speed control operates on the speed error between a reference speed and the MGT rotor speed. It is the primary control part of the Micro turbine. A lead-lag transfer function has been used to represent the speed controller [15-16]. The block diagram of the speed controller is shown in Figure 2-19. And the corresponding Matlab/Simulink model is shown in Figure 2-20.

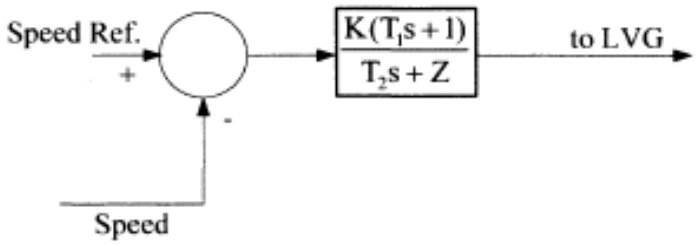

Figure 2-19. The block diagram of the speed controller in MGT

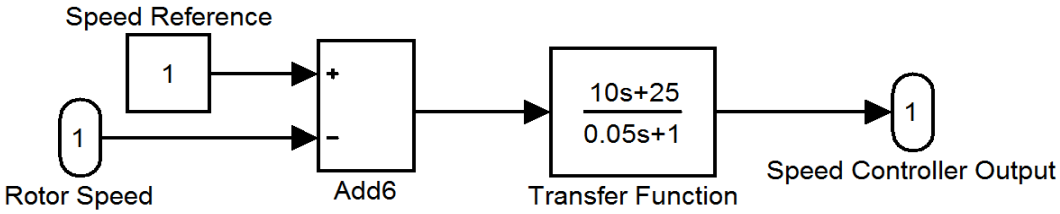

Figure 2-20. The Simulink implementation of the speed controller in MGT

The acceleration controller is used during turbine startup to limit the rate of the rotor acceleration prior to reaching the operating point. If the operating speed is close to its rated speed, the acceleration control could be eliminated. The Matlab/Simulink implementation is illustrated in Figure 2-21.

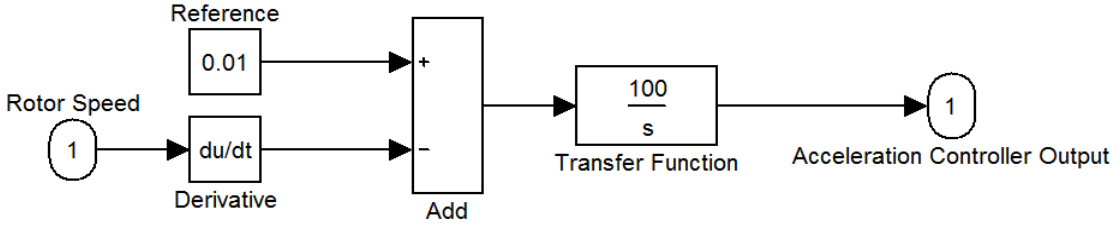

Figure 2-21. The Simulink implementation of the acceleration controller in MGT

The fuel flow burned in the combustor results in the turbine torque and the exhaust gas temperature is measured by a thermocouple. The output from the thermocouple is compared with

a reference value. Normally the reference value is much higher than the measured value. The block diagram of the temperature controller is shown in Figure 2-22. And the temperature controller subsystem in Matlab/Simulink is shown in Figure 2-23.

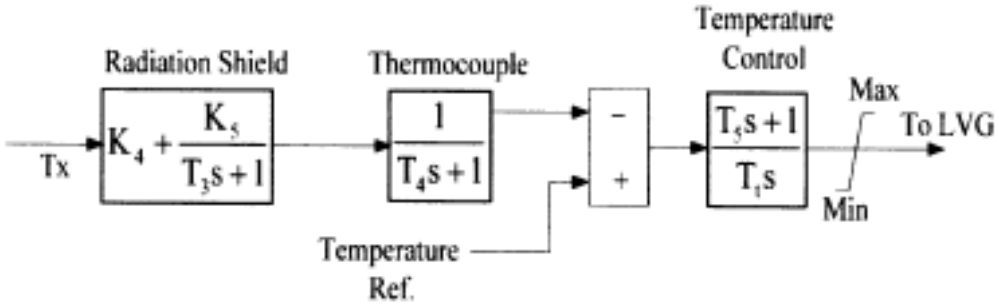

Figure 2-22. The block diagram of the temperature controller in MGT [17]

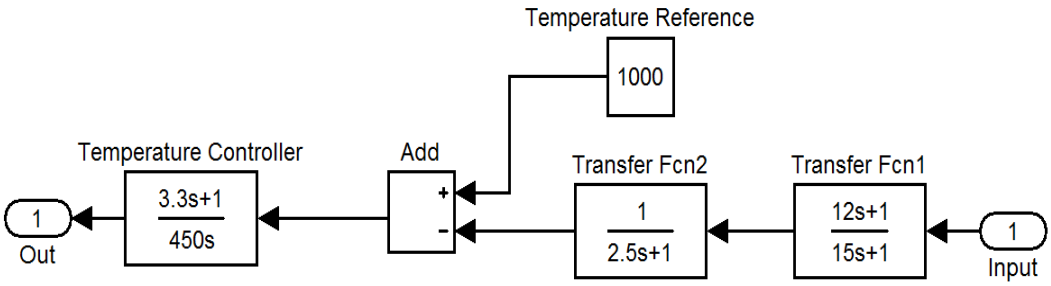

Figure 2-23. The Simulink implementation of the temperature controller in MGT

The output of all controllers goes to a low value select to produce the fuel demand signal. The working principle is shown in Figure 2-24.

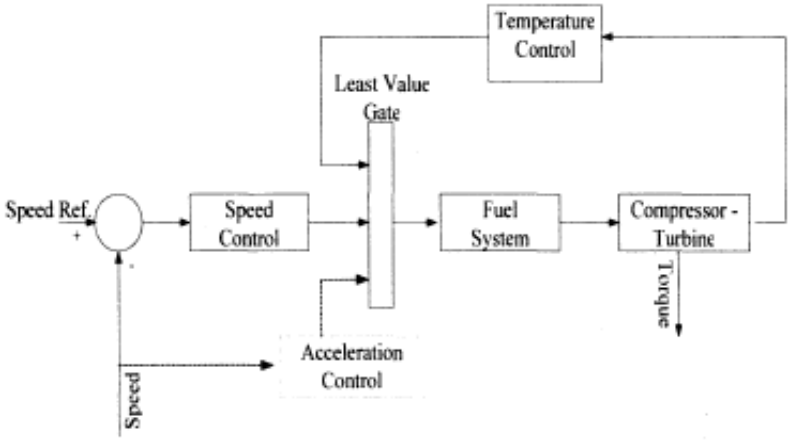

Figure 2-24. The working principle of MGT [17]

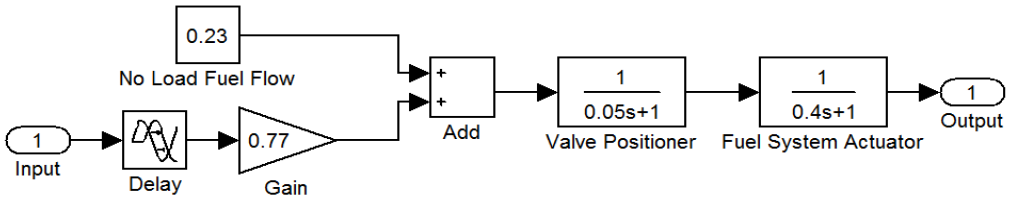

Figure 2-25. The Simulink implementation of the fuel control system in MGT

The fuel system is composed of the valve positioner and the fuel system actuator. References [18-19] give these transfer function equations. The valve positioner and the fuel system actuator transfer functions are given below.

$$E = \frac{K_v}{T_v s + C} F_d \tag{2.15}$$

$$W_f = \frac{K_f}{T_f s + C} E \tag{2.16}$$

Where K_v and K_f are the gain. T_v and T_f are the time constants. C is a constant. Based on these equations, the Matlab/Simulink subsystem of the fuel control system is shown in Figure 2-25. V_{ce} represents the minimum amount of the required fuel. It is scaled by the gain value of 0.77 and offset by 0.23, the fuel flow at no load. The time delay preceding the fuel flow control represents the delays in the governor control using digital logic in place of analog devices.

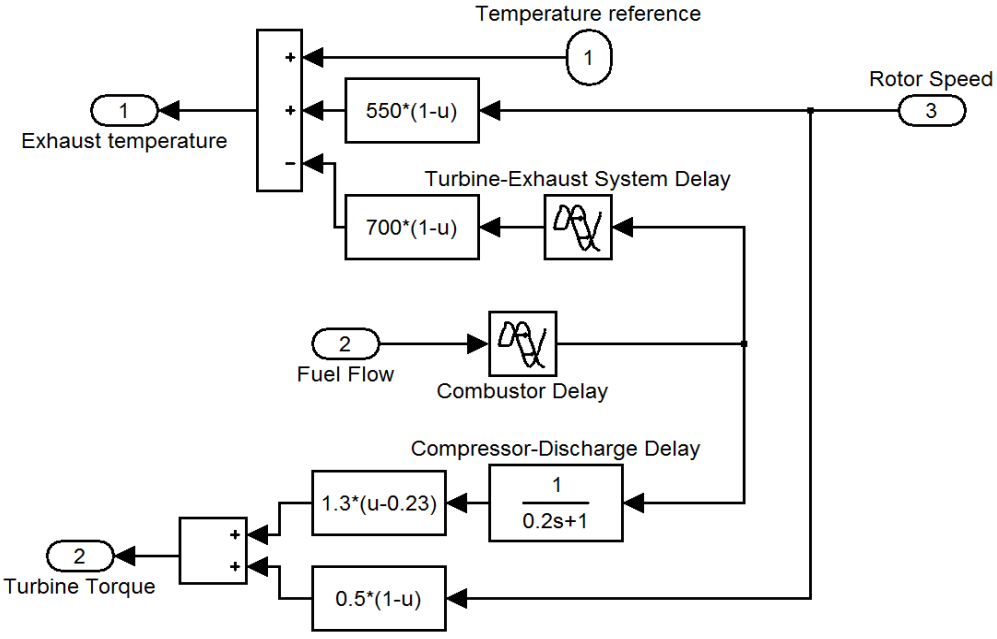

Figure 2-26. The Simulink implementation of the compressor-turbine in MGT

The compressor-turbine is the heart of the micro gas turbine and is essentially a linear, non-dynamic device (with the exception of the rotor time constant). Both the torque and the exhaust temperature characteristics of the single-shaft gas turbine are essentially linear with respect to fuel flow and turbine speed and are given by the following equations [19]. The compressor-turbine subsystem in Matlab/Simulink is shown in Figure 2-26. The first input is the temperature reference; The second input is the p.u. fuel demand signal; and the third input is the p.u. rotor speed. The output values are the exhaust temperature and the p.u. turbine torque, respectively.

Also the load voltage is regulated at the preset per unit value by a PI voltage regulator using abc_to_dg and dg_to_abc transformations. The first output of the voltage regulator is a vector containing the three modulating signals used by the PWM generator to generate the 6 IGBT pulse. The second output returns the modulation index.

Finally, the Matlab/Simulink model of Micro Gas Turbine is shown in Figure 2-27.

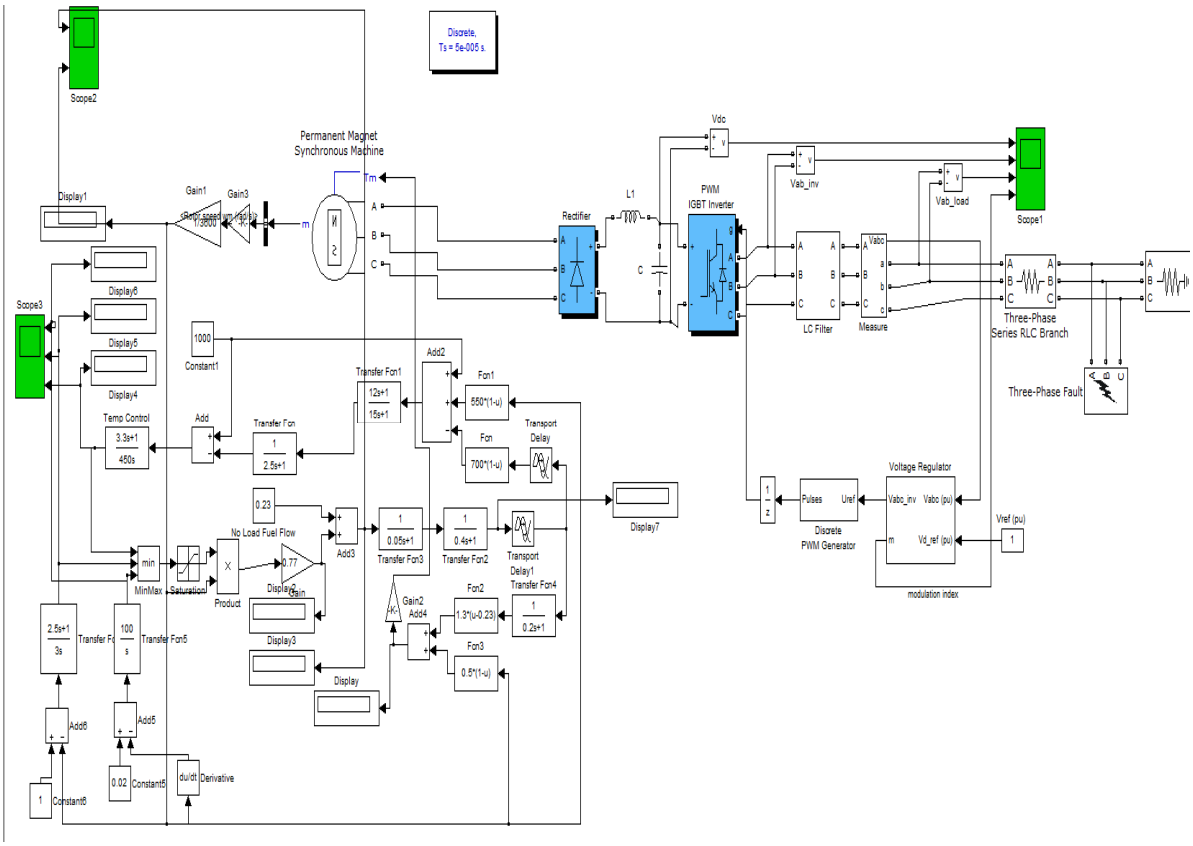

Figure 2-27. The Simulink model of Micro Gas Turbine

2.4.4 Fuel Cell

Fuel cells produce electricity continuously and directly as result of a chemical reaction. Chemical reactions often involve the transfer of the electrons from one atom to another, creating one of each positive and negative electron. More specifically, if a carefully chosen reaction is made to take place in an electrical circuit, with a source of electrons at one "pole" and a substance that absorbs the electrons to complete the reaction at the other "pole", the electrons move around the circuit [20]. A typical fuel cell produces a small voltage. To create enough voltage, individual fuel cells are combined into “fuel cell stacks” to provide sufficient power in a single circuit. The chemical reactions are summarized in Table 2-3.

Table 2-3. Summary of chemical reactions in different fuel cells

Fuel Cell	Anode Reaction	Cathode Reaction	Overall Reaction
Proton Exchange	$2H_2 \rightarrow 4H^+ + 4e^-$	$O_2 + 4H^+ + 4e^- \rightarrow 2H_2O$	$2H_2 + O_2 \rightarrow 2H_2O(l)$
Alkaline	1) $2H_2 \rightarrow 4H^+ + 4e^-$ 2) $4H^+ + 4(OH)^- \rightarrow 4H_2O$	$O_2 + 2H_2O + 4e^- \rightarrow 4(OH)^-$	$2H_2 + O_2 \rightarrow 2H_2O(l/g)$
Phosphoric Acid	$2H_2 \rightarrow 4H^+ + 4e^-$	$O_2 + 4H^+ + 4e^- \rightarrow 2H_2O$	$2H_2 + O_2 \rightarrow 2H_2O(g)$
Molten Carbonate	1) $2H_2 \rightarrow 4H^+ + 4e^-$ 2) $4H^+ + 2CO_3^{-2} \rightarrow 2H_2O + 2CO_2$	$O_2 + 2CO_2 + 4e^- \rightarrow 2CO_3^{-2}$	$2H_2 + O_2 \rightarrow 2H_2O(g)$
	1) $CH_4 + H_2O \rightarrow CO + 3H_2$ (reformation) 2) $CO + H_2O \rightarrow CO_2 + H_2$ (water-gas shift) 3) $4H_2 + CO_2 \rightarrow CO_2 + 8H^+ + 8e^-$ 4) $CO_2 + 8H^+ + 4CO_3^{-2} \rightarrow 5CO_2 + 4H_2O$	$2O_2 + 4CO_2 + 8e^- \rightarrow 4CO_3^{-2}$	$CH_4 + 2O_2 \rightarrow 2H_2O(g) + CO_2(g)$
Solid Oxide	1) $2H_2 \rightarrow 4H^+ + 4e^-$ 2) $4H^+ + 2O^{-2} \rightarrow 2H_2O$	$O_2 + 4e^- \rightarrow 2O^{-2}$	$2H_2 + O_2 \rightarrow 2H_2O(g)$
	1) $CH_4 + H_2O \rightarrow CO + 3H_2$ (reformation) 2) $CO + H_2O \rightarrow CO_2 + H_2$ (water-gas shift) 3) $4H_2 + CO_2 \rightarrow CO_2 + 8H^+ + 8e^-$ 4) $CO_2 + 8H^+ + 4O^{-2} \rightarrow CO_2 + 4H_2O$	$2O_2 + 8e^- \rightarrow 4O^{-2}$	$CH_4 + 2O_2 \rightarrow 2H_2O(g) + CO_2(g)$

To some extent, a fuel cell stack operates like a battery. The principle of the fuel cell was discovered by the German scientist Christian Friedrich Schonbein in 1838. Based on this work, the first fuel cell was developed by the Welsh scientist Sir William Robert Grove in 1843, using the similar materials to today's phosphoric-acid fuel cell [20]. There are currently several different types of fuel cells under development, which can run on a variety of fuels. There are basically five fuel cell types: proton exchange membrane fuel cells (PEMFC), alkaline fuel cells (AFC), phosphoric acid fuel cells (PAFC), molten carbonate fuel cells (MCFC), solid oxide fuel cells (SOFC). In Table 2-4, the key features of these fuel cells are summarized. A proton

exchange membrane fuel cell (PEMFC) stack and a solid-oxide fuel cell (SOFC) stack have been studied and modeled in Matlab/Simulink.

Table 2-4. The key features of different fuel cells

	PEMFC	AFC	PAFC	MCFC	SOFC
Electrolyte	Ion Exchange Membranes	Mobilized or Immobilized Potassium Hydroxide	Immobilized Liquid Phosphoric Acid	Immobilized Liquid Molten Carbonate	yttrium-stabilized zirconia
Operating Temperature	80°C	120°C - 150°C	200°C	650°C	800-1000°C
Charge Carrier	H^+	OH^-	H^+	CO_3^{-2}	O^{-2}
External Reformer for CH_4	Yes	Yes	Yes	No	No
Catalyst	Platinum	Platinum	Platinum	Nickel	Perovskites
Prime Cell Components	Carbon-based	Carbon-based	Graphite-based	Stainless-based	Ceramic
Product Water Management	Evaporative	Evaporative	Evaporative	Gaseous Product	Gaseous Product
Usable rejected Heat recovery	Negligible	Negligible	Yes	Yes	Yes
Gaseous/Liquid Water formation	Cathode	Anode	Cathode	Anode	Anode
Fuel	Pure H_2 (tolerates CO_2)	Pure H_2	Pure H_2 (tolerates CO_2, 1.5% CO)	H_2, CO, CH_4, other hydrocarbons (tolerates CO_2)	H_2, CO, CH_4, other hydrocarbons (tolerates CO_2)
Electrical Efficiency	35%	40-60%	40-50%	50-60%	50-65%

Hydrogen fueled Proton Exchange Membrane (PEM) Fuel cells are the most common in applications. A PEM fuel cell uses hydrogen fuel and oxygen from the air to produce electricity. Hydrogen and ambient oxygen are fed into opposite sides of the fuel cell, separated by a membrane (the PEM), forcing a flow of electrons through an attached circuit to complete the reaction of hydrogen and oxygen into water. As shown in Figure 2-28, at the anode, the electrons are produced from the hydrogen molecules, flowing through an external circuit. At the cathode, the oxidant is reduced to conduct the electrons back from the external circuit. The electrolyte is

the proton exchange membrane. The catalyst is not required but highly recommended to help the chemical reactions to take place.

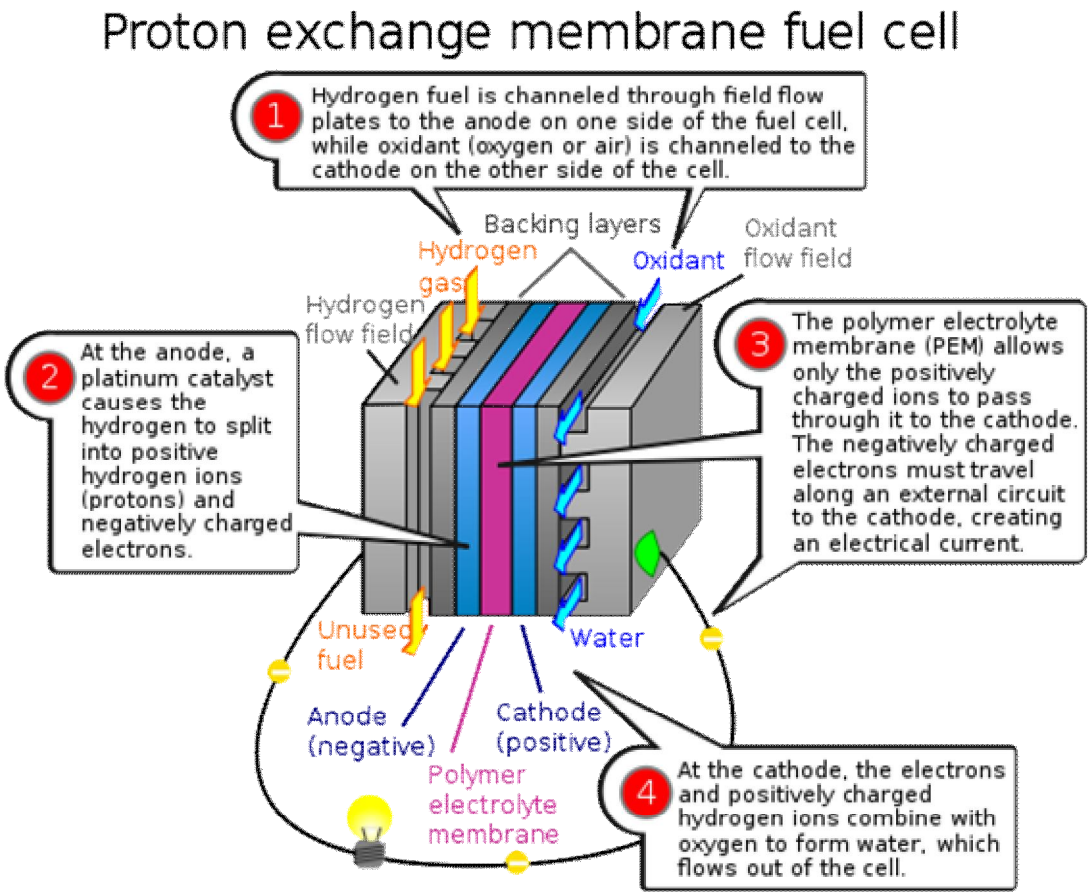

Figure 2-28. The operation principle of a PEM fuel cell [21]

The typical U-I curve of a PEM fuel cell is shown in Figure 2-29. It consists of three regions. Activation regions dominates at low current. It represents the activation voltage drop due to the slowness of the chemical reactions taking place at electrode surfaces. The second region is governed by the ohmic losses. The last region represents the mass transport losses resulting from the change in concentration of reactants as the fuel is used. The Matlab/Simulink model of PEMFC is developed by using a combination of physical and empirical modeling techniques developed by Mann *et al.*(2000) and Amphlett *et al.*(1995) [22].

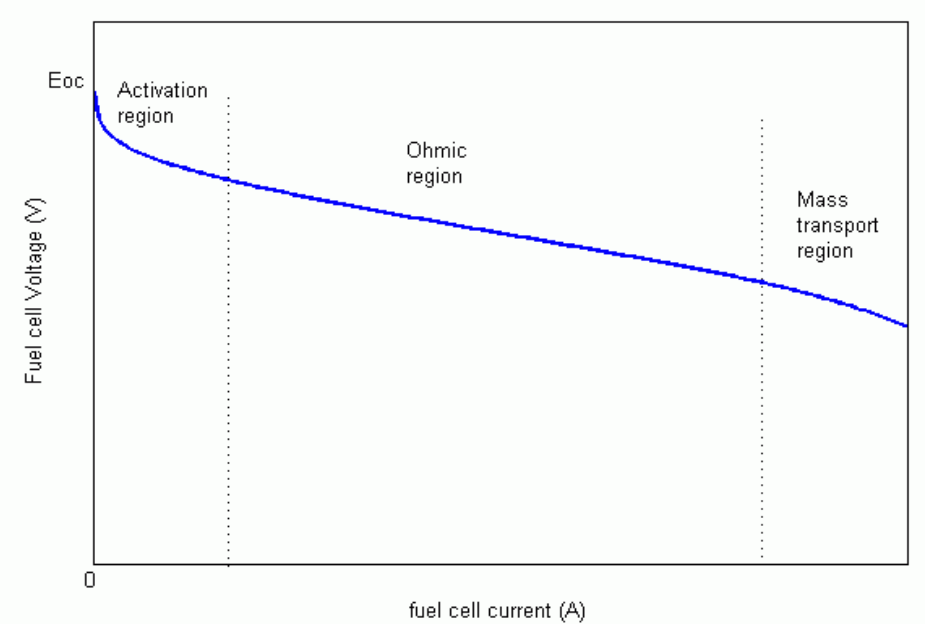

Figure 2-29. A typical U-I curve of a PEM fuel cell

The power of the fuel cell stack is defined as

$$P = nVI = nI(E_{Nernst} - \eta_{act} - \eta_{ohm}) \tag{2.17}$$

where n is the number of fuel cells. E_{Nernst} is the Nernst voltage. η_{act} and η_{ohm} are the activation overvoltage and the resistive overvoltage, respectively. V is the single cell voltage. I is the single cell current.

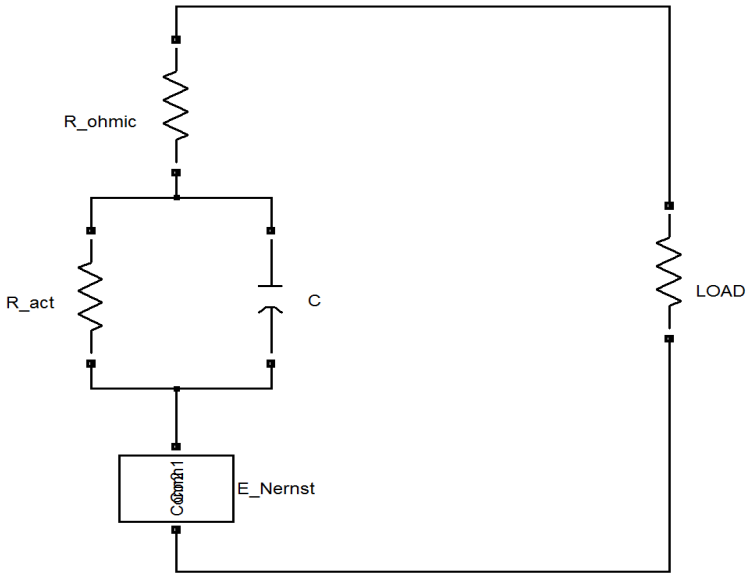

Figure 2-30. The equivalent circuit of the dynamical fuel cell model

$$E_{Nernst} = 1.229 - 0.85\times10^{-3}(T - 298.15) + 4.308\times10^{-5}T\cdot\ln(P_{H_2}P_{O_2}^{\frac{1}{2}}) \quad \text{when } T \le 100°C \tag{2.18}$$

$$E_{Nernst} = 1.229 - 0.85\times10^{-3}(T - 298.15) + 4.308\times10^{-5}T\cdot\ln(\frac{P_{H_2}P_{O_2}^{\frac{1}{2}}}{P_{H_2O}}) \quad \text{when } T > 100°C \tag{2.19}$$

where P_{H_2} is the partial pressure of hydrogen inside the stack; P_{O_2} is the partial pressure of oxygen inside the stack; P_{H_2O} is the partial pressure of water vapor inside the stack. T is the operating temperature.

Even when there is no current output, the real open circuit voltage is less than the ideal because of certain losses occurring at zero current. The activation voltage drop due to the slowness of the chemical reactions taking place at electrode surfaces.

$$\eta_{act} = \xi_1 + \xi_2 T + \xi_3 T\cdot\ln(C_{O_2}) + \xi_4 T\ln(i) \tag{2.20}$$

$$\eta_{ohm} = -i(R_{electronic} + R_{proton}) \tag{2.21}$$

where C_{O_2} is the oxygen concentration at the cathode; R is the resistance. ξ is the empirical coefficient for calculating activation overvoltage. In reference [23], the equation can be substituted by a semi-empirical equation like

$$\eta_{act} = -0.9514 + 0.00312T - 0.000187T\ln(i) + 7.4\times10^{-5}T\ln(C_{O_2}) \tag{2.22}$$

The oxygen concentration C_{O_2} is calculated by the semi-empirical equation [23]:

$$C_{O_2} = \frac{P_{O_2}}{5.08\times10^6}e^{(\frac{-489}{T})} \tag{2.23}$$

Ohmic Losses come from the ionic resistance of the electrolyte and from the electronic resistance of the electrodes, interconnections and other parts of the fuel cell.

The membrane specific resistivity for the flow of hydrated protons is defined as

$$r_m = \frac{181.6[1 + 0.03\frac{i}{A} + 0.062(\frac{T}{303})^2(\frac{i}{A})^{\frac{5}{2}}]}{(\lambda - 0.634 - \frac{3i}{A})e^{(\frac{4.18T}{T-303})}} \tag{2.24}$$

Where A is the active cell area. λ is the empirical parameter of the membrane water content. The resistance of the membrane is expressed as [22]:

$$R_m = \frac{l\cdot r_m}{A} \tag{2.25}$$

Where l is the thickness of the polymer membrane. According to these equations presented above, the basic model is applicable for a typical PEMFC stack of various configurations and operating conditions.

Based on the NedStack PS100 product datasheet, the corresponding PEM fuel cell stack is modeled and simulated. The simulation results are shown in Figure 2-32. It can reflect the actual fuel cell characteristics shown in Figure 2-31.

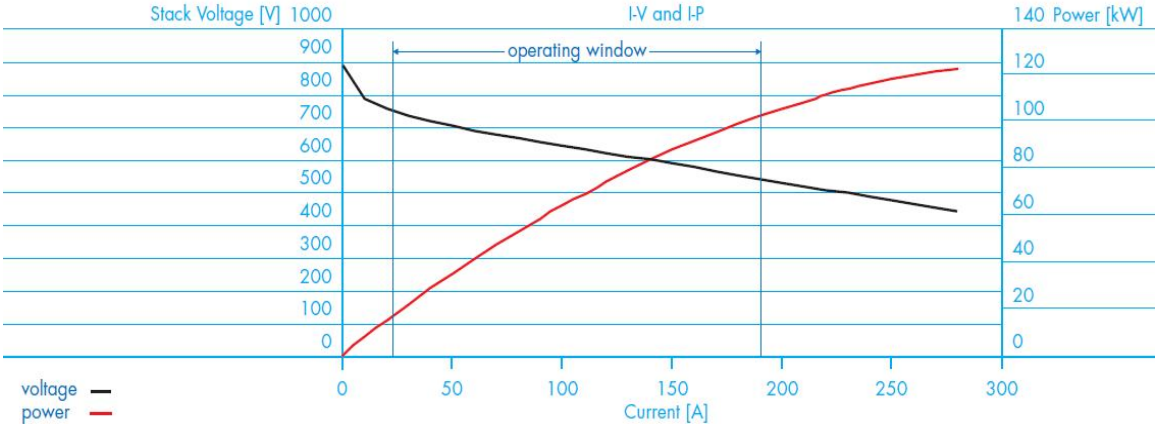

Figure 2-31. I-V and I-P curves of a NedStack PS100 fuel cell stack [24]

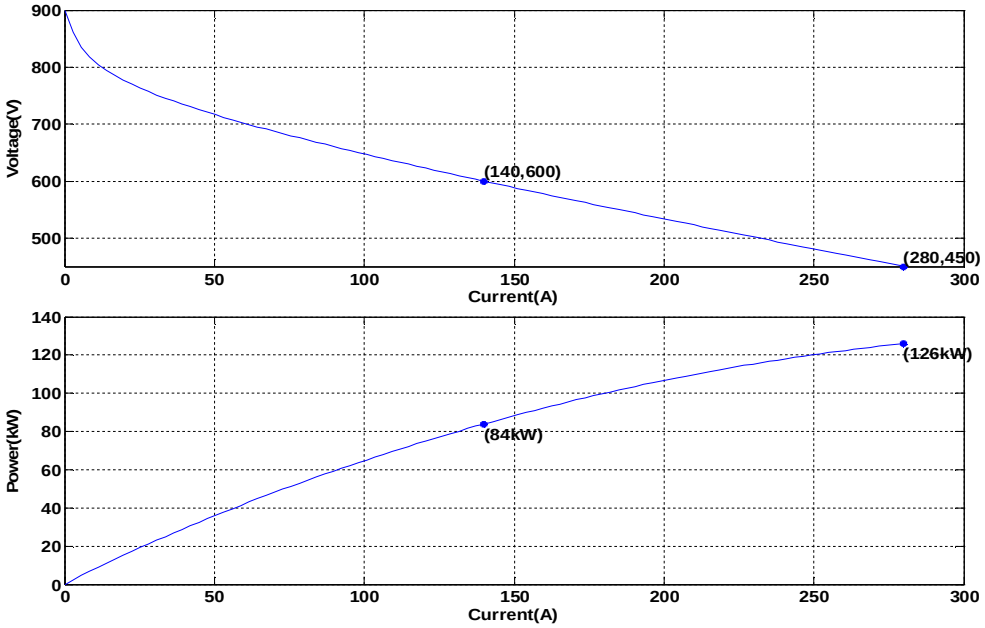

Figure 2-32. Simulation results of a Nedstack PS100 fuel cell stack

For low currents, the major loss is the activation loss. The voltage drops sharply from the open circuit voltage 900V. There is also a linear voltage drop starting from 20A to 190A, namely the operating window. The major loss is the ohmic loss at this moment. And at high working currents, the sharp voltage drop is due to the concentration loss. But the effect of the concentration losses is not taken into consideration in this PEM fuel cell stack model. The future work involving with an advanced and complicated model will address the effect of the concentration loss. In addition, as is shown in the I-P curve, the maximum power is around 84kW, which occurs at around 50% of the maximum current.

A SOFC is an electrochemical conversion device that produces electricity directly from oxidizing a fuel. However, unlike normal fuel cells, the SOFC is composed entirely of solid-state materials, typically ceramics. It allows SOFC to operate at much higher temperatures than conventional fuel cells. So it has less need for the catalysts. The most attractive advantage of this type of fuel cell is the high efficiency. Based on references [25-26], a basic SOFC model in the normal operation is obtained. The stack model will be based on the following assumptions:

- The gases are ideal.
- The stack is fed with hydrogen and air. If natural gas instead of hydrogen is used as fuel, the dynamics of the fuel processor must be included in the model, upstream of the hydrogen inlet, as a first-order transfer function. The transfer function gain should reflect the changes in composition occurring during the process. The effect of the fuel processor in the model will be tested in the future.
- The channels that transport gases along the electrodes have a fixed volume, but their lengths are small. It is only necessary to define one single pressure value in their interior.
- The exhaust of each channel is via a single orifice. The ratio of pressures between the interior and exterior of the channel is large enough to consider that the orifice is choked.
- The temperature is stable at all times.
- The only source of losses is ohmic, as the working conditions of interest are not close to the upper and lower extremes of current.
- The Nernst equation can be applied.

An SOFC stack model has been studied based on the references mentioned above. A hybrid sample system consisting of an SOFC and other elements will be presented in the sample system section.

2.4.5 Wind Turbine

Typically, a wind turbine is composed of a rotor, a generator, a three-blades, and a drive train. As the wind blows through the blades, the power captured by the wind turbine is converted into electrical power by a generator. The pitch angle is controlled in order to limit the generator output power to its nominal value for high wind speeds. Through some power electronic interface, the power is transmitted to the grid.

A wind turbine extracts kinetic energy from the wind blowing through the blades. The output power of the turbine is given by the following equation [27].

$$P_m = \frac{1}{2} C_p(\lambda, \beta) \rho A V^3 \tag{2.26}$$

P_m Mechanical output power of the turbine (W)

ρ Air density (kg / m^3)

A Turbine swept area (m^2)

V Wind speed (m/s)

$C_p(\lambda, \beta)$ Performance coefficient of the turbine

λ Tip speed ratio of the rotor blade tip speed to wind speed

β Blade pitch angle (deg)

C_p is a characteristic of the wind turbine. There are different methods to calculate C_p such blade element method, look-up table and analytical approximation. In this thesis, $C_p(\lambda, \beta)$ is modeled by a generic equation.[28]

$$C_p(\lambda, \beta) = c_1 \left(\frac{c_2}{\lambda_i} - c_3\beta - c_4\right) e^{\frac{-c_5}{\lambda_i}} + c_6\lambda \tag{2.27}$$

$$\frac{1}{\lambda_i} = \frac{1}{\lambda + 0.08\beta} - \frac{0.035}{\beta^3 + 1} \tag{2.28}$$

The coefficients *c1* to *c6* are: c1 = 0.5176, c2 = 116, c3 = 0.4, c4 = 5, c5 = 21 and c6 = 0.0068. The maximum value of C_p ($C_{p\max} = 0.48$) is achieved for β = 0 degree and for λ = 8.1. This particular value of λ is defined as the nominal value (λ_{nom}).

Based on these equations, the Simulink model of a wind turbine is shown in Figure 2-33.

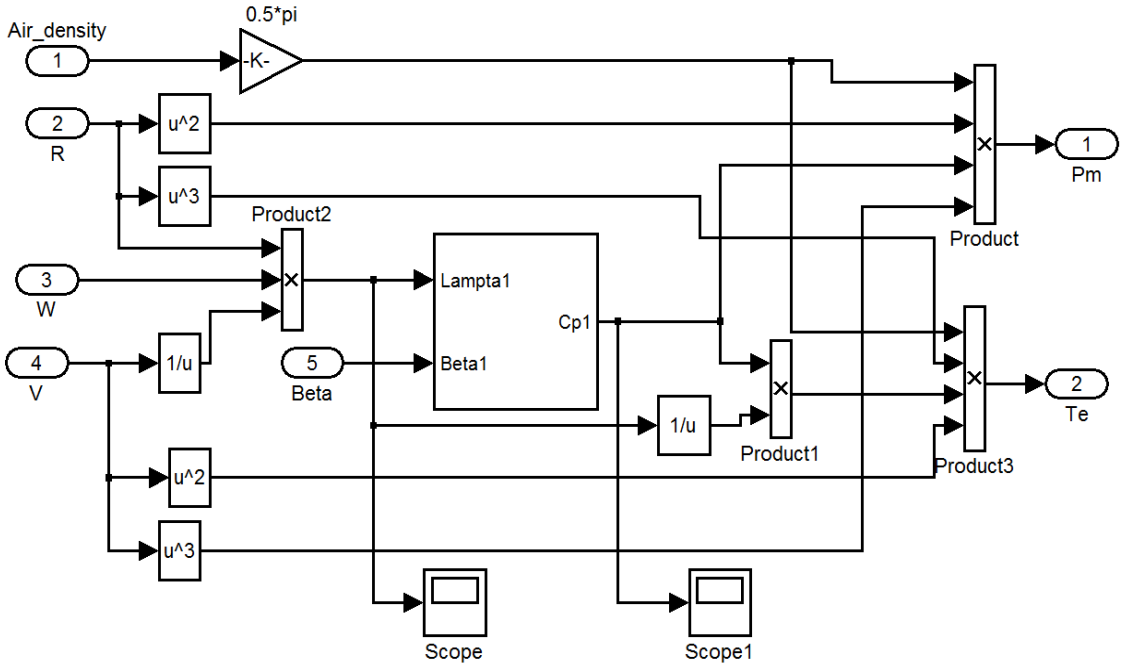

Figure 2-33. Wind turbine Simulink model

Doubly-fed wind turbine (DFIG) consists of a wound rotor induction generator and an AC/DC/AC converter. DFIG is used in variable speed turbines. The stator winding is connected directly to the 60 Hz grid while the rotor is fed at variable frequency through the AC/DC/AC converter. Using DFIG technology, it is possible to capture the maximum energy over a wind range of wind speeds by optimizing the turbine speed. The working principle of DFIG is shown in Figure 2-34.

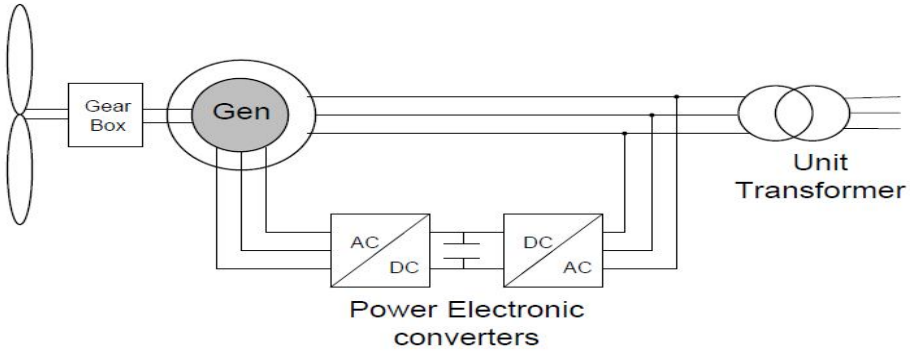

Figure 2-34. The working principle of DFIG [29]

References [30-33] present a detailed description of DFIG modeling. The mechanical power and the stator electric power output are computed as follows.

$$P_m = T_m \omega_r \tag{2.29}$$

Where P_m is the mechanical power captured by the wind turbine and transmitted to the rotor. T_m is the mechanical torque applied to rotor. ω_r is the rotational speed of rotor.

However, in the fixed speed wind turbine, the generator is a squirrel-cage induction generator. The stator winding is connected directly to the grid and the rotor is driven by the wind turbine. The power captured by the wind turbine is converted into electrical power by the induction generator and is transmitted to the grid by the stator winding. The rotor of a fixed-speed wind turbine rotates at a fixed speed determined by the frequency of the grid, the gear ratio and the pole pairs of generator. The reactive power absorbed by the induction generator is provided by the grid or by some devices like capacitor banks, SVC, STATCOM or synchronous condenser.

This type of wind turbines is much more simple, robust and more cost-efficient compared to the other wind turbine types. However, the reactive power consumption cannot be controlled. Another drawback with the fixed speed wind turbine is that wind speed fluctuation is transmitted into the mechanical torque and it is finally transferred to the electrical power on the grid. The fluctuation in the delivered power to the grid can lead to large voltage fluctuation where the wind farm connected to a weak grid [29].

A random wind speed generator has been built in Matlab/Simulink as well.

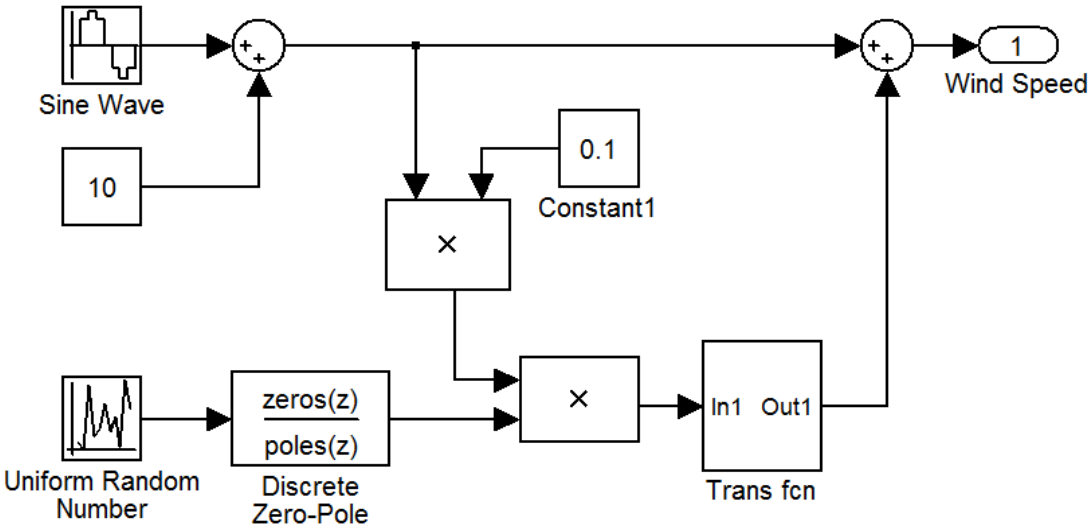

Figure 2-35. Random wind speed generator in Matlab/Simulink

In this section, the dynamic behavior of the doubly-fed wind turbine is analyzed when the wind speed changes randomly. Figure 2-36 shows the random wind speed passing through the blades. The generated real power and reactive power are illustrated in Figures 2-38 and 2-39. The pitch angle is controlled in order to limit the generator output power to its nominal value for high wind speeds. The real power is regulated at its nominal value 9MW. The reactive power absorbed by the induction generator is provided by the grid which is modeled as a three phase voltage source with infinite power rating. Thus the reactive power is regulated at almost 0Mvar. Fig shows the pitch angle response due to the random change in the wind speed. As can be seen, the response of the pitch angle of the wind turbine blades follows the pattern of wind speed which is shown in Fig. Also the simulation result of the rotor speed response is shown in Figure 2-37.

The wind turbine with induction generator is also tested without the pitch angle controller. The detailed simulation results are shown in the following sample system section.

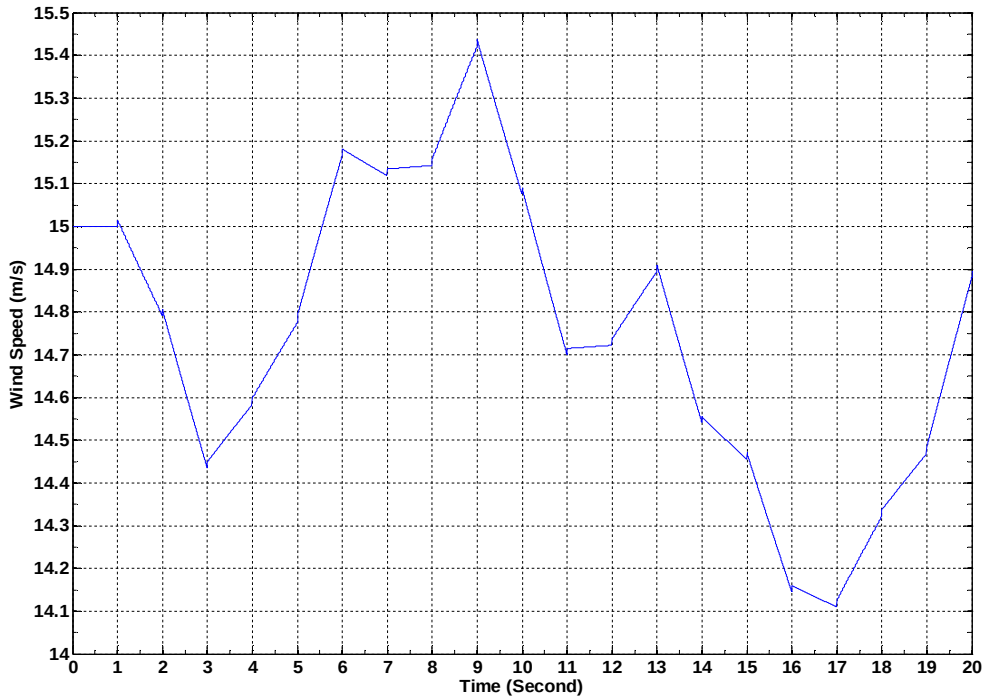

Figure 2-36. Random wind speed over a period of 20 seconds

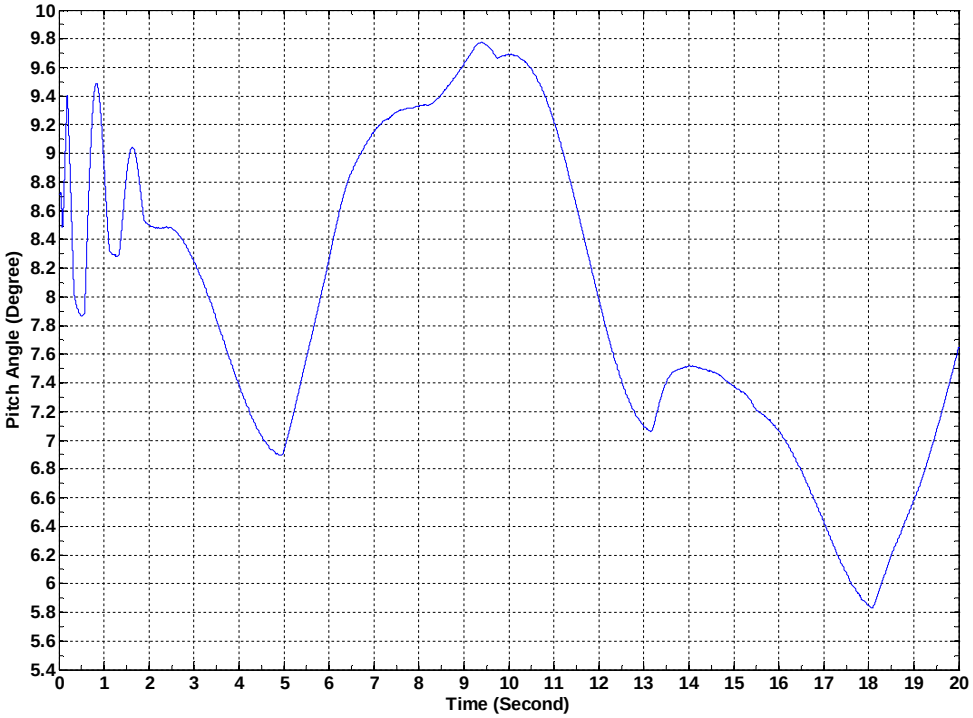

Figure 2-37. Pitch angle response to random wind speed over a period of 20 seconds

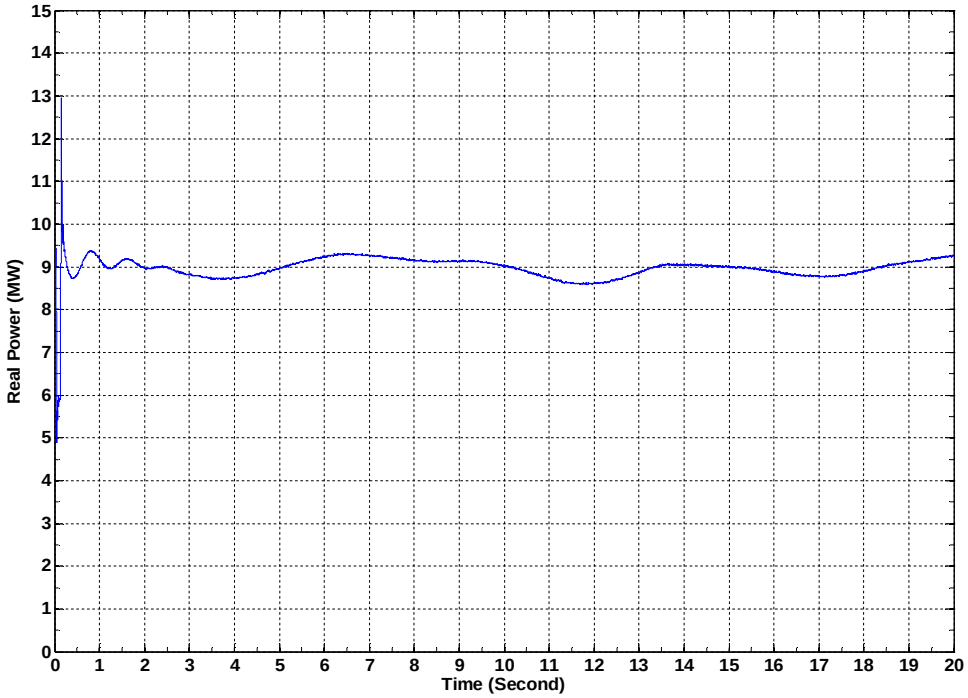

Figure 2-38. Real power response to random wind speed over a period of 20 seconds

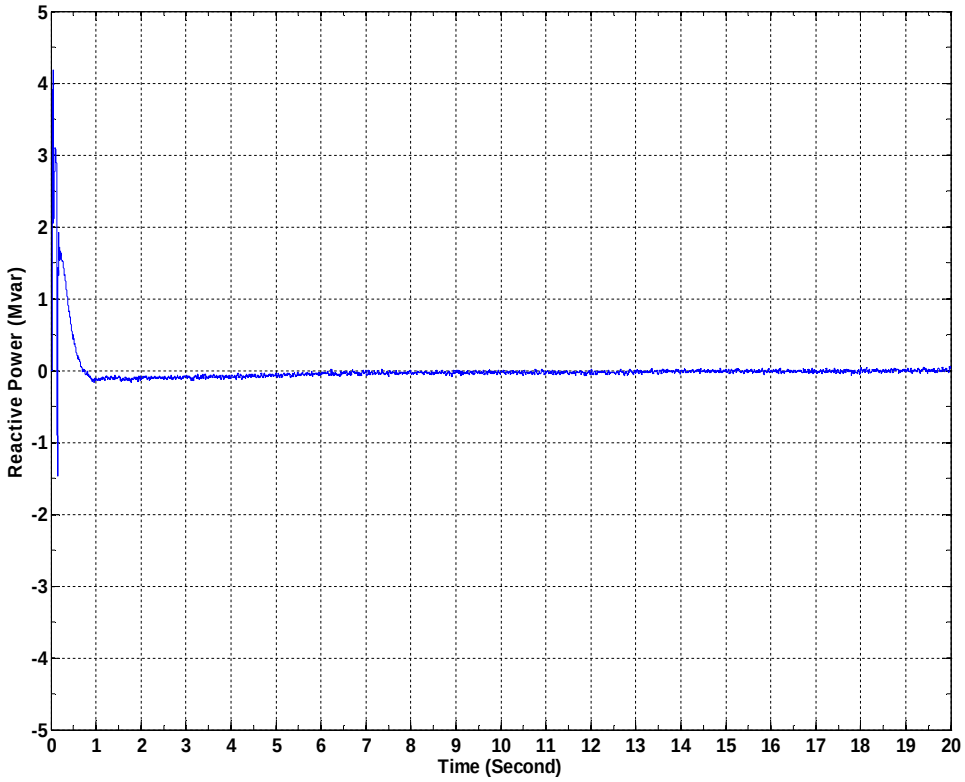

Figure 2-39. Reactive power response to random wind speed over a period of 20 seconds

2.5 Short-term Storage Modeling

The electricity demand fluctuates depending on the time of the day and the time of a year. Since the traditional power grid is not able to store up electricity, the mismatch between supply and demand is more likely observed. As the concept of Microgrid is becoming more pervasive, a mixed power system make the best use of the different types of local generation. Some forms of generations have large response time and others have little flexibility in operation. In addition, some forms of generations can start up very quickly to provide more or less energy depending the real-time load demand pattern. Provided these reasons clearly, the energy storage is beneficial in managing such a system. A desired form of energy storage is expected to provide the required power into the power system and store up sufficient energy at low electricity consumption. Four types of short-term storage are studied and modeled: Battery Storage, Flywheel, Supercapacitor and Pumped Hydro Storage.

2.5.1 Battery

There are several approaches to model a battery. A commonly used battery model is the Thevenin equivalent circuit. As is seen in Figure 2-40, it consists of an ideal no-load voltage (*Eo*), internal resistance (*R*), an overvoltage resistance *Ro* and *Co*. *Co* represents the capacitance of the parallel plates. *Ro* represents the non-linear resistance contributed by the contact resistance of plate to electrolyte. The major disadvantage of this model is that all values are unrealistically assumed to be constants. It is possible to extend the Thevenin battery model to a more complex model.

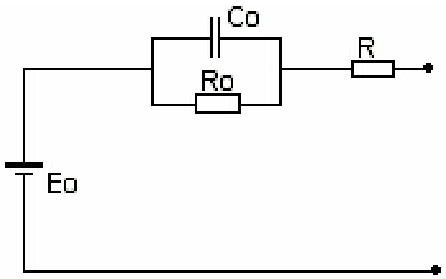

Figure 2-40. The Thevenin equivalent circuit of the battery model

The battery is also modeled using a controlled voltage source in series with a constant resistance. As proposed in [34], the battery block implements a generic dynamic model parameterized to represent most popular types of the rechargeable batteries.

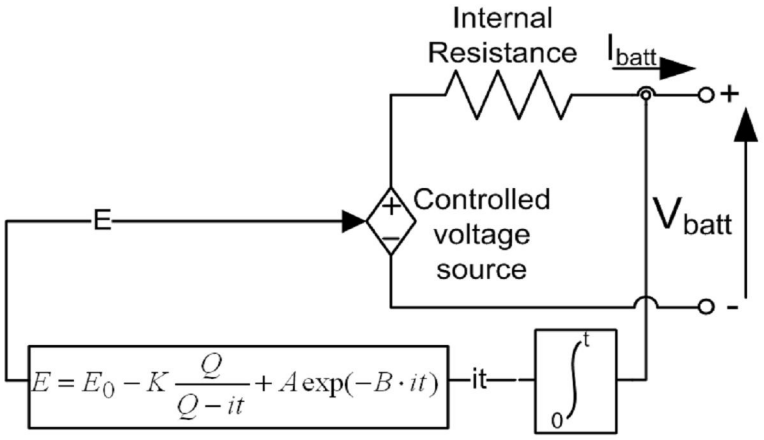

Figure 2-41. The equivalent circuit of the rechargeable battery [34]

Where all the parameters of the equivalent circuit can be estimated to represent a specific battery based on its own electrical characteristic.

E = no-load voltage (V)

E_0 = battery constant voltage (V)

K = polarization voltage (V)

Q = battery capacity (Ah)

$\int idt$ = actual battery charge (Ah)

A = exponential zone amplitude (V)

B = exponential zone time constant inverse $(Ah)^{-1}$

Vbatt = battery voltage (V)

R = internal resistance (Ω)

i = battery current (A)

The proposed model [34] is based on specific assumptions and has limitations:

1) Model assumptions:

• The internal resistance is supposed constant during the charge and discharge cycles and doesn't vary with the amplitude of the current.

• The model's parameters are deduced from the discharge characteristics and assumed to be the same for charging.

• The capacity of the battery doesn't change with the amplitude of the current (No Peukert effect).

• The temperature doesn't affect the model's behavior.

• The Self-Discharge of the battery is not represented.

• The battery has no memory effect.

2) Model limitations:

• The minimum No-Load battery voltage is 0 V and the maximum battery voltage is not limited.

• The minimum capacity of the battery is 0 Ah and the maximum capacity is not limited. Therefore, the maxi- mum SOC can be greater than 100% if the battery is overcharged.

The key parameters of common batteries are presented in Table 2-5.

Table 2-5. The key parameters of common batteries [34]

Type Parameters	Lead-Acid 12V 1.2Ah	Nickel-Cadmium 1.2V 1.3Ah	Lithium--Ion 3.6V 1Ah	Nickel-Metal-Hydrid 1.2V 6.5Ah
$E_0(V)$	12.6463	1.2505	3.7348	1.2848
R (Ω)	0.25	0.023	0.09	0.0046
K (V)	0.33	0.00852	0.00876	0.01875
A (V)	0.66	0.144	0.468	0.144
B $(Ah)^{-1}$	2884.61	5.7692	3.5294	2.3077

To prevent the battery from overcharging or discharging, the State-Of-Charge (SOC) of the battery is no greater than 100% (fully charged) and no less than 0% (empty condition) in Simulink model. SOC is defined as:

$$SOC = 100(1 - \frac{\int_0^t idt}{Q}) \tag{2.30}$$

A 240V, 8Ah Lithium-Ion battery is modeled and used to support a constant load. The initial SOC is assumed to be 100% (fully charged). To prevent the battery from over discharging, when the SOC goes under 10%, the battery will be recharged by a diesel generator. And to prevent the battery from overcharging, when the SOC goes up to 90%, the back-up diesel generator is removed immediately. The battery voltage and SOC simulation results are monitored and shown in Figures 2-42 and 2-43. At t = 400 s, the SOC drops under 10%. A diesel generator starts up to provide the power. At t = 1400 s, the SOC goes up to 90%. The back-up generator is removed immediately.

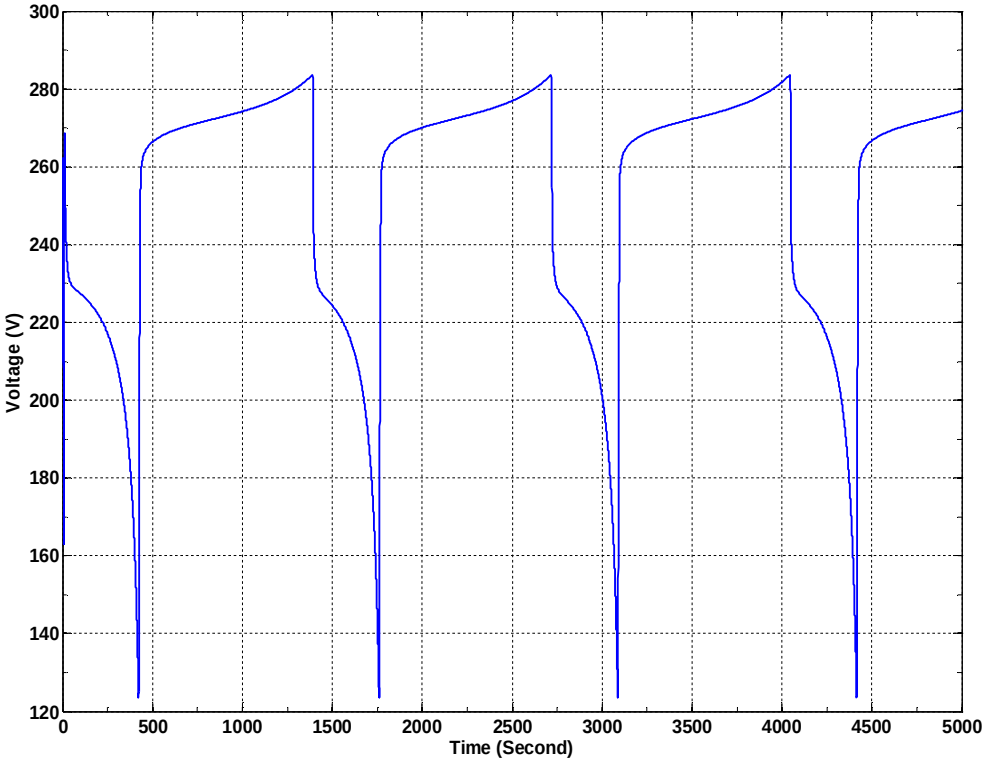

Figure 2-42. Voltage change of a 240V, 8Ah lithium-Ion battery

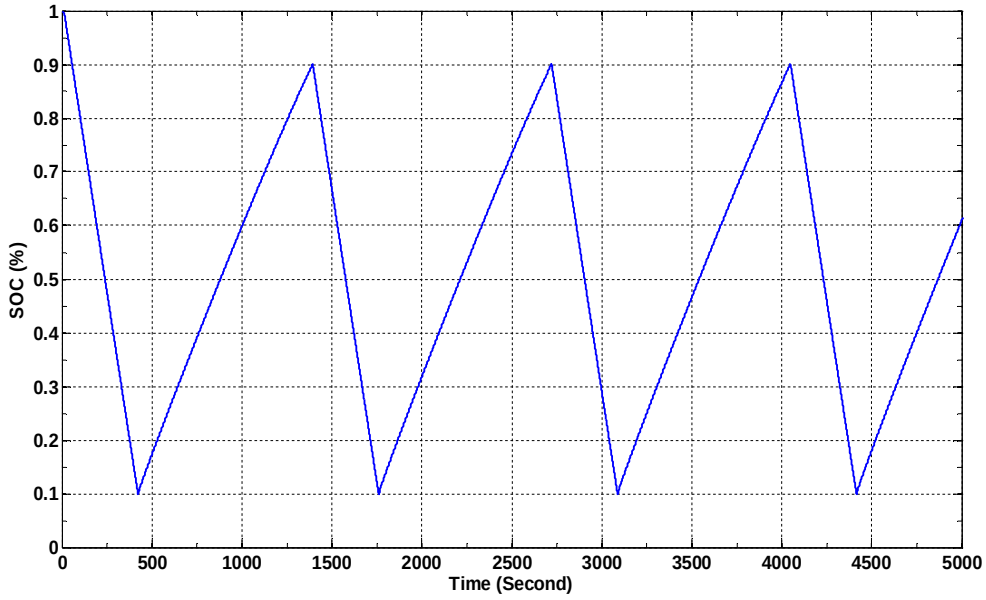

Figure 2-43. SOC change of a 240V, 8Ah Lithium-Ion battery

2.5.2 Flywheel

As one form of energy storage, flywheels are typically useful when there is a mismatch between the generated power and the power required by the load. For example, the flywheel energy storage can provide power for maximum acceleration. In term of Microgrid, the advanced flywheel energy storage can handle the power needs of the peak load and store the energy at the low load period. It is a very good solution for the supply of critical loads. Flywheel energy storage devices have a relatively fast response time. The stability of the local load can benefit from the short-term storage. Generally speaking, it is an electromechanical approach to store energy. To store the electricity, a motor is used to convert the electrical energy from power grid or any other external source into the mechanical energy. The energy stored in the flywheel is a function of the mass density, angular velocity, inner diameter, outer diameter, length, etc. Then the flywheel is able to provide electrical energy using the same motor as a generator at this moment. My thesis focuses on a cylinder flywheel, which is the typical shape of a flywheel. The flywheel model is composed of the energy subsystem, SVPWM subsystem, control subsystem, a motor/generator, power electronics, etc.

The rotational energy stored in the flywheel is defined as

$$E = \frac{1}{2} I \omega^2 \tag{2.31}$$

Where I is the moment of inertia that is directly proportional to the mass of the rotor by means of a constant that depends on the shape factor. ω is the angular velocity.

For a cylinder, a typical shape of flywheels, the moment of inertia is

$$I = \frac{1}{2} \pi h \rho (r_0^4 - r_i^4) \tag{2.32}$$

Where the outer diameter and inner diameter are represented by r_0 and r_i, respectively. h is length and ρ is mass density. Thus

$$E = \frac{1}{4} \pi h \rho \omega^2 (r_0^4 - r_i^4) \tag{2.33}$$

The energy scales as ω^2. The flywheel with a larger angular velocity can store much more energy. A small and light flywheel is preferable because it can operate at high stress levels. So composite materials such as Carbon T1000 and Carbon AS4C are better options in making flywheels.

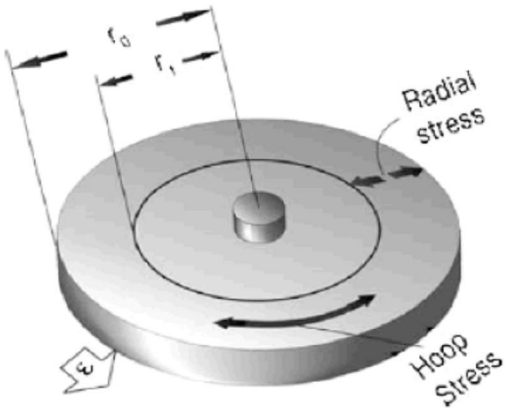

Figure 2-44. Force analysis on a cylindrical flywheel

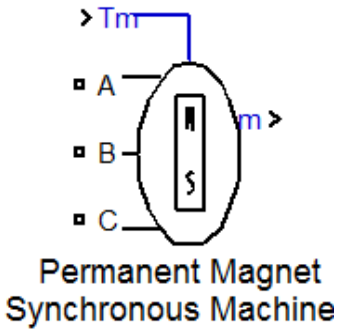

Figure 2-45. Simulink model of the permanent magnet synchronous machine

The motor/generator is modeled as a permanent magnet synchronous machine which is shown in Figure 2-45. The mode of operation is dictated by the sign of the mechanical torque (positive for motor mode, negative for generator mode). The electrical system is expressed by the equations:

$$\frac{d}{dt}i_d = \frac{1}{L_d}v_d - \frac{R}{L_d}i_d + \frac{L_q}{L_d}p\omega_r i_q \tag{2.34}$$

$$\frac{d}{dt}i_q = \frac{1}{L_q}v_q - \frac{R}{L_q}i_q - \frac{L_d}{L_q}p\omega_r i_d - \frac{\lambda p\omega_r}{L_q} \tag{2.35}$$

$$T_e = 1.5p[\lambda i_q + (L_d - L_q)i_d i_q] \tag{2.36}$$

Where L_q and L_d are q and d axis inductances. R is the resistance of the stator windings. i_q and i_d are q and d axis currents. v_q and v_d are q and d axis voltages. ω_r is the angular velocity of the rotor. λ is the amplitude of the flux induced by the permanent magnets of the rotor in the stator phases. p is the number of pole pairs. T_e is the electromagnetic torque.

The mechanical system is expressed by the equations:

$$\frac{d}{dt}\omega_r = \frac{1}{J}(T_e - F\omega_r - T_m) \tag{2.37}$$

$$\frac{d\theta}{dt} = \omega_r \tag{2.38}$$

Where J is the combined inertia of rotor and load. F is the combined viscous friction of rotor and load. θ is the rotor angular position. T_m is the shaft mechanical torque.

The Simulink model of the flywheel energy storage is shown in Figure 2.46.

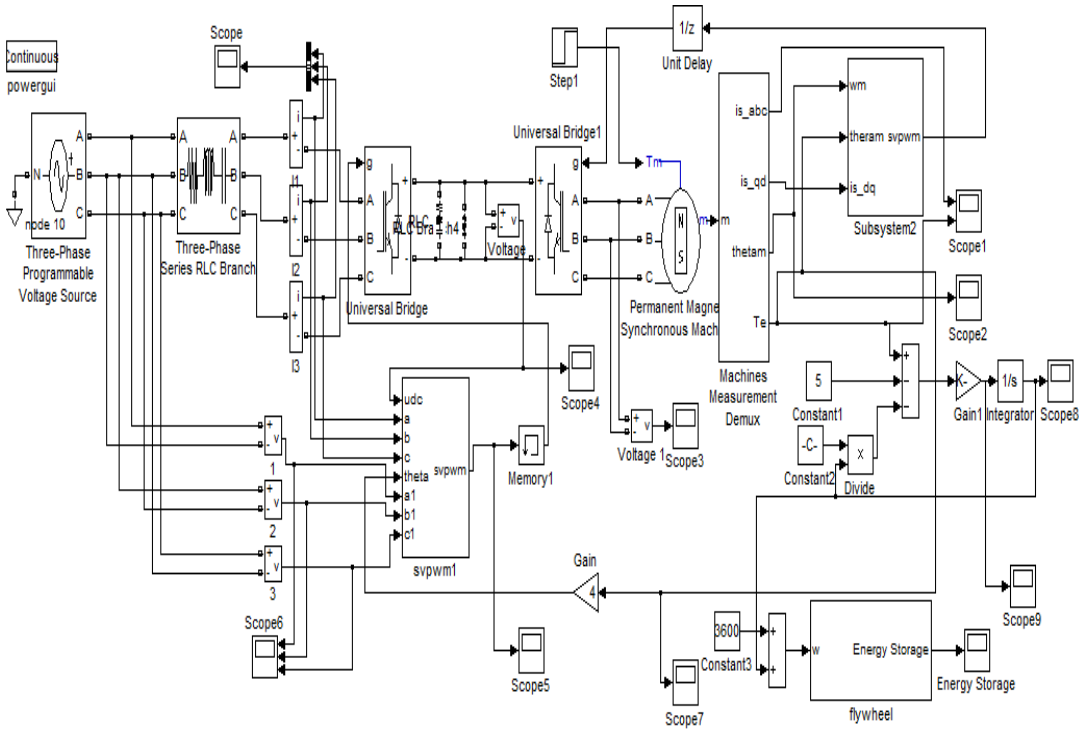

Figure 2-46. The flywheel model in Matlab/Simulink

The flywheel energy storage subsystem is shown in Figure 2-47. In the simulation, the inner diameter is 20cm and the length is 5cm.

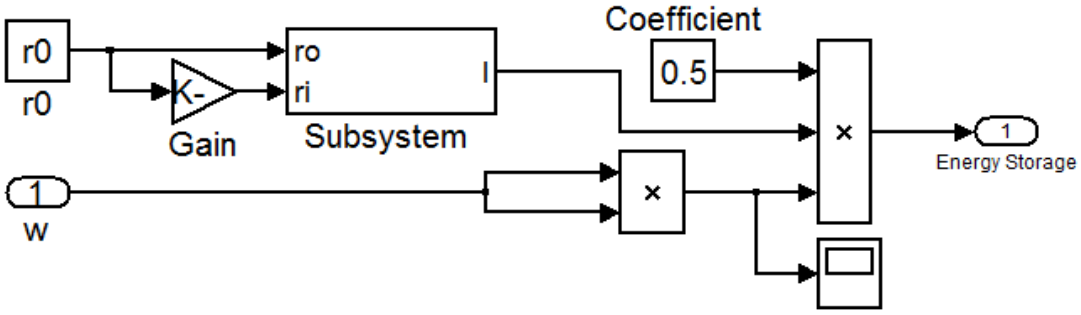

Figure 2-47. Flywheel energy storage subsystem

The AC power converter plays an important part in energy transformation and power transmission. It is mainly composed of an inverter and a rectifier. The universal bridge blocks are available in the standard SimPowerSystems library.

Sinusoidal PWM is a very popular technique used in AC motor control. This relatively unsophisticated method employs a triangular carrier wave modulated by a sine wave and the points of intersection to determine the switching points of the power devices in the inverter. However, this method is unable to make full use of the inverter's supply voltage and the asymmetrical nature of the PWM switching characteristics produces relatively high harmonic distortion in the supply. Space Vector PWM (SVPWM) is a more sophisticated technique for generating a fundamental sine wave that provides a higher voltage to the motor and lower total harmonic distortion, it is also compatible for use in vector control (Field orientation) of AC motors [35]. The switching vectors, the voltage reference and the boundaries between the controllable ranges, the six-step operation and over-modulation are shown in Figure 2-48.

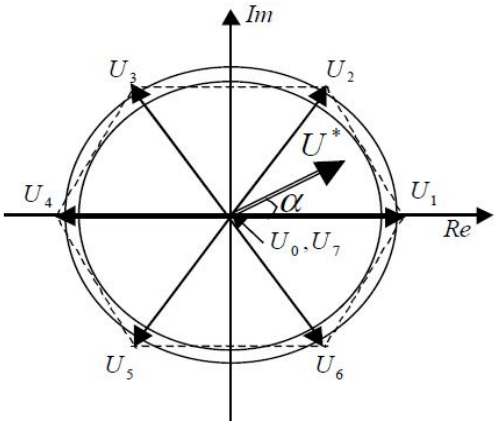

Figure 2-48. Voltage reference and switching-state vectors in SVPWM

Using Clarke-Park transformation, three phase current vectors are converted to a two-dimensional rotating reference frame (*d*-*q*) from a three-dimensional stationary reference frame. The "*d*" component represents the flux producing component of the stator current and the "*q*" component represents the torque producing component. Then these two decoupled components can be independently controlled by passing though separate PI controllers. Closed loop current control and speed control are used. The PI speed regulator with output limits is used for speed regulation. Compared with the speed reference, the generator/motor speed can be adjusted very well. The Proportional plus Integral (PI) type current regulator is also provided.

The outputs of the PI controllers are transformed back to the three-dimensional stationary reference plane using the inverse of the Clarke-Park transformation. The corresponding switching pattern is pulse width modulated. The SVPWM subsystems are shown in Figures 2-49 and 2-50.

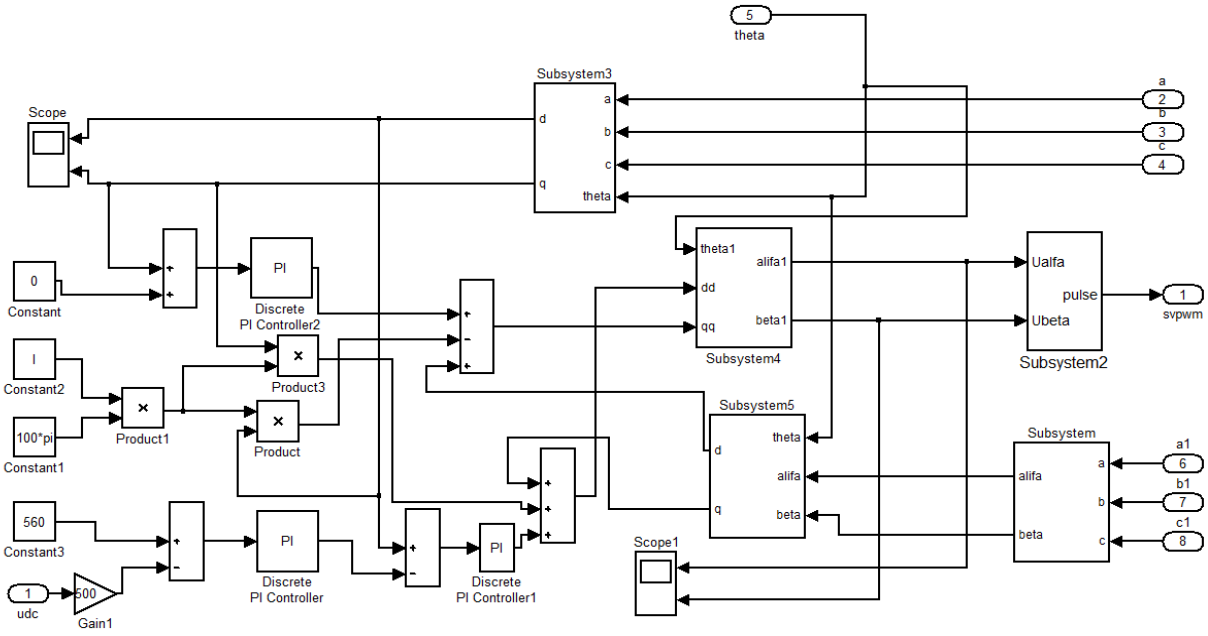

Figure 2-49. SVPWM subsystem 1 in the flywheel model

For flywheels, the depth of discharge (DOD) is defined as

$$a = 1 - \frac{\omega_{\min}^2}{\omega_{\max}^2} \tag{2.39}$$

Flywheels store energy mechanically in the form of kinetic energy. They take an electrical input to accelerate the rotor up to speed by using the built-in motor, and return the electrical energy by using this same motor as a generator. In the discharge mode, the mechanical

torque is -100Nm initially and removed at t=0.6s. In the charge mode, the mechanical torque 100Nm is applied initially and removed at t=0.6s. The simulation results in both the discharge and charge mode show the excellent correspondence with that expected. In future, the individual flywheel model will be incorporated into a more advanced and complicated Microgrid test system.

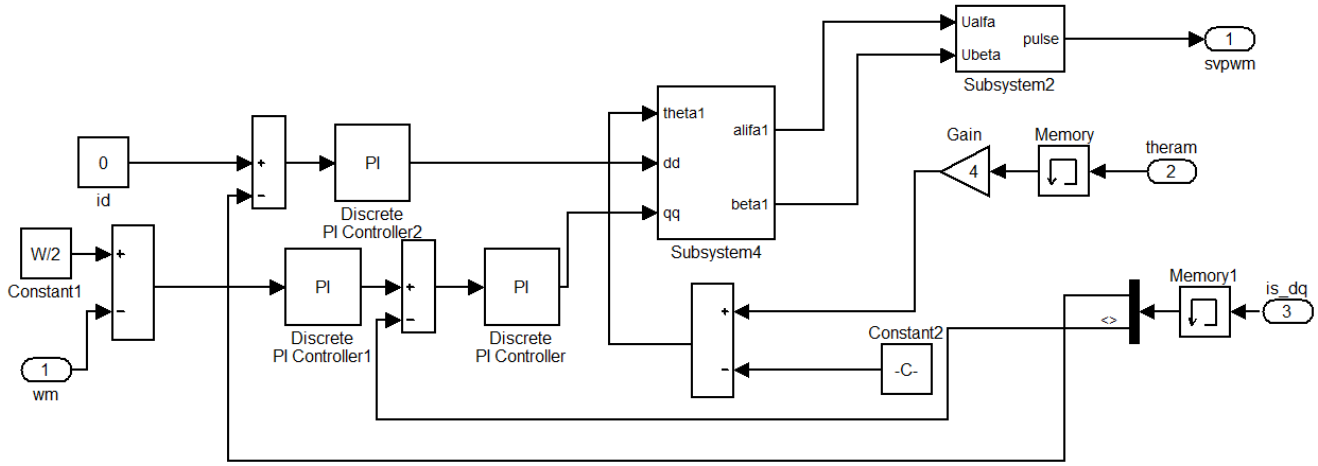

Figure 2-50. SVPWM subsystem 2 in the flywheel model

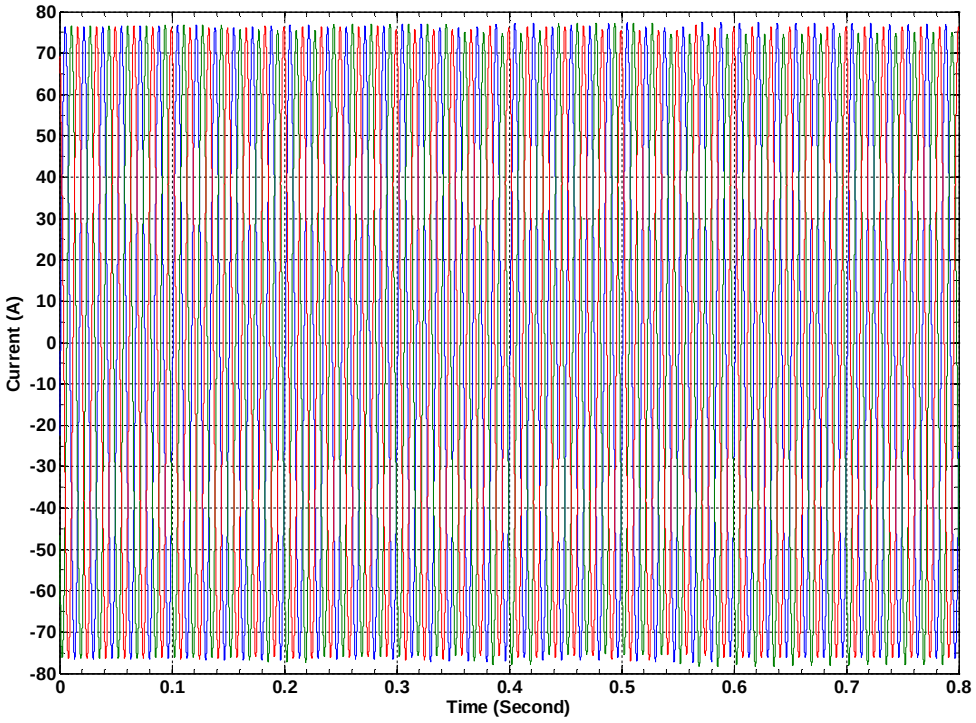

Figure 2-51. Flywheel simulation: current on the power grid side

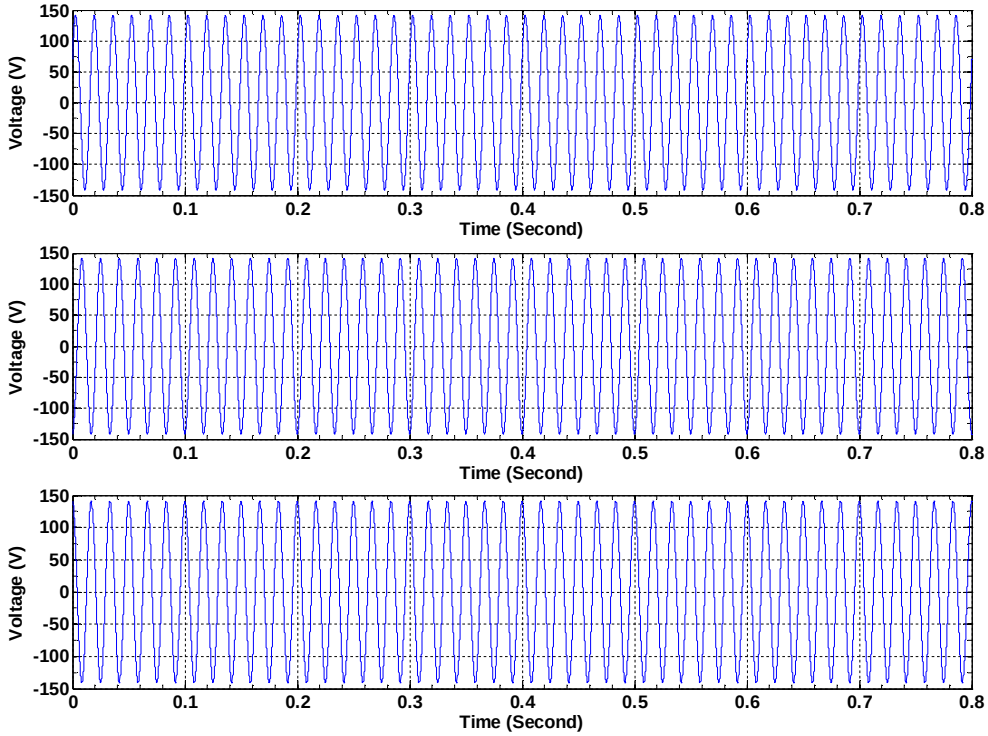

Figure 2-52. Flywheel simulation: three phase voltage on the power grid side

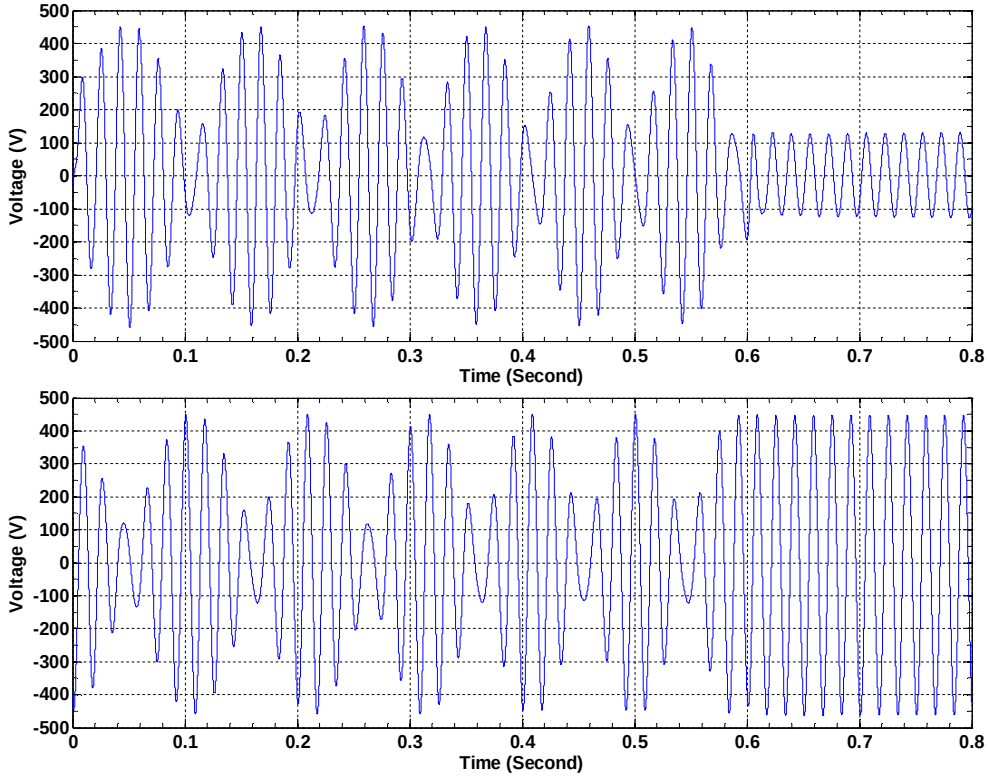

Figure 2-53. Flywheel simulation: d-q voltage in discharge mode

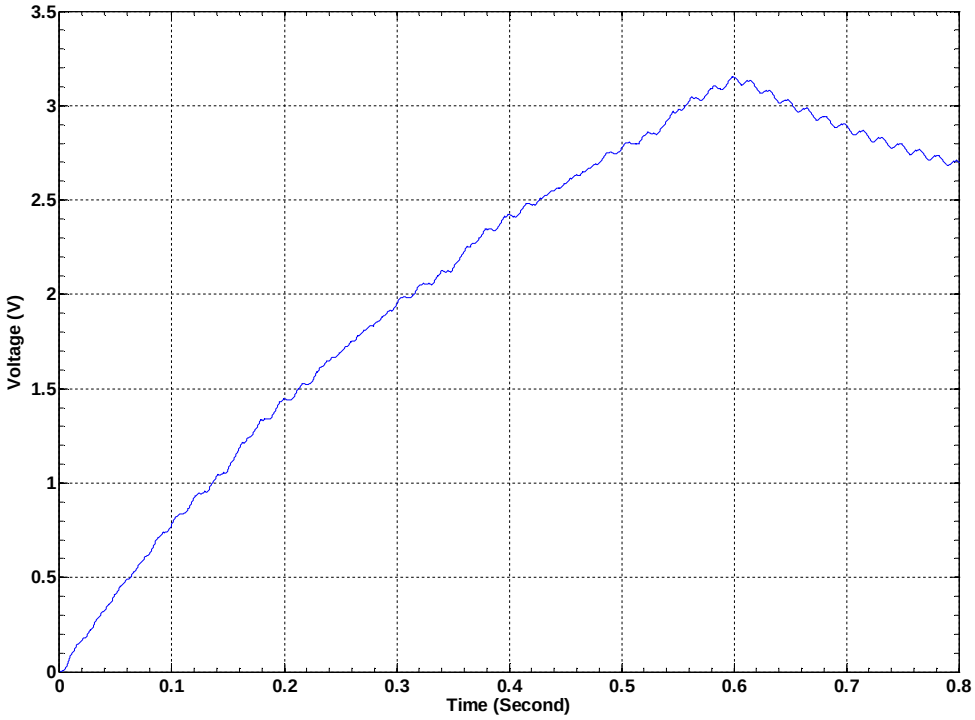

Figure 2-54. Flywheel simulation: DC voltage in discharge mode

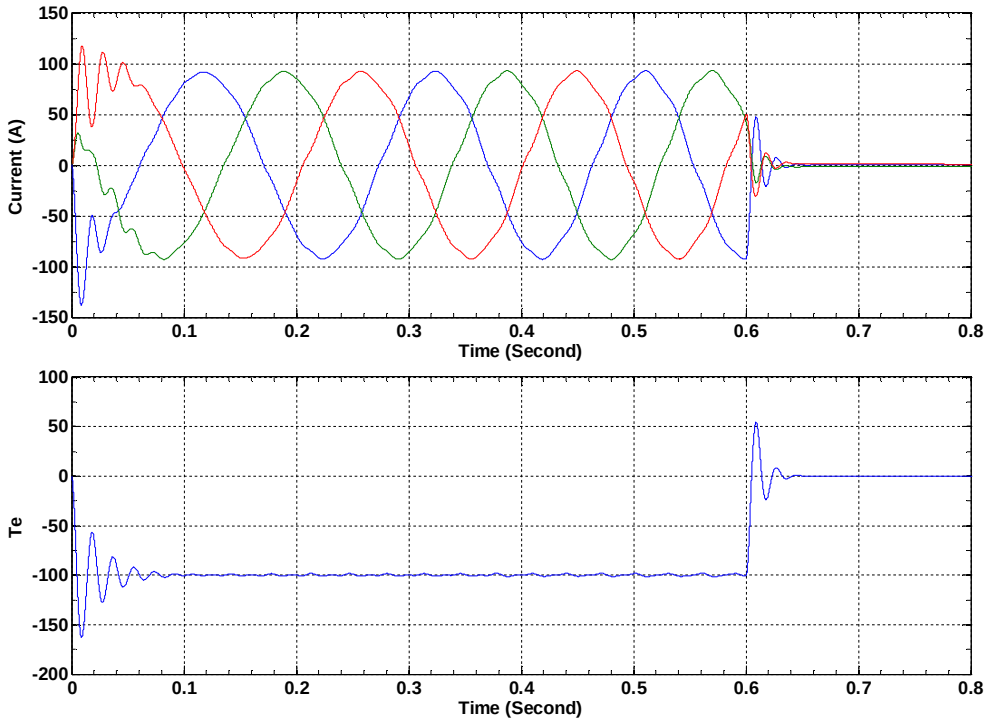

Figure 2-55. Flywheel simulation: abc current and Te in discharge mode

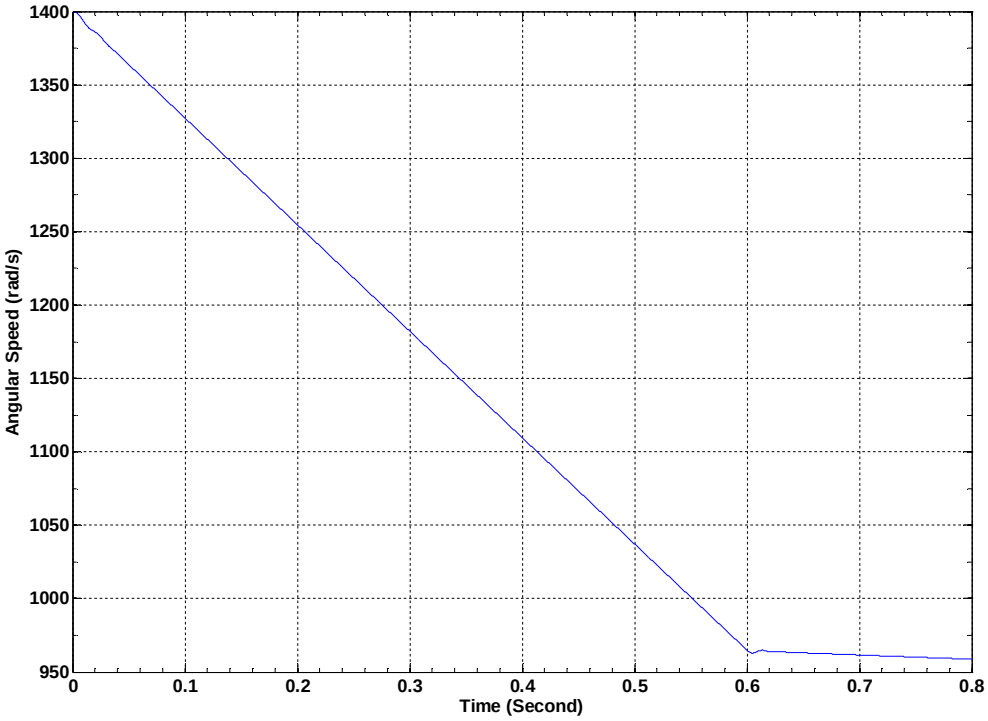

Figure 2-56. Flywheel simulation: angular speed in discharge mode

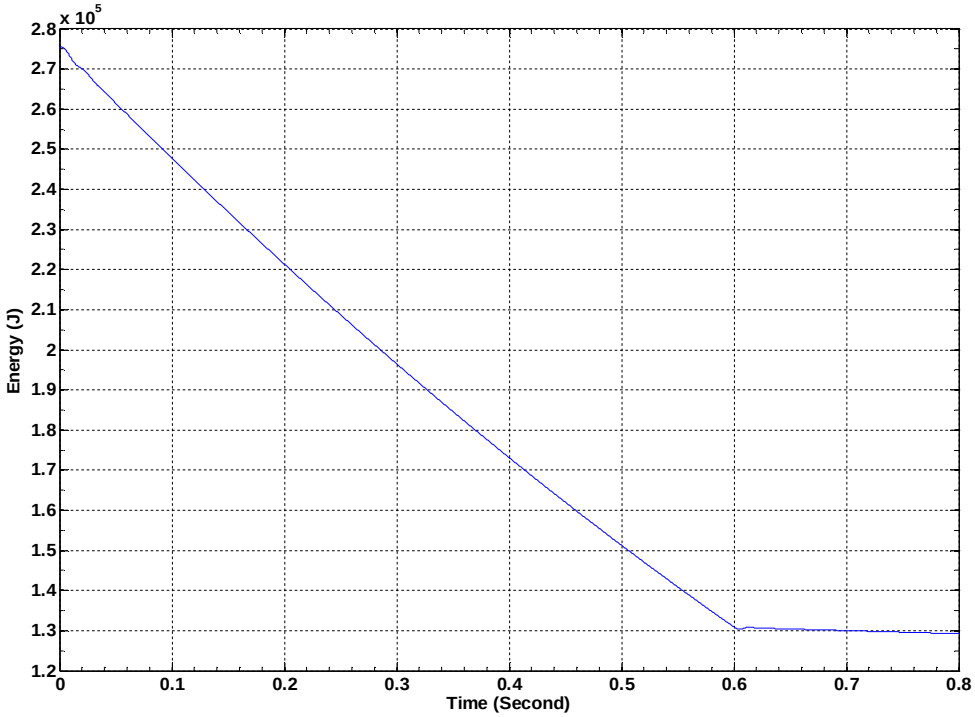

Figure 2-57. Flywheel simulation: energy change in discharge mode

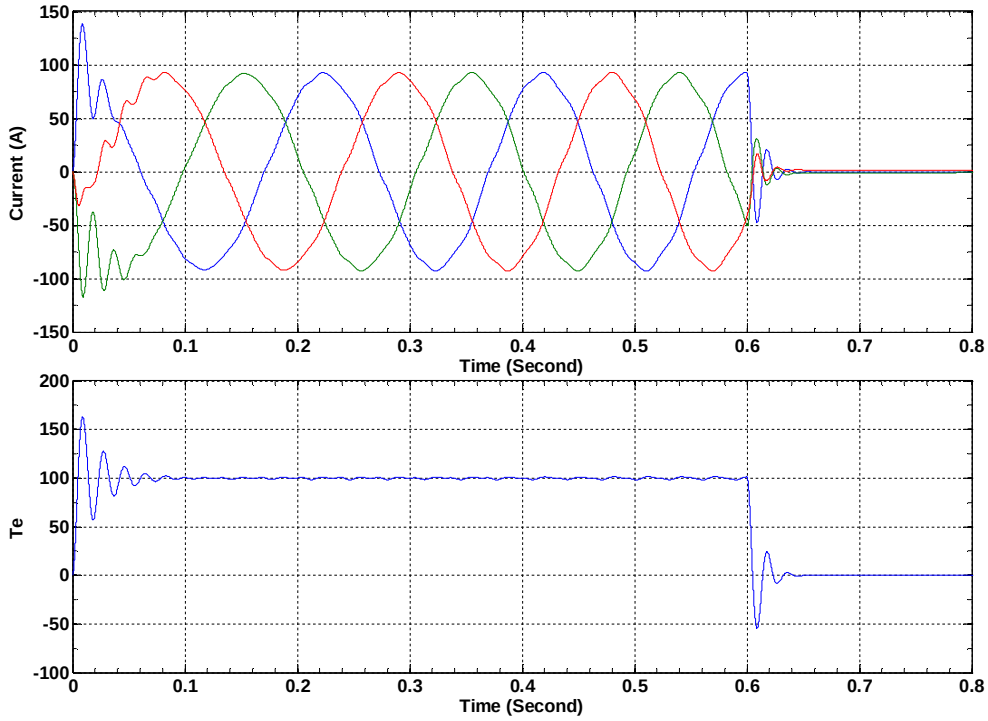

Figure 2-58. Flywheel simulation: abc current and Te in charge mode

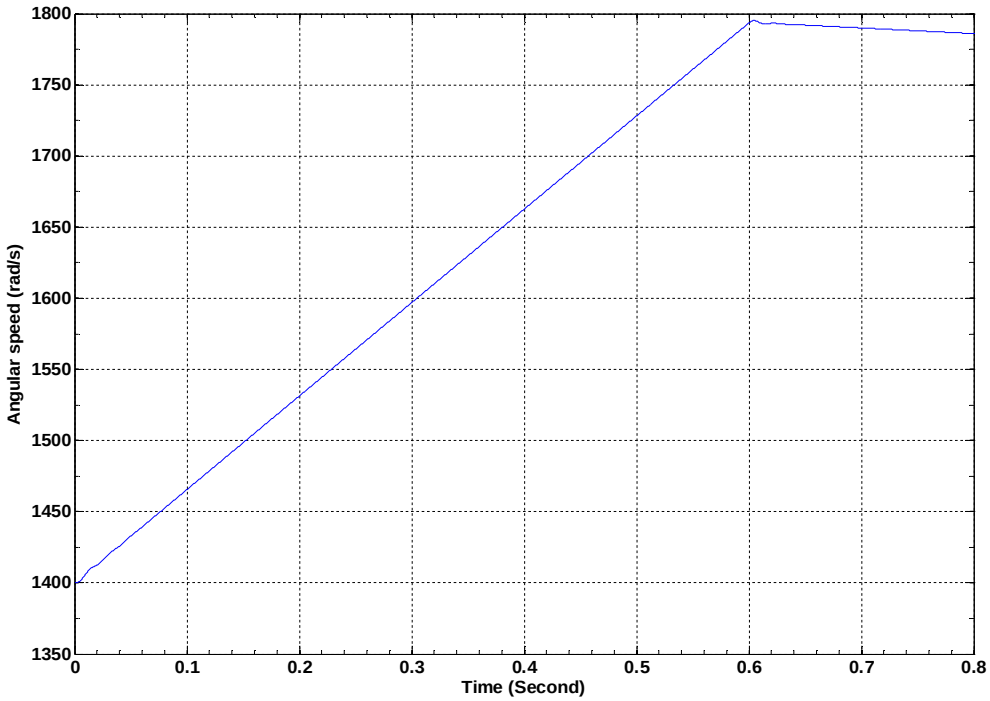

Figure 2-59. Flywheel simulation: angular speed in charge mode

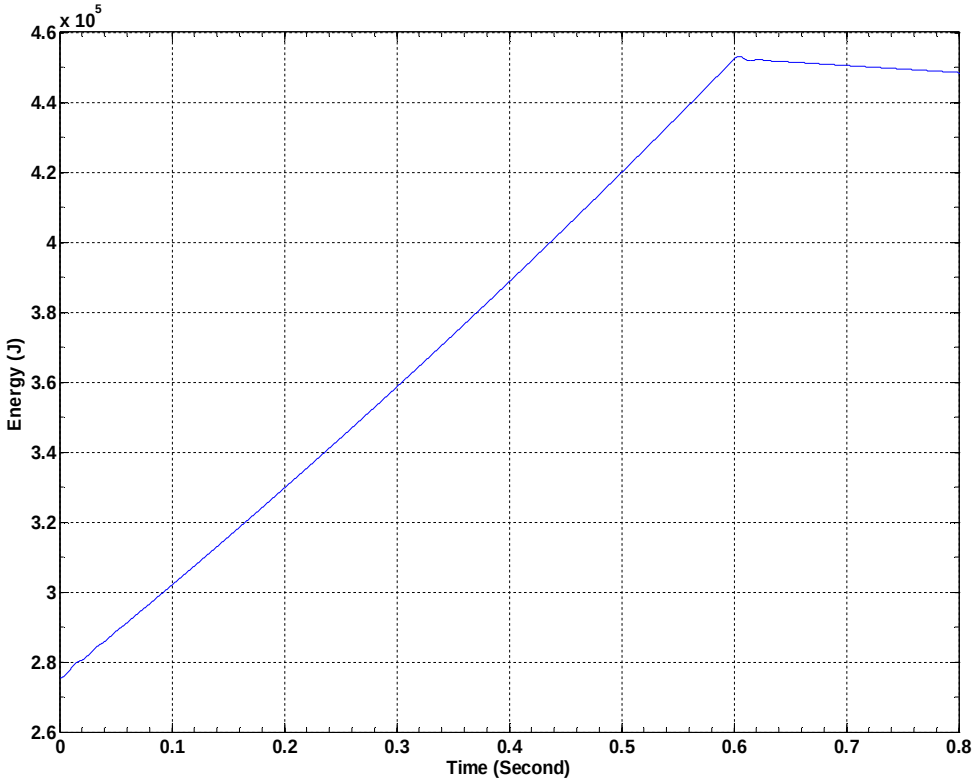

Figure 2-60. Flywheel simulation: energy change in charge mode

2.5.3 Supercapacitor

The Supercapacitor, also known as ultra-capacitor, is the electrochemical capacitor that has higher energy density than common capacitors on the order of thousands of times.

In a conventional capacitor, energy is stored by the removal of charge carriers. This charge separation creates a potential between the two plates, which can be harnessed in an external circuit. The total energy stored in this fashion is proportional to both the number of charges stored and the potential between the plates. The number of charges stored is essentially a function of size and the material properties of the plates, while the potential between the plates is limited by the dielectric breakdown. Different materials sandwiched between the plates to separate them result in different voltages to be stored. Optimizing the material leads to higher energy densities for any given size of capacitor [36].

In contrast with traditional capacitors, Supercapacitor does not have a conventional dielectric. Rather than two separate plates separated by an intervening substance, these capacitors use "plates" that are in fact two layers of the same substrate, and their electrical properties, the so-called "electrical double layer", result in the effective separation of charge despite the

vanishingly thin (on the order of nanometers) physical separation of the layers. The lack of need for a bulky layer of dielectric permits the packing of "plates" with much larger surface area into a given size, resulting in their extraordinarily high capacitances in practical sized packages.[36]

To further analyze the dynamic behavior of the supercapacitor, extensive measurements are made on different supercapacitors with various working conditions. Reference [37] states that a supercapacitor can be modeled using standard circuit components shown in Figure 2-61.

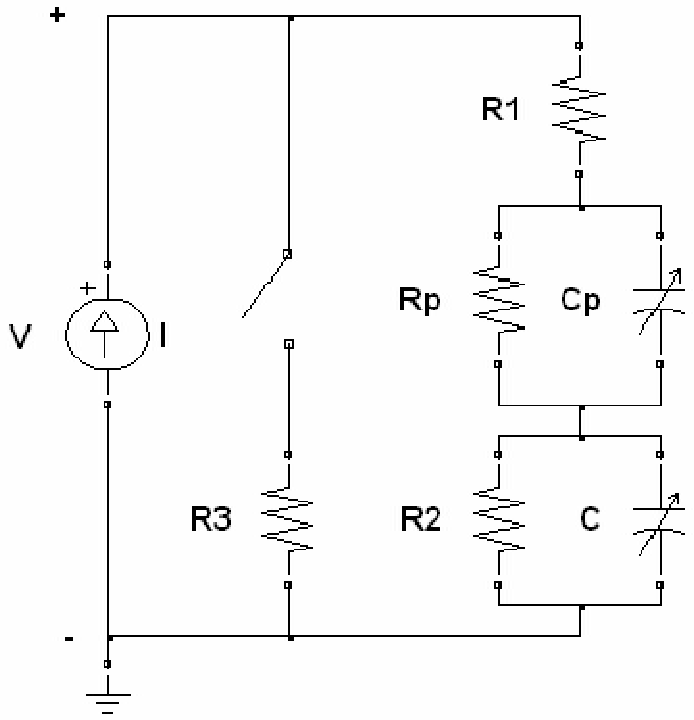

Figure 2-61. Two level Supercapacitor Model

The capacitance C is responsible for the most important phenomenon in the model. It determines the amount of energy stored in the circuit and the rate of energy level variations. The resistance *R2* that is connected in parallel with the capacitor is meant to represent the self discharge effect. The series resistance *R1* represents the energy losses during charge and discharge. These losses occur because the conducting element in the supercapacitor has a resistance, so the connection is not ideal. The over voltage protection provided by *R3* and the switch controlling its connection to the circuit is necessary to prevent damage to the capacitor elements by balancing the voltage level. The voltage balancing is needed because otherwise the voltage in one separate cell can increase higher than the others resulting in gassing or explosion. This voltage difference can occur if one cell has a lower capacitance than the others, since that results in more energy being stored. The resistance *Rp* and the capacitance *Cp* are included in the

circuit to model some of the fast dynamics in the behavior of the supercapacitor [37]. But the most obvious drawback of this equivalent circuit is that the modeling heavily relies on a series of test. In this case, the high accuracy is not of my most interest. A simplified model is carried out without comprising the accuracy too much.

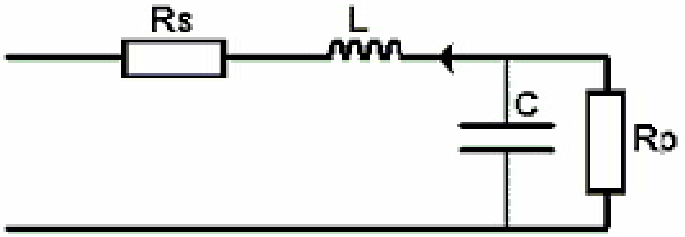

Figure 2-62. A simplified supercapacitor model

Alternately, the classical equivalent circuit model for the supercapacitor is shown in Figure 2-62. The model consists of the capacitance *C*, the equivalent series resistance *Rs*, and the equivalent parallel resistance *Rp*. The *Rs* is responsible for the internal heating loss in the capacitor and is most important during charging and discharging. The *Rp* represents the self-discharge effect and will impact the long-term performance of the supercapacitor. The small inductor *L* results primarily from the physical construction of the supercapacitor. Since the DC current is applied during discharging and recharging, it is possible to eliminate the inductor term. If the simulation time is much larger than the self-discharge time, the equivalent parallel resistance might be neglected as well.

The actual capacity C varies with quantities as current, voltage and temperature. If the nonlinear behavior of the capacitance is ignored, it is sufficient to use a standard capacitor with ac constant value. Otherwise, it is better to embed these relationships into the model than to simply have a constant C all the time. The manufactures datasheet has been implemented in the Look-Up Tables. Because the supercapacitors are really sensitive to overvoltage. The capacitor may not be charged with voltages above its rated maximum voltage. Thus in Simulink model, the relay block controls the switch status in order to keep the voltage from rising too high.

The Supercapacitor can be parallel connected to the main DC link by means of a bidirectional DC/DC converter. It has relatively fast response.

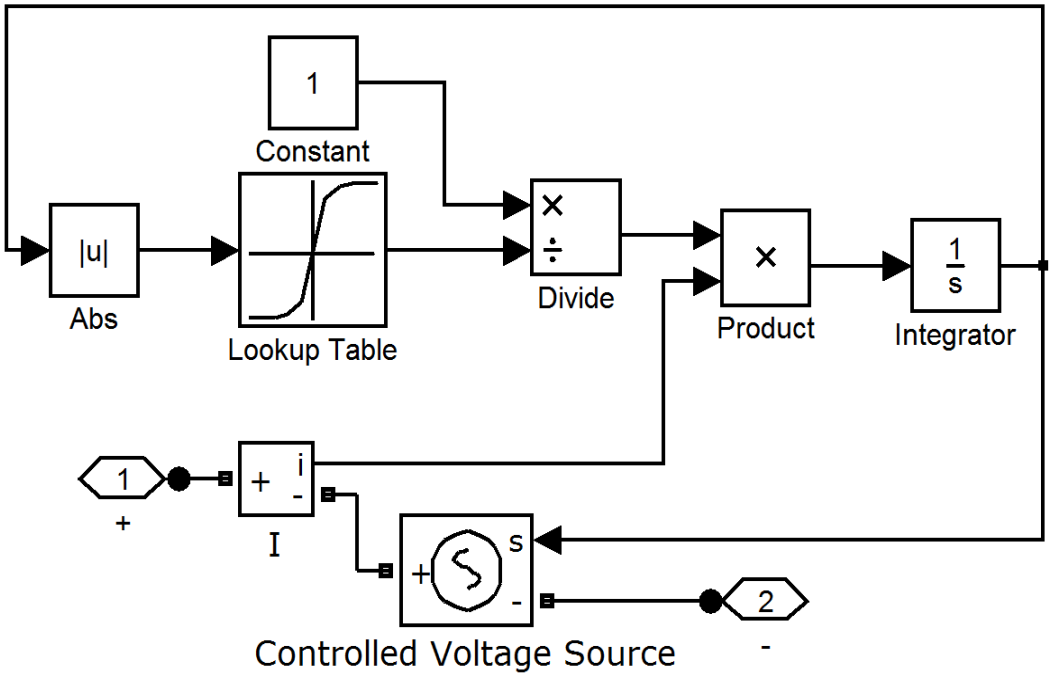

Figure 2-63. Non-linear C in supercapacitor model using controlled voltage source

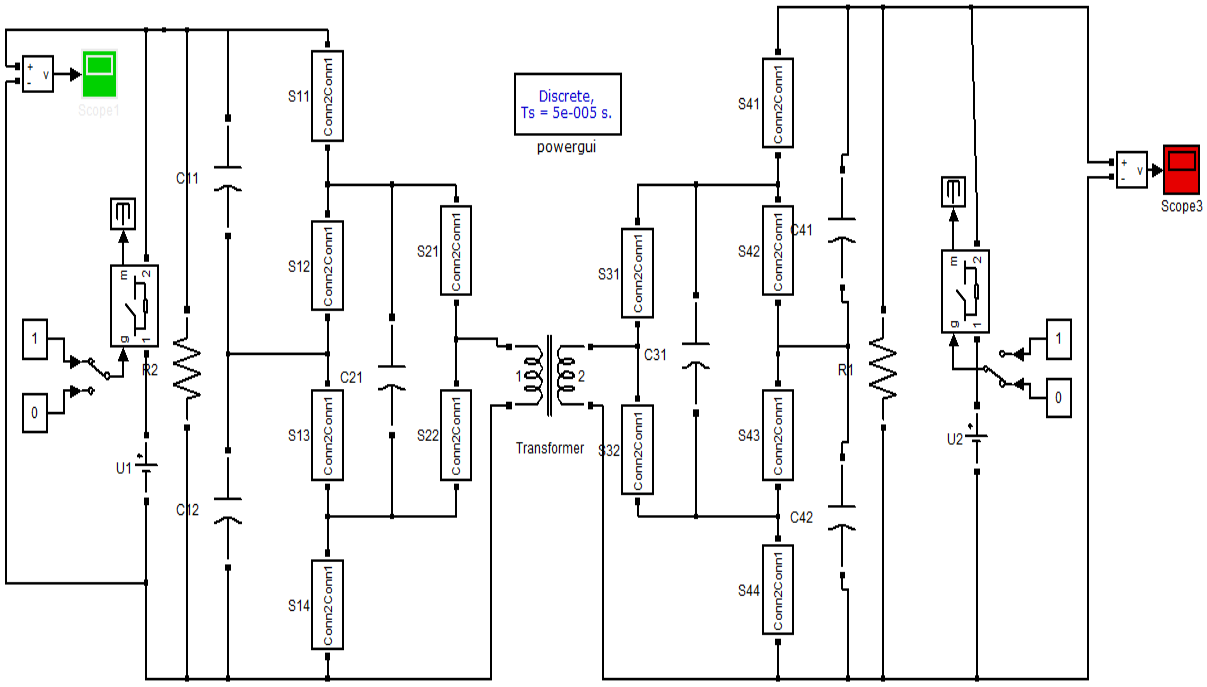

Figure 2-64. Bidirectional DC/DC converter in Matlab/Simulink

2.5.4 Pumped Hydro Storage

This type of energy storage stores up energy in the form of water. Pumping is done at time when the supply is larger than the demand. The water is pumped from a lower elevation reservoir to a top reservoir using the low-cost electric power. At peak load period, the stored water is released through turbines. Then the hydro-turbines can be put into operation immediately to release the required energy. Although it always takes more energy to pump the water than that can be obtained from releasing the water, the overall efficiency of the power system will be enhanced. The utilities also can operate the plant at a profit by selling more electricity at a higher price when demand peaks. It is worth mentioning that the pumped hydro storage is the largest-capacity form of available energy storage.

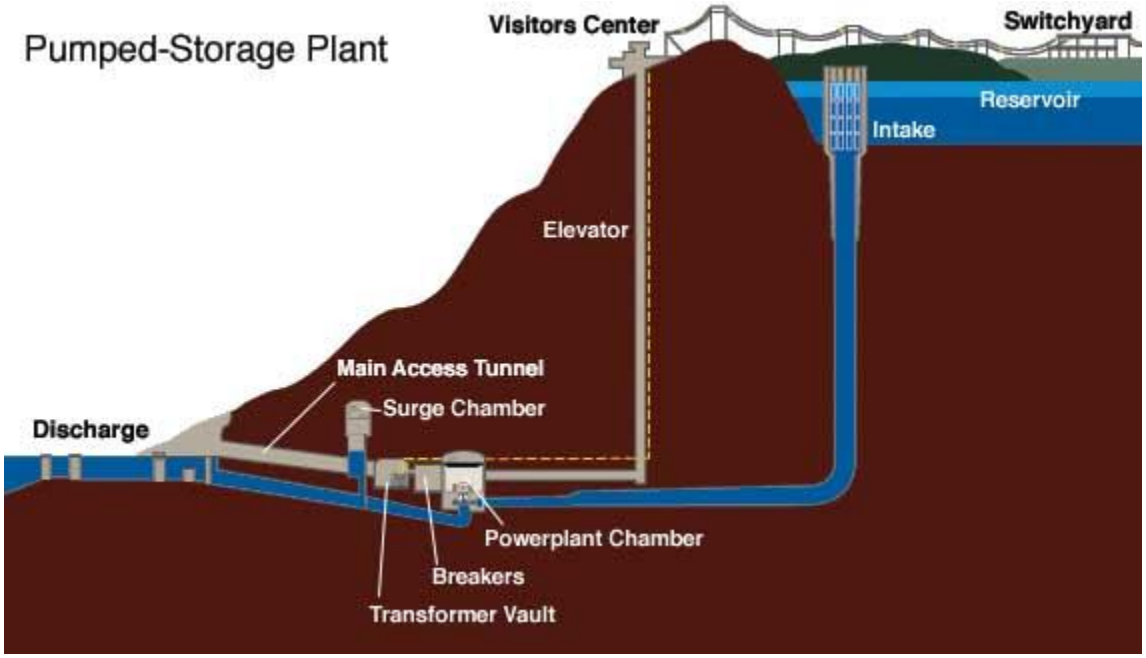

Figure 2-65. Diagram of the TVA pumped storage facility at Raccoon Mountain Plant [38]

The TVA pumped storage plant is shown in Figure 2-65. The Simulink implementation of the pumped hydro storage is shown in Figure 2-66. The detailed description of the pumped hydro storage will be presented in a pending publishing.

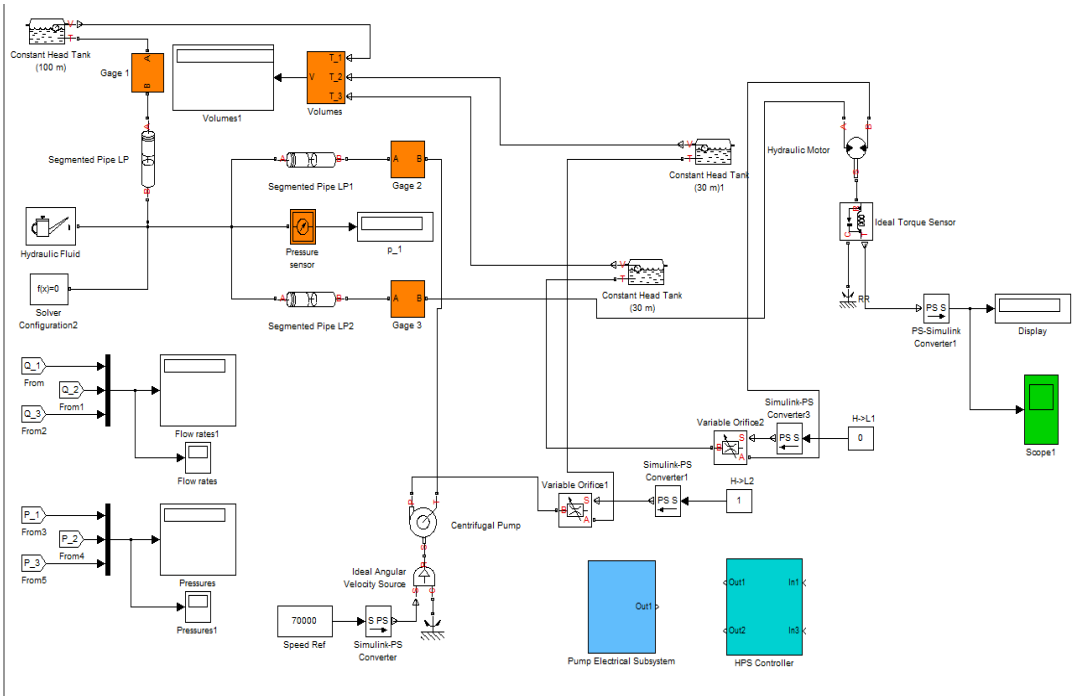

Figure 2-66. Simulink implementation of the pumped hydro storage

2.6 Sample System Modeling

2.6.1 Wind-Diesel Hybrid System

A simulation model for the wind-diesel hybrid system has been developed using Matlab/Simulink. The sample system includes a wind farm, a diesel generator, the main load and the controllable secondary load. User-defined wind data and load profile are used to evaluate the system performance through a variety of simulation case studies. The simulation results indicate the compatibility of the hybrid DG system. In grid-connected mode, the frequency reference is provided by the grid, while it is provided by the controllable secondary load in islanding mode. Figure 2-67 shows the block diagram of the proposed sample system.

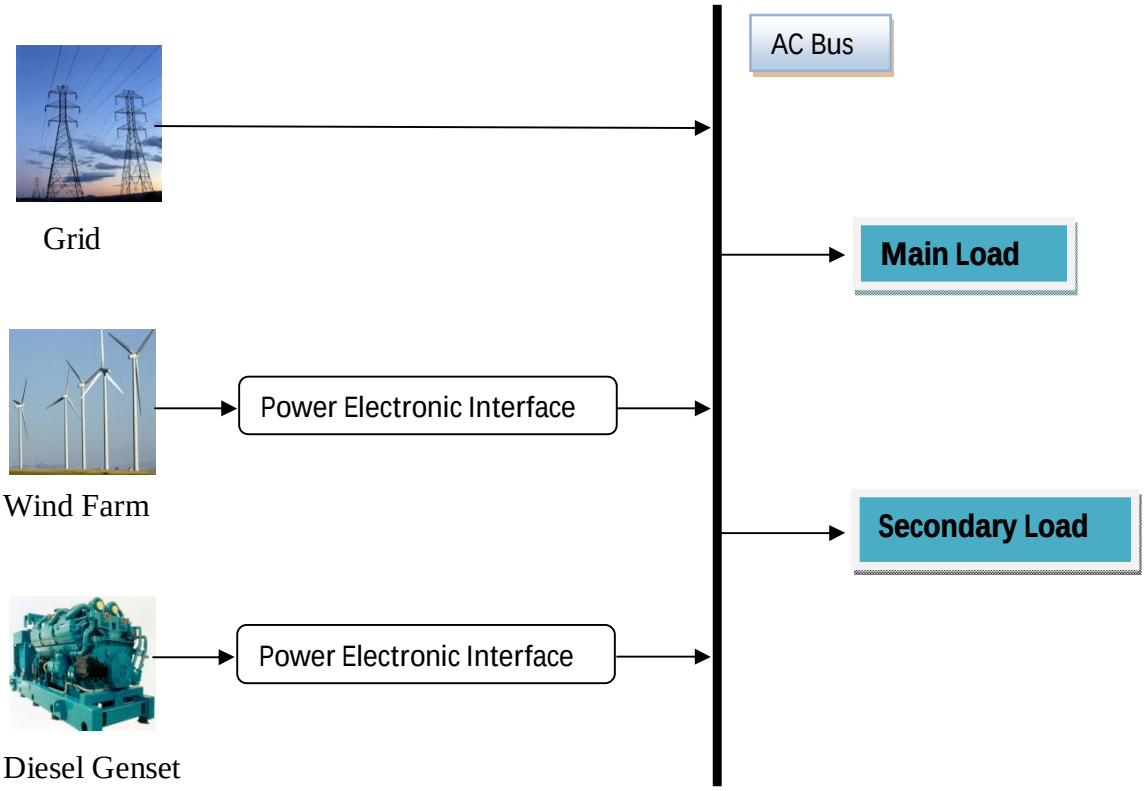

Figure 2-67. The block diagram of the proposed Wind-Diesel system

Case study 1: Off-grid at 5s

In the grid-connected mode, the loads are fed by the grid and the micro-sources at the same time. At t=5s, a three phase ground fault is applied and then the sample system is disconnected with the power grid. In this case, the wind speed remains the same as time changes. The diesel generator will produce more power to compensate the disturbance simultaneously. As a result, the frequency is brought back to 60Hz at around 9s. The transient response can be observed in Figure 2-68. The load side voltage is kept at 1 p.u. The voltage transients following the fault and islanding can be seen in Figure 2-69.

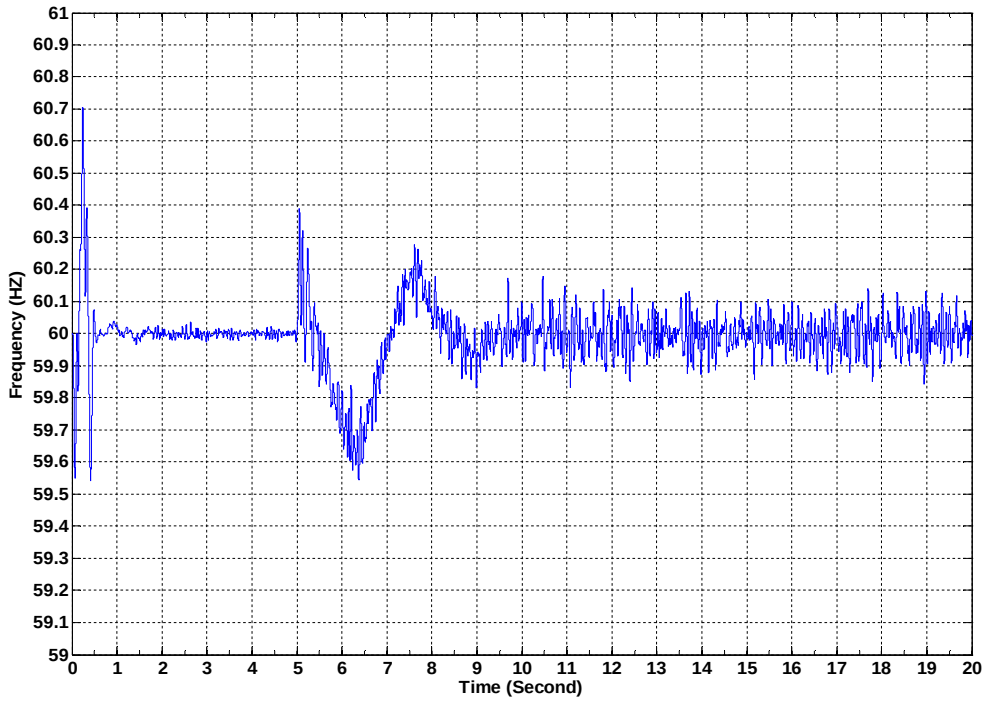

Figure 2-68. System frequency when the Wind-Diesel sample system is disconnected at 5s

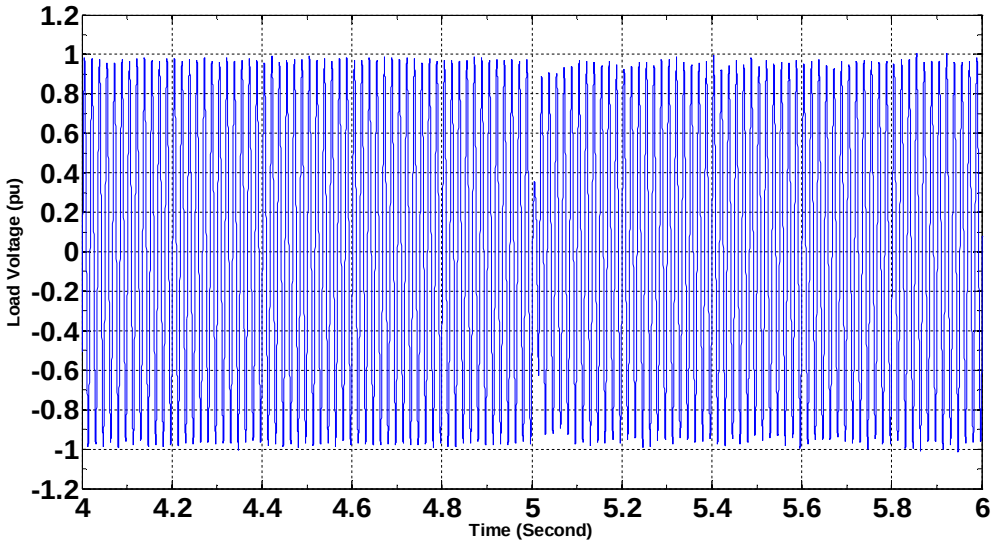

Figure 2-69. Load voltage when the Wind-Diesel sample system is disconnected at 5s

Case study 2: Wind speed changes in islanding mode

The wind speed is generated from a Signal Builder which is available in Matlab/Simulink standard library. As is seen in Figure 2-70, the wind speed increases from 9m/s to 11m/s at the

10th second. In result, the wind generator produce more power to feed the main load as well as the secondary load. When t=10s, the frequency momentarily goes up to 60.62Hz and the controllable secondary load reacts to absorb more power in order to bring the frequency back to the normal value 60Hz. After around 14.5s, the frequency keeps at 60Hz. Figure 2-71 shows the real power output. As the main load is still 100kW, the secondary load absorbs an additional 60kW to maintain a constant 60Hz frequency.

Another test is carried out to examine the dynamic response of the wind farm to random generated wind speed. The pattern of the random wind speed is illustrated in Figure 2-72. The simulation results show the responses of the rotor speed, the frequency, the real power and reactive power in Figures 2-73, 2-74 and 2-75, respectively. The main load power is regulated at the desired value 100KW. The secondary load is robust to maintain a constant 60Hz system frequency.

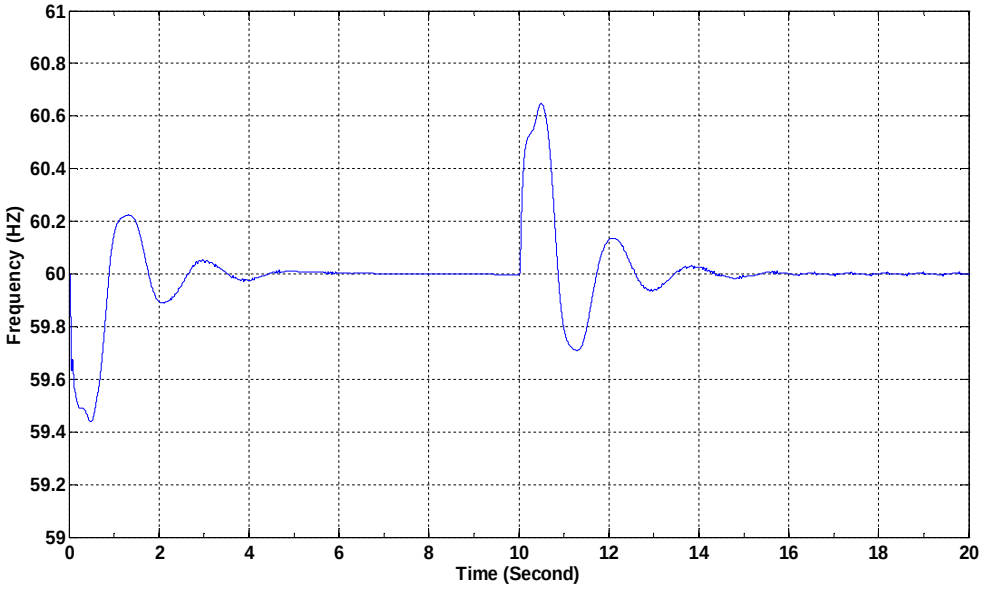

Figure 2-70. System frequency when the wind speed increases at 10s in the islanding mode

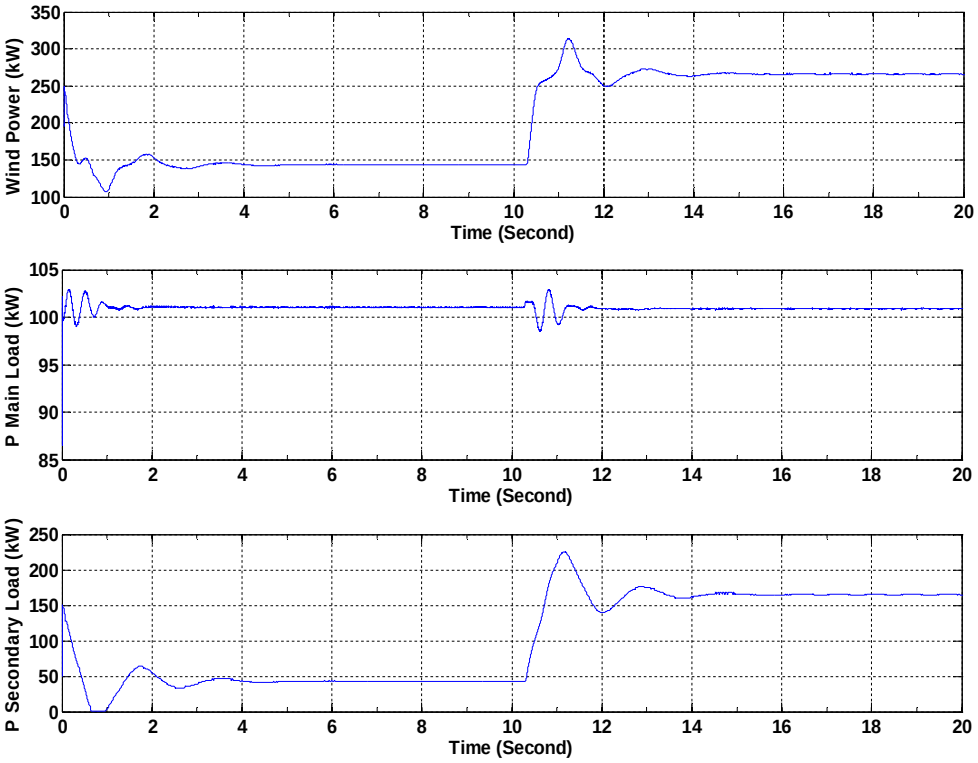

Figure 2-71. Active power when the wind speed increases at 10s in the islanding mode

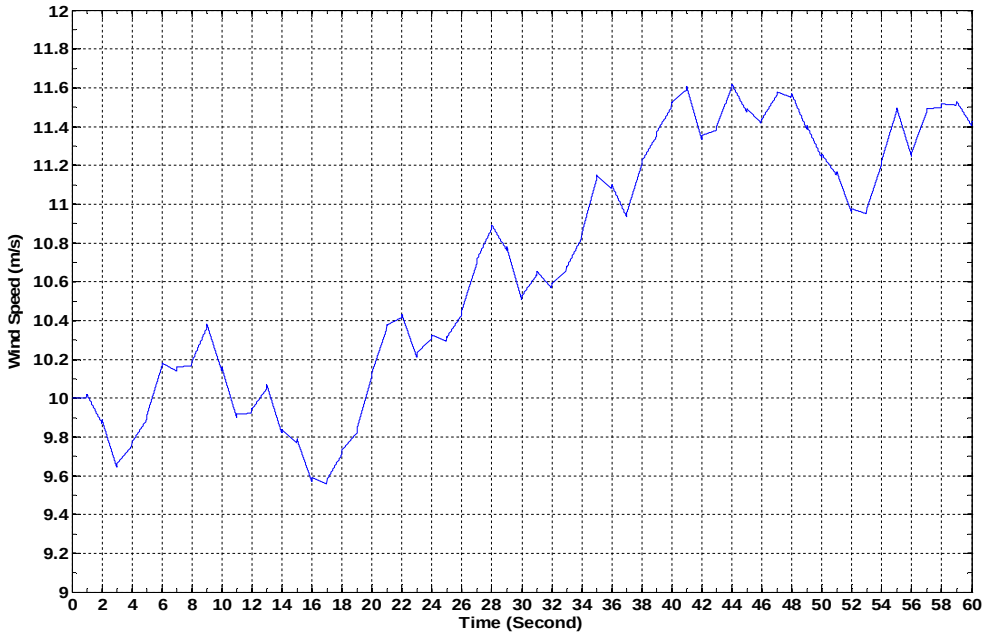

Figure 2-72. Random wind speed during 60s

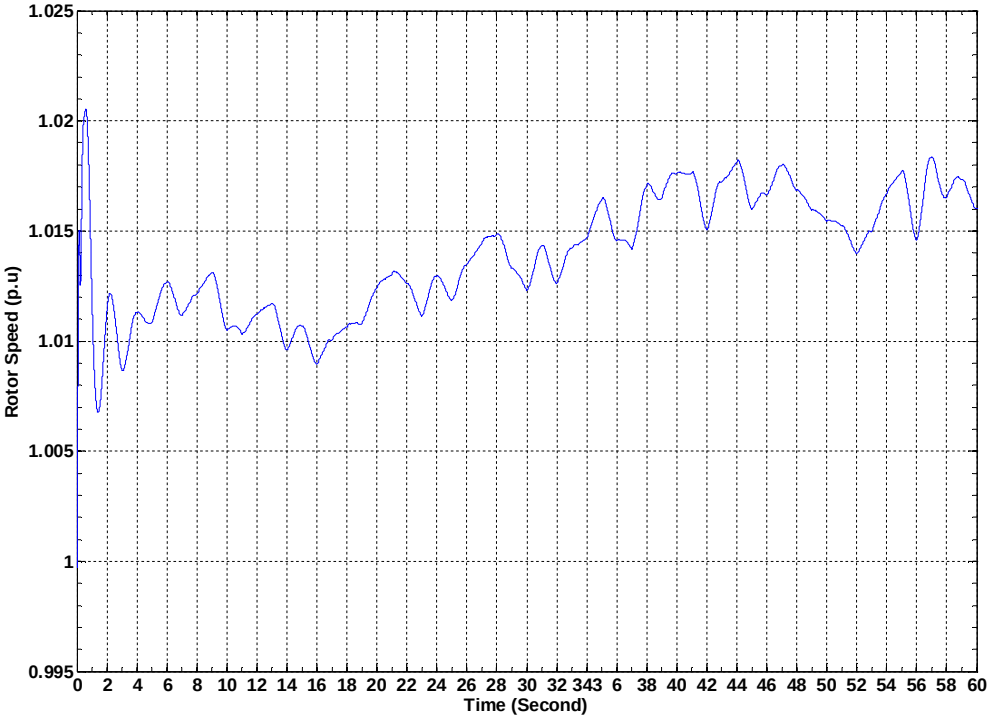

Figure 2-73. Rotor speed response to 60s random wind speed

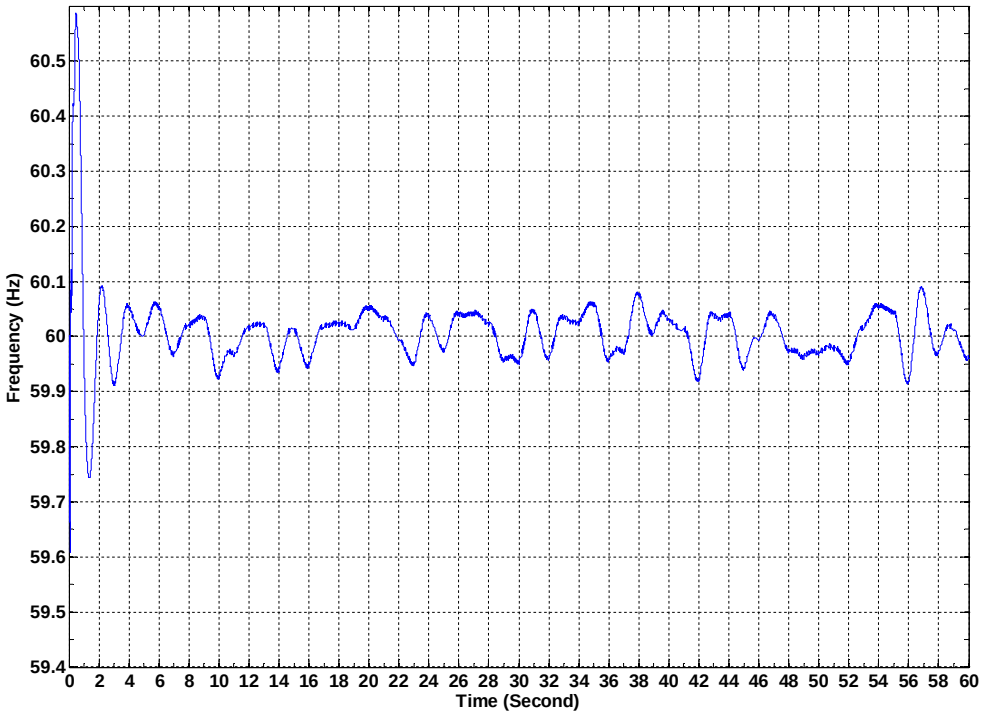

Figure 2-74. System frequency response to 60s random wind speed

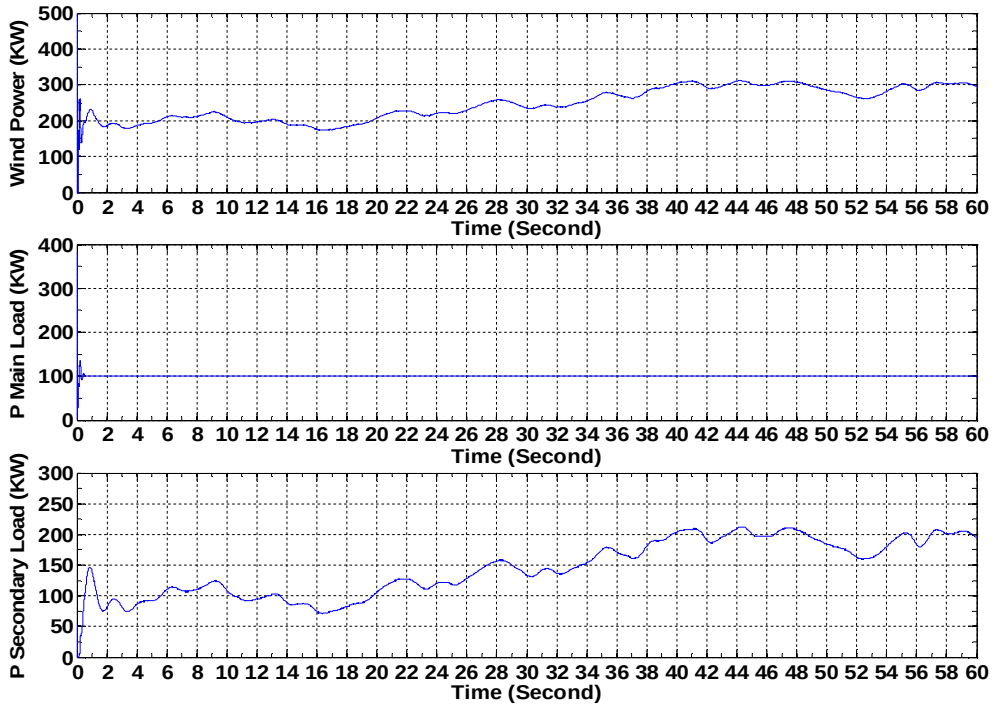

Figure 2-75. Active power response to 60s random wind speed

Case study 3: Load changes in isolated mode

According to turbine characteristics, for a 10 m/s wind speed, the turbine output power is almost 200kW. As the main load is 100kW, the secondary load absorbs 100kW to maintain a constant 60Hz frequency. At t=10s, the additional load of 50kW is switched on. The frequency momentarily drops to 59.7Hz and the frequency regulator reacts to reduce the power absorbed by the controllable secondary load so as to bring the frequency back to 60Hz. The results shown in Figure 2-77 demonstrates the dynamical load sharing between the main load and the controllable secondary load.

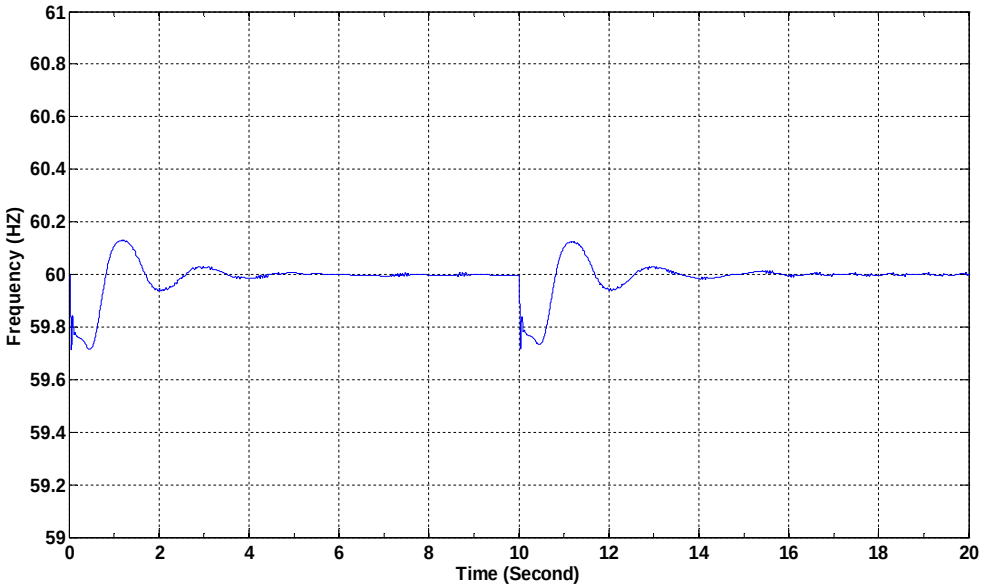

Figure 2-76. System frequency when the main load increases at 10s in the islanding mode

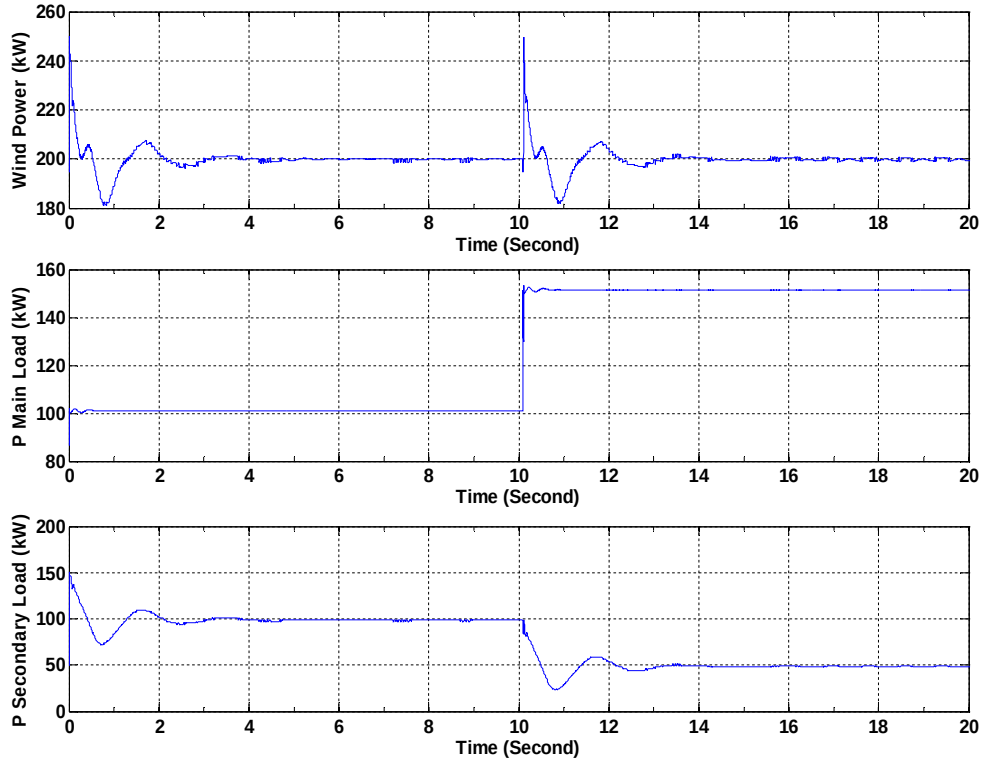

Figure 2-77. Active power when the main load increases at 10s in the islanding mode

In this section, the modeling, control, and power management of a hybrid Microgrid sample system have been analyzed. The hybrid energy system configuration was covered briefly and the details of each component modeling were discussed in the last two chapters. A basic power management strategy that maintains the system stability was implemented.

Different case studies have been carried out to evaluate the dynamics behaviors of the sample system under various disturbances. The simulation results show the feasibility of the proposed power management scheme to meet a desired load demand pattern. In the future work, it is necessary to apply some advanced energy management to reduce the transient time in order to keep a higher level of reliability of power system at the same time.

2.6.2 Fuel Cell-Battery Storage-Dynamic Load Hybrid System

Fuel cells convert the chemical energy in a fuel directly into electricity through an electrochemical reaction. The battery provides bursts of power as a generator essentially when the load increases sharply at peak load period, while it absorbs the excessive energy at low load period.

The electrical subsystem is composed of four parts: the dynamic load, the battery storage, the fuel cell and the DC/DC converter.

1. DC/DC converter is current-regulated to control the power splitting from the battery and the fuel cell.
2. Battery storage is modeled as a 288Vdc, 13.9Ah Nickel-Metal-Hydride battery. The SOC of the battery is initialed to 50%. Its discharge curve is shown in Figure 2-78. Also the simulation results are shown in Figure 2-79.
3. A typical fuel cell only produces a small voltage. To create enough voltage, the fuel cells are layered and combined in series and parallel circuits to form a 288 Vdc, 100 kW Proton Exchange Membrane (PEM) fuel cell stack.
4. Dynamic load is represented by a DC machine which is controllable via an external torque signal.

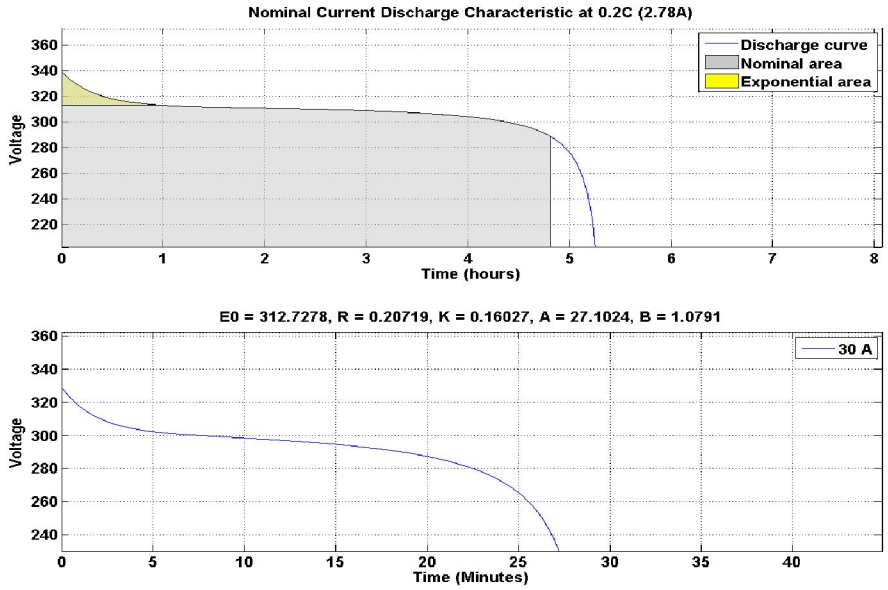

Figure 2-78. Discharge curve of a 288Vdc, 13.9Ah Nickel-Metal-Hydride battery

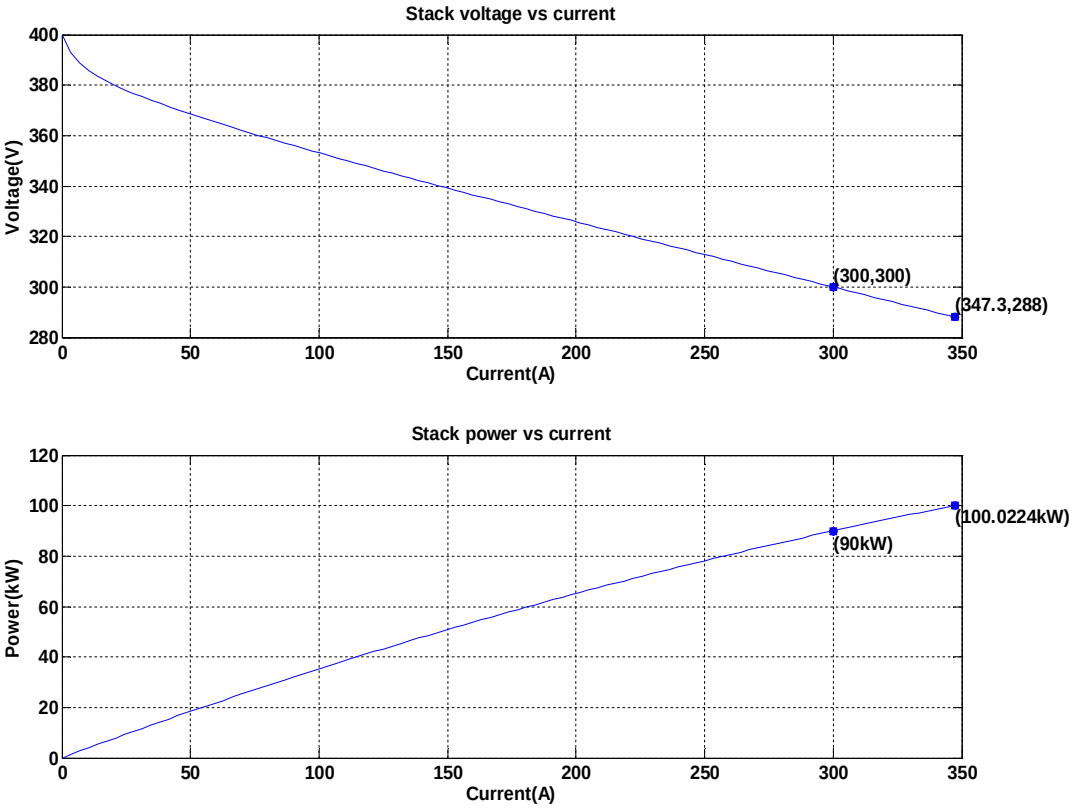

Figure 2-79. Simulation results of a 288Vdc, 100kW PEM fuel cell stack

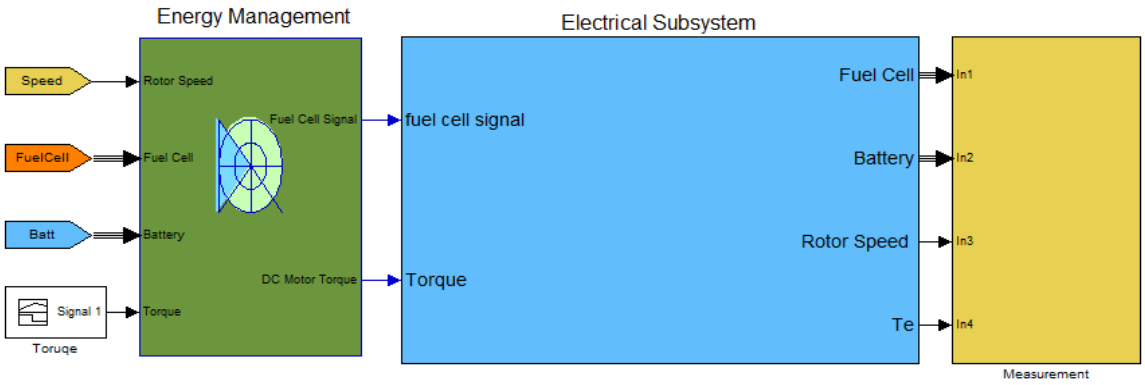

Figure 2-80. Matlab/Simulink model of the fuel cell-battery hybrid system

The final Matlab/Simulink model of the fuel cell-battery hybrid is shown in Figure 2-80. The Energy Management Subsystem receives the reference signals for the load demand and control the fuel cell system and the battery system in order to distribute accurately the power from the two electrical sources. The required load demand is provided by a combination of the two available power source. To prevent the battery from overcharging or over-discharging in working conditions, the Energy Management Subsystem maintains the State-Of-Charge (SOC) between 10 and 90%. Also, it prevents against voltage collapse by controlling the power required from the battery.

As is shown in Figure 2-81, at the beginning of the simulation, the battery provides the required power till the fuel cell starts at around 0.5s. Due to its large time constant, the fuel cell is not able to reach the reference power instantly. Thus the battery continues to provide the power at this moment. Then the fuel cell begins to serve all the load (10kW). At t=5s, an additional 25kW load is switched on. In the Matlab/Simulink model, it can be achieved by controlling the mechanical torque to the DC machine. The fuel cell cannot increase its power instantaneously; therefore the battery produce more power in order to maintain the required torque. As the fuel cell power reaches the reference power, the battery decreases its output. Due to the fuel cell large response time, it takes time to reach the required power. It is slightly different from the reference power. At t=14 s, a 20kW is switched off. The battery helps the fuel cell by absorbing the extra power. The battery power becomes negative. Because the battery receives some power from the fuel cell.

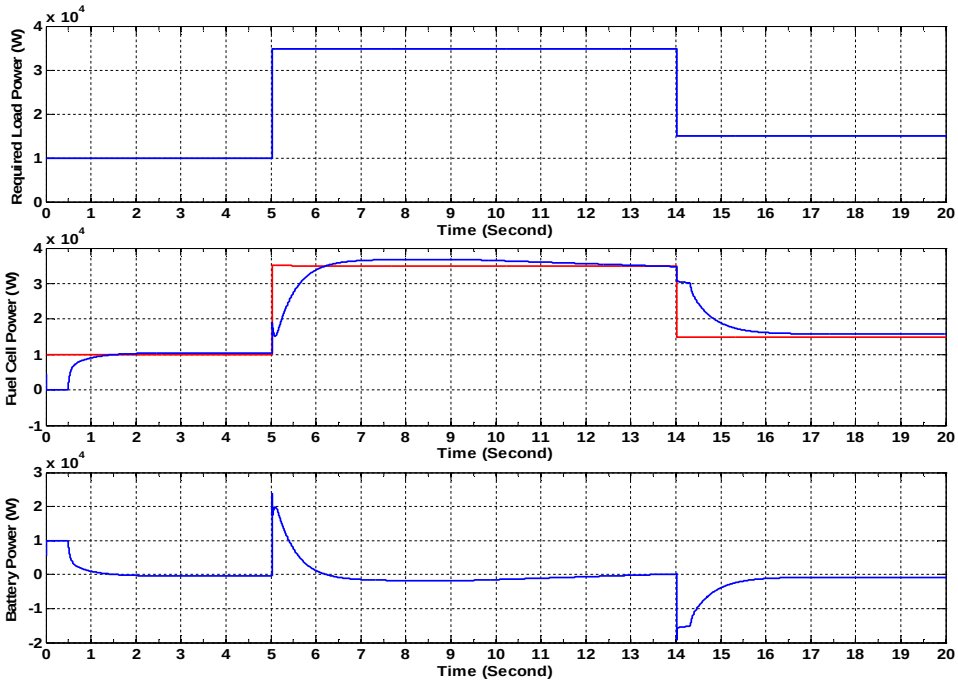

Figure 2-81. Reactive power output of the required load, fuel cell and battery

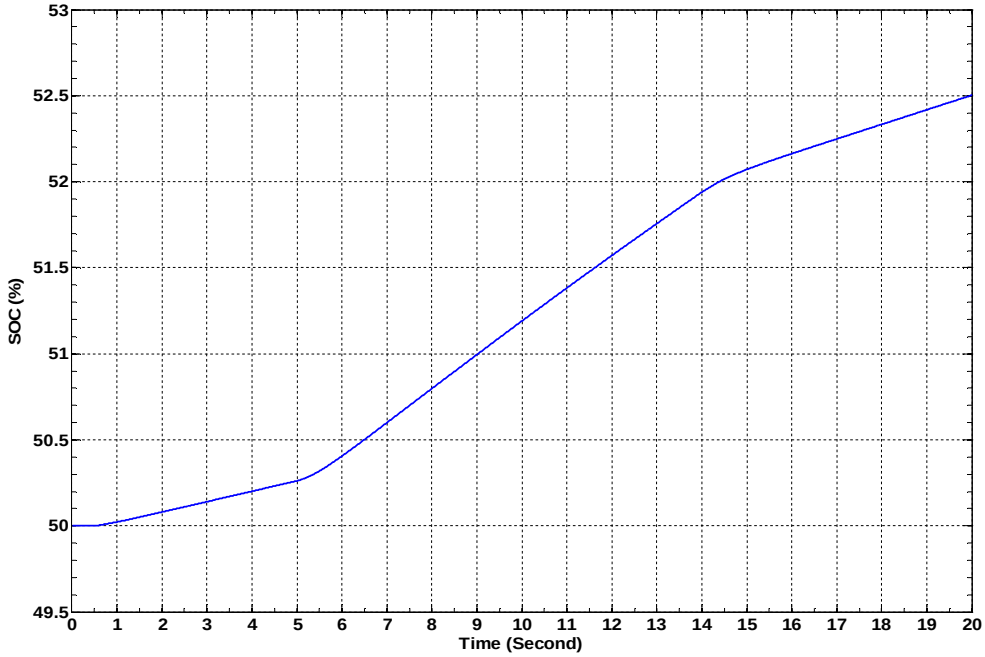

Figure 2-82. Battery SOC in of the fuel cell-battery hybrid system

The State-Of-Charge of the battery storage is shown in Figure 2-82. Initially, it is set to 50%. To prevent the battery from overcharging or over-discharging in working conditions, the Energy Management Subsystem maintains the State-Of-Charge (SOC) between 10 and 90%. In the simulation, it does not reach the upper limit 90% and the lower limit 10%. Reference and

measured current of DC/DC converter are shown is Figures 2-83. The stack consumption of air and fuel are shown in Figure 2-84.

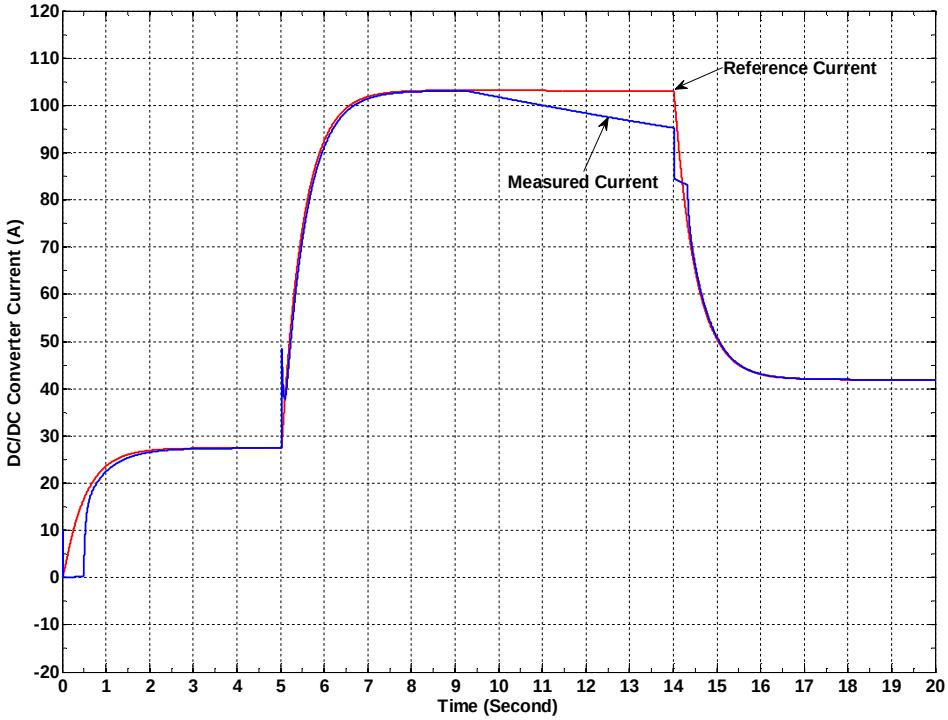

Figure 2-83. Reference and measured DC/DC converter current

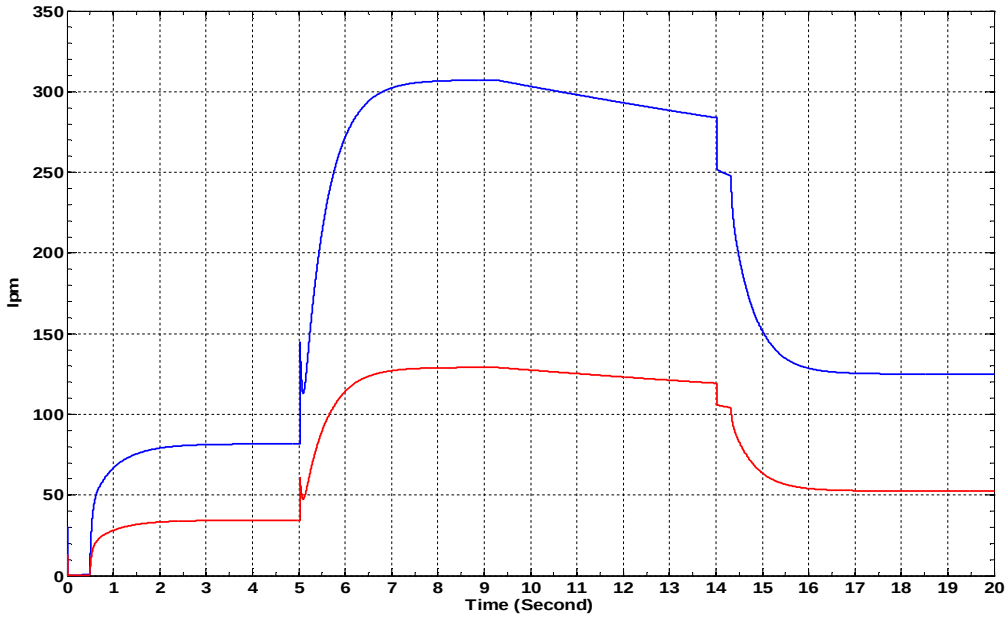

Figure 2-84. Stack consumption of air(blue) and fuel(red)

2.7 Conclusions

To analyze the dynamic performance of Microgird components, proper and accurate models are required for various research purposes. Thus this chapter presents the detailed modeling of DG, loads and transmission lines. All the models obtained from theoretical equations or experimental data have been built in MATLAB/SIMULINK. In addition to the extensive investigation of individual Microgrid components, several sample systems have been carried out to examine the dynamic behavior of the hybrid power.

Chapter 3
Improvements on Microgrid Modeling and Simulation

3.1 RT-LAB (Real-time Simulation)

This chapter presents the basic idea of RT-LAB simulator as well as an overview of the simulation process. The RT-LAB simulation software enables the parallel simulation of power to realize for electrical systems for several drives and electric circuits on clusters of PC running RT-Linux operating systems at sample time below 5 μs . One of the most attractive advantages is that the standard Matlab/Simulink models can be used directly without writing any other code. RT-LAB build computation and communication tasks necessary to effectively make parallel simulation of electrical systems on low cost off-the-shelf PC technology [39].

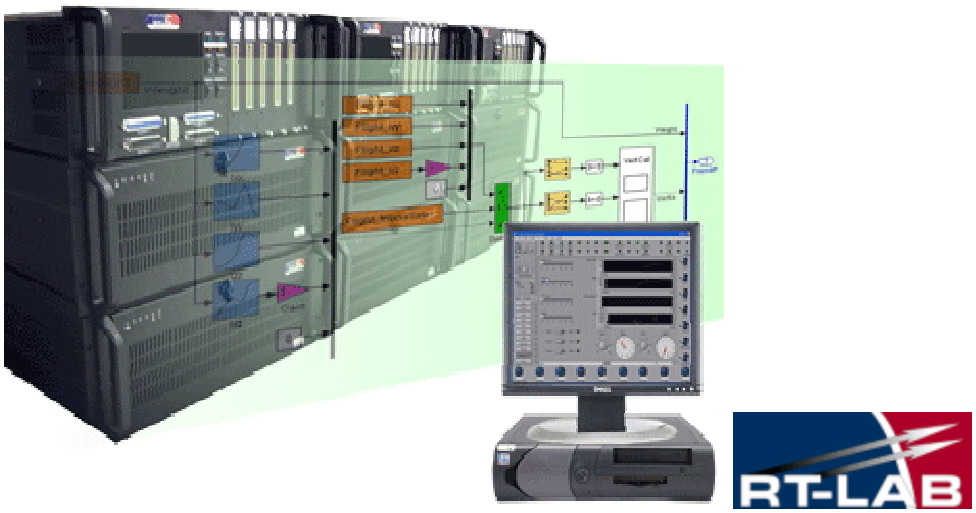

Figure 3-1. RT-LAB configuration

RT-LAB is a distributed real-time platform that facilitates the design process for engineering systems by taking engineers from Simulink or SystemBuild dynamic models to real-

time with hardware-in-the-loop, in a very short time, at a low cost [40]. In the chapter of Microgrid modeling, both the individual DG models and sample systems have been implemented in Matlab/Simulink and run with various test scenarios. When the number of the components is not too large, the execution time is not a big problem. However, as the test system is becoming more complex, a flexible real-time simulator is needed to run the complex simulation for speeding up model execution, control and test.

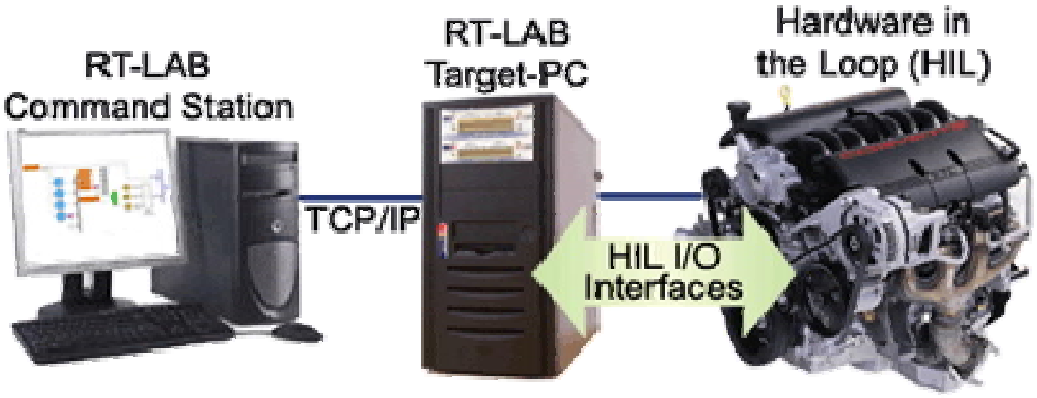

Figure 3-2. RT-LAB Single Target Configuration [41]

In RT-LAB single target configuration typically used for rapid control prototyping, a single computer runs the plant simulation or control logic. One or more hosts may connect to the target via an Ethernet link. The target uses QNX or RedHawk Linux as the RTOS for fast simulation or for applications where real-time performance is required [41].

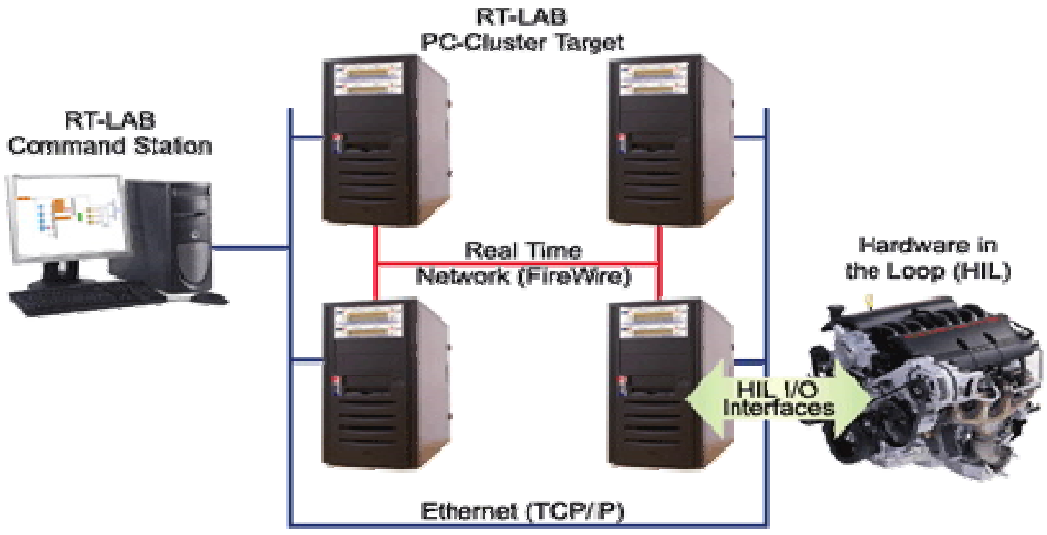

Figure 3-3. RT-LAB Distributed Target Configuration [41]

The distributed configuration allows for complex models to be distributed over a cluster of multi-core PCs running in parallel. The target nodes in the cluster communicate with each other with low latency protocols such as FireWire, SignalWire or InfiniBand, fast enough to provide reliable communication for real-time applications. The real-time cluster is linked to one or more host stations through a TCP/IP network. Here again, the cluster of PCs can be used for Real-Time applications (using QNX or RedHawk Linux), or fast simulation of complex systems (using QNX, RedHawk or Windows). RT-LAB PC-cluster targets are designed for flexible and reconfigurable mega-simulation. The user can build and expand the PC-cluster as needed, then redeploy the PCs for other applications when the simulation is done. RT-LAB can accommodate up to 64 nodes running in parallel [41].

Generally speaking, RT-LAB provides tools for running simulation of highly complex models on a network of distributed run-time targets, communicating via ultra low-latency technologies, in order to achieve the required performance. In addition, RT-LAB's modular design enables the delivery of economical systems by supplying only the modules needed for the application in order to minimize computational requirements and meet customers' price targets. This is essential for high-volume embedded applications [40]. RT-LAB allows the user to readily convert Simulink models, via Real-Time Workshop (RTW), and then to conduct Real-Time Simulation of those models executed on multiple target computers equipped with multi-core PC processors. This is used particularly for Hardware-in-the-Loop (HIL) and rapid control prototyping applications. RT-LAB transparently handles synchronization, user interaction, real-world interfacing using I/O boards and data exchanges for seamless distributed execution [41].

Opal-RT provides a complete range of Real-Time Digital Simulators and control prototyping systems for power grids, power electronics, motor drives. Opal-RT Real-Time Digital Simulators, control prototyping systems and motor kits help the user design and test the controllers for a wide variety of applications including small power converters, hybrid electric drives, large power grids and renewable energy systems. All the DG, short-term storage, load, transmission line models are built in Matlab/Simulink. RT-LAB is fully integrated with Matlab/Simulink. Thus all model preparation for RT-LAB is done with established dynamic system modeling environments, which allows the users to leverage experience in using these tools. Also with RT-LAB's visualization and control panel, the user can dynamically select signals to trace, modify any model signal or parameter in real-time.

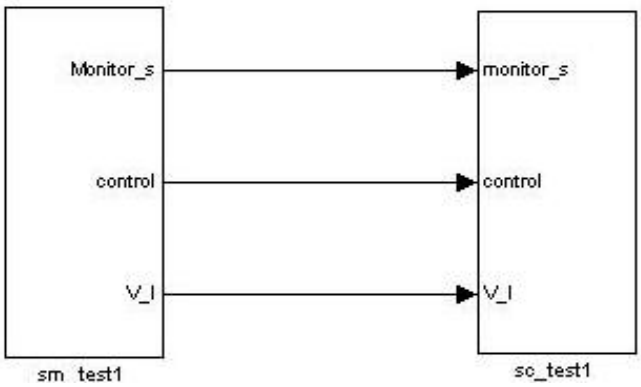

Figure 3-4. A overview of RT-LAB subsystems

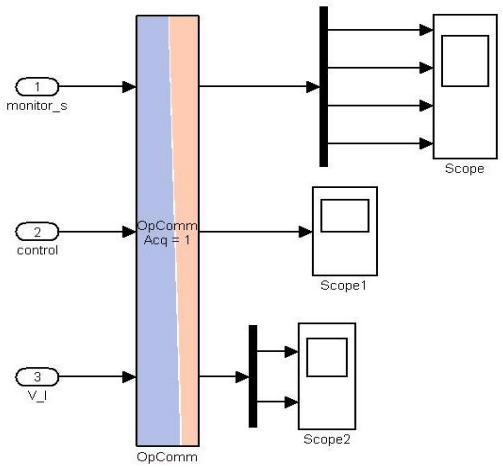

Figure 3-5. A typical RT-LAB SC subsystem

Once the Matlab/Simulink models are built and tested well, all the top-level subsystems must be named with a prefix identifying their functions. The console subsystem "SC_" is the subsystem operating on the command station that enables the interaction with the system. It contains all the Simulink blocks related to acquiring and viewing data like the scope block. Only one console subsystem is run inside the whole system. The master subsystem "SM_" contains the computational elements of the model. There is always only one master subsystem in the model. The slave subsystem "SS_" contains the computational elements of the model when distributing the processing across multiple nodes. RT-LAB maximizes parallelism when computation nodes exchange only priority signals. For this, the master and slave subsystems must compute and send their outputs before they read their inputs. At the execution time, RT-LAB provides seamless support for inter-processor communication and interact with the simulation in real-time from the host station using TCP/IP.

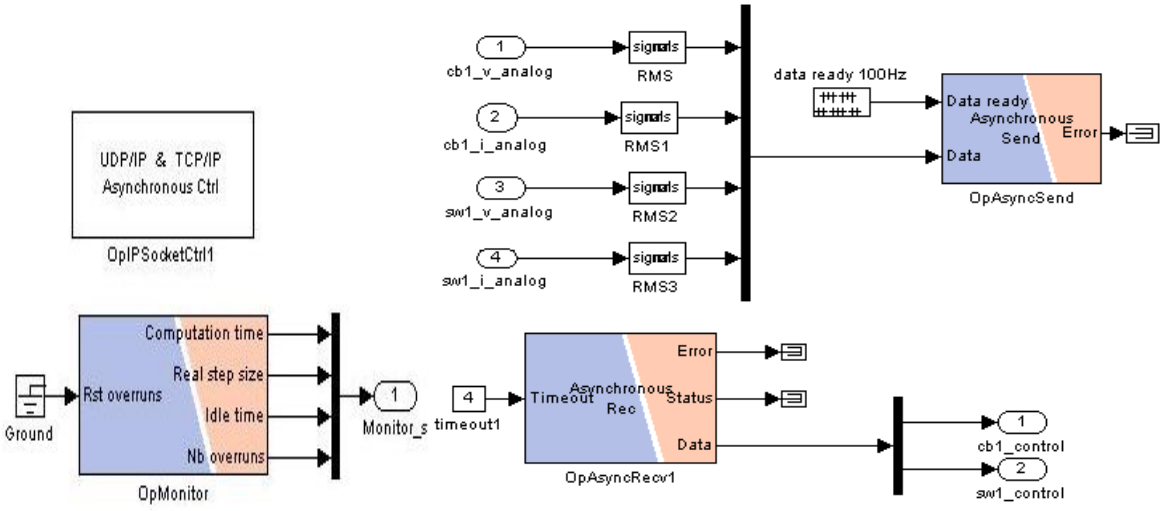

Figure 3-6. UDP/IP TCP/IP communication implemented in RT-LAB

3.2 PSS/E Interface

A dynamic co-simulation with a power system planning package PSS/E has been studied. An interface between PSS/E and Matlab/Simulink allows models created in the Matlab/Simulink to be co-simulated as part of a network in PSS/E. A GE 3.6 MW wind turbine has been implemented in IEEE 3-bus test system.

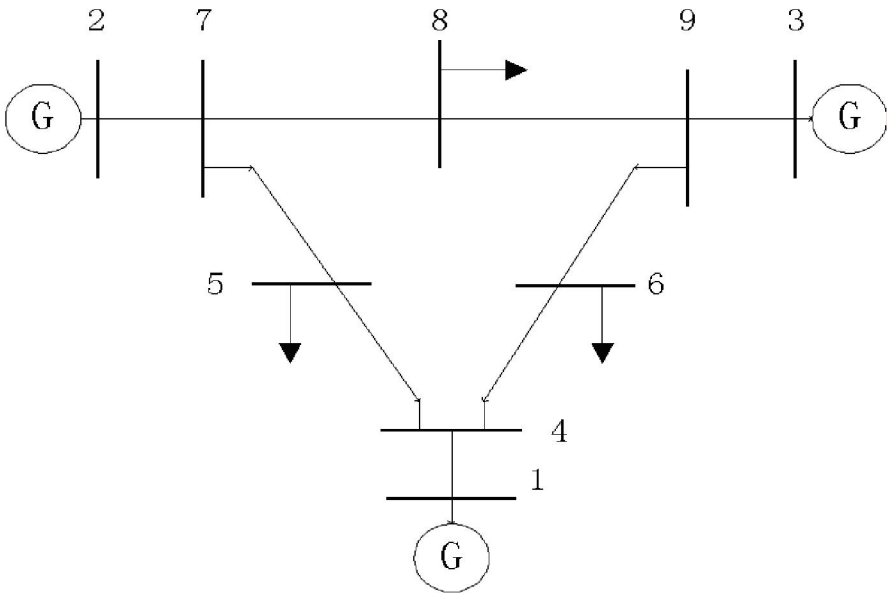

Figure 3-7. IEEE 3-bus test system

In PSS/E new version, we can create Matlab models of controllers and governors and interface it directly with PSSE. To optimize the design of distributed generations and energy storage, a co-simulation has been developed to evaluate various Microgrid components. This simulation has been implemented in IEEE 23-bus test system, which is shown in Figure 3-8. This test system has 23 buses, 6 machines, 8 loads and 34 branches. The total generated power is 3258.7 MW and the total load is 3200 MW. The detailed simulation results will be presented in a pending publishing.

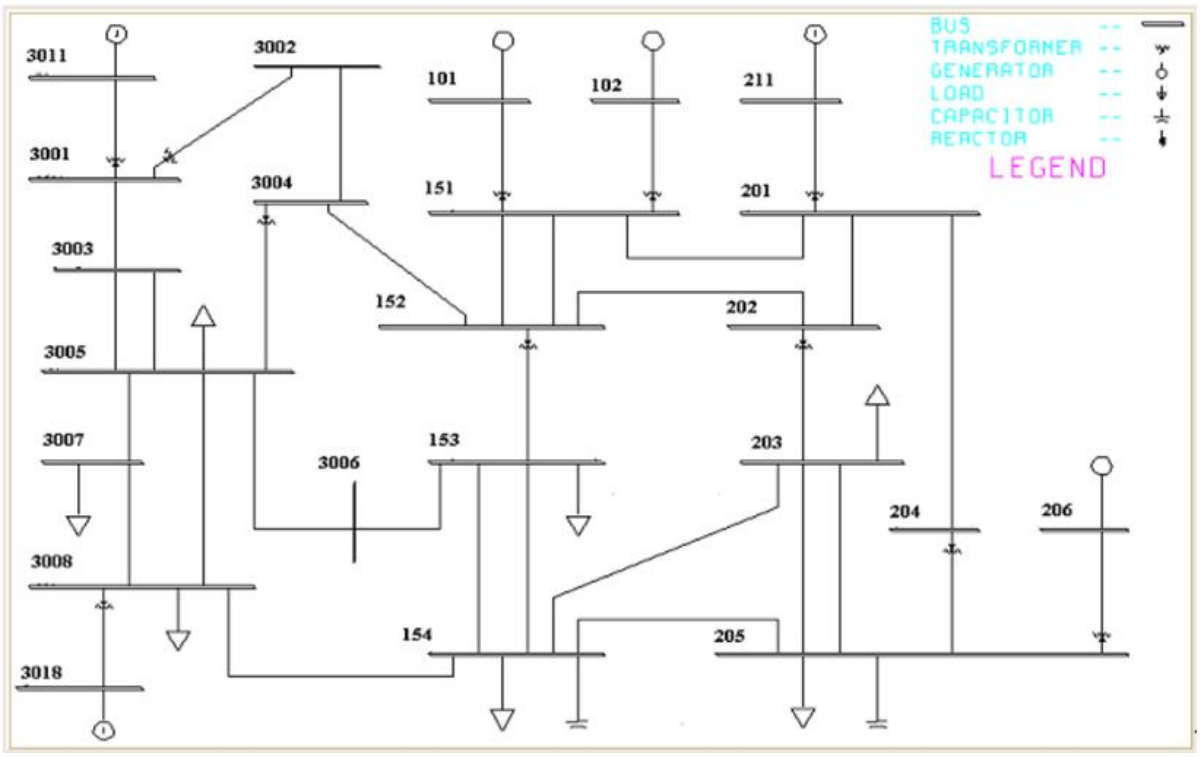

Figure 3-8. IEEE 23-bus test system

3.3 PLECS

In system modeling chapter, many complex components are studied and designed. A lot of power electronic technologies are incorporated in Microgrid system modeling and simulation. The complicated non-linear behavior of power electronic devices becomes a big challenge. Simulation of modern electrical systems using power electronics has always been a challenge because of the nonlinear behavior of power switches, their connection to continuous sub-systems

and the design of discrete-time control [42]. Many simulation platforms have been developed in the past decades. Although the models built in Matlab/Simulink are tested well as expected, more efficient and faster simulation software are required in near future. Some of them tend to focus on the accurate simulations of detailed behaviors of power electronics devices based on their own libraries, such as PSCAD (Professional's tool for Power Systems Simulation), CASPOC (Power Electronics and Electrical Drives Modeling and Simulation Software), PSPICE (Design and simulate analog and digital circuits), PSIM (simulation software designed for power electronics, motor control, and dynamic system simulation) and so on.

But all the models have been built in Matlab/Simulink. Therefore, we are looking for a well suited tool for modeling the complex electrical circuits within the same software environment. PLECS, a new Simulink toolbox implemented as a circuit simulator will be briefly introduced. In PLECS toolbox and Matlab/Simulink co-simulation, the power electronics circuits can be simulated more accurately. A sample model is tested and selective simulation results are provided for a comparative study. The version of PLECS that has been analyzed is 2.2 developed by Plexim GmbH.

PLECS is a toolbox for high-speed simulations of electrical circuits within the Simulink environment. It is specially designed for power electronics systems, but is also a powerful tool for any combined simulation of electrical circuits and controls. Matlab/Simulink is typically good for different kinds of control loops. But it takes a long time to implement the electrical circuits which are modeled using mathematical expressions. The concept of ideal switches distinguishes PLECS from any other simulation program. Also it is able to access other Matlab/Simulink ordinary libraries.

In reference [43], the simulations results shows a comparison between Simulink-only modeling and a co-simulation modeling of the same PV inverter. A simulation model with an accurate PV string model has been implemented in PLECS in order to observe the interaction between the power electronics and the PV cell in co-simulation environment. The simulation results were obtained using the same control structure and the same parameters for the PV plant. A real time of one second has been simulated in 59 seconds using PLECS and about 3 minutes 46 seconds using Simulink transfer functions. Some of PLECS components are shown in Figure 3-9. PLECS include resistors, inductors, capacitors, switches, and voltage and current sources all taken as ideal components. Voltages and currents can be measured using special probes.

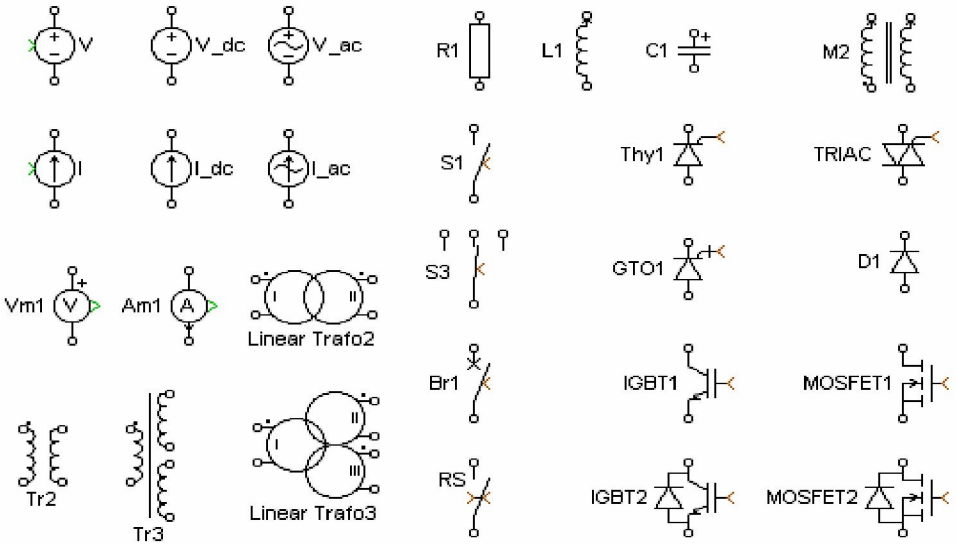

Figure 3-9. Some PLECS components

Thermal management is an important aspect of power electronic systems and is becoming more critical with increasing demands for compact packaging and higher power density. PLECS enables the user to embed the thermal design with the electrical design at an early stage in order to provide a cooling solution suitable for each particular application. Figure 3-10 a library with various thermal components that model the thermal behavior in Matlab/Simulink.

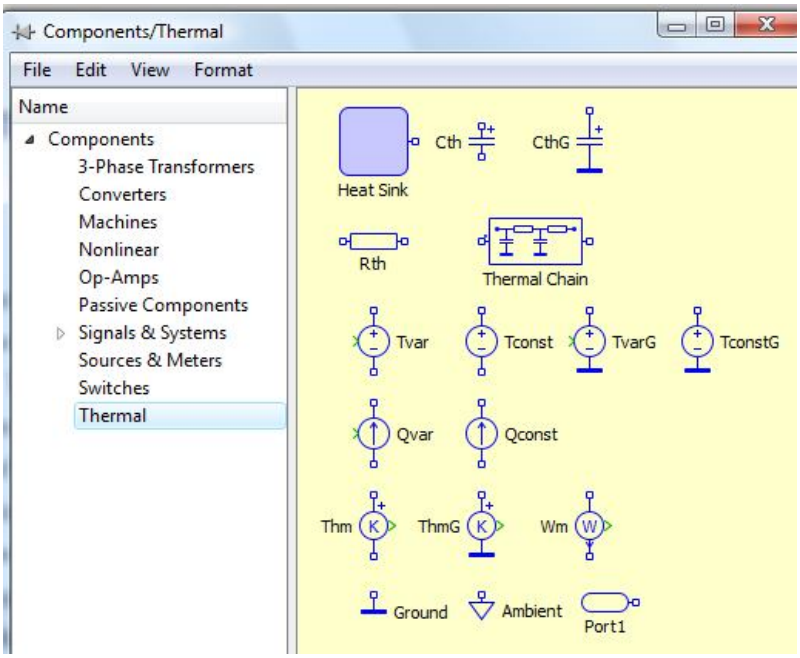

Figure 3-10. PLECS thermal components

In the previous chapter, the modeling of supercapacitors is discussed. One of the basic models is built using a standard capacitance with a constant value, that ignores the dynamic behaviors of the supercapacitors. In reference [37], the detailed modeling of a non-linear supercapacitor in PLECS and Matlab/Simulink is presented. The values of the capacitor changes during the simulation using control signals. The voltage over the components or the currents through them must be measured, in order to be passed through some calculation steps to find the component values. The component models are created using controlled voltage or controlled current sources. Reference [44] shows a PLECS implementation of PV string model as a non-linear current source, which is shown in Figure 3-12.

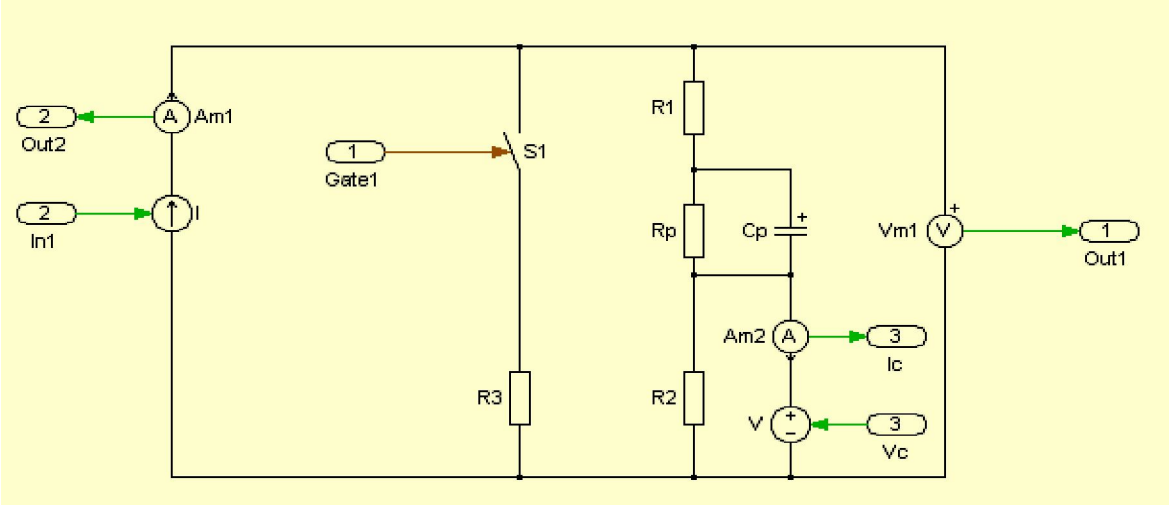

Figure 3-11. Electrical circuit of non-linear supercapacitor model implemented in PLECS [37]

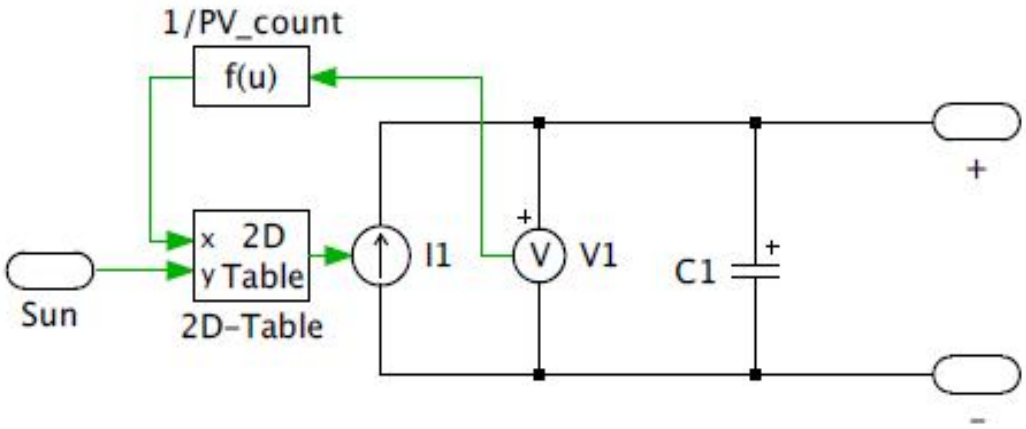

Figure 3-12. PLECS implementation of PV string model as a non-linear current source [44]

Chapter 4
Microgrid Planning

4.1 Introduction

As distributed generations and renewable energy are becoming the fastest growing segment of the energy industry, the technical issues and environmental impacts have to be studied and understood. The large number of small-scale Microgrid components with their own characteristics is a big challenge for Microgrid modeling and planning. Especially in term of renewable energy, the power output might be seasonal and non-dispatchable. A powerful simulator engine is necessary to overcome these challenges. The HOMER Micro-power Optimization Model is a computer model developed by the U.S. National Renewable Energy Laboratory (NREL) to assistant in the design of micro-source systems to facilitate the comparison of power generation technologies across a wide range of applications. HOMER models a power system's physical behavior and its lift cycle cost, which is the total cost of installing and operating the system over its life span. HOMER allows the modelers to compare many different design options based on their technical and economic merits. It also assists on understanding and qualifying the effects of uncertainty or changes in the inputs [45].

HOMER performs three principal tasks [45]: simulation, optimization, and sensitivity analysis. In the simulation process, HOMER models the performance of a particular micro power system configuration each hour of the year to determine its technical feasibility and life-cycle cost. In the optimization process, HOMER simulates many different system configurations in search of the one that satisfies the technical constraints at the lowest life-cycle cost. In the sensitivity analysis process, HOMER performs multiple optimizations under a range of input assumptions to gauge the effects of uncertainty or changes in the model inputs. Optimization determines the optimal value of the variables over which the system designer has control such as

the mix of components that make up the system and the size or quantity of each. Sensitivity analysis helps assess the effects of uncertainty or changes in the variables over which the designer has no control, such as the average wind speed or the future fuel price.

Typically renewable energy has high initial capital costs and low operating and maintenance costs, whereas conventional energy has low initial capital costs and high operating and maintenance costs. Given different cost characteristics, it is extremely difficult to compare the economics of each combination of components. HOMER models both conventional and renewable energy technologies.

4.2 Parameters for Wind-Diesel-Battery-PV System

The first case study explored the role of different generators to reduce the overall system cost. The case study focused on Ontario area, Canada, because the extensive energy data is public accessible. This section will model the economic and environmental performance of solar and wind energy on Ontario area of Canada. Figure 4-1 shows the geographical map of Ontario. After running the simulations in HOMER, it was able to identify the least cost system as a function of specific variables. A Wind-PV-Diesel hybrid system with battery storage is built in HOMER to test and analyze.

Figure 4-1. Geographical Map of Ontario, Canada [46]

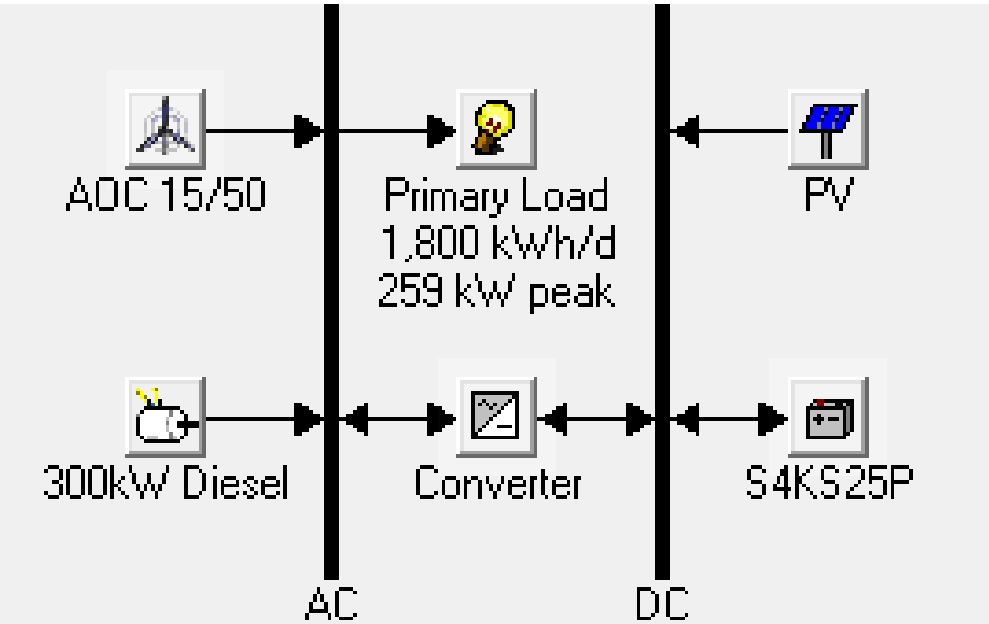

Figure 4-2. A Wind-Diesel-Battery-PV system serving an ac load implemented in HOMER

All the load data is originally coming from the public database established by The Independent Electricity System Operator (IESO). The IESO is a non-profit corporate entity established in 1998 by the Electricity Act of Ontario. The proposed hybrid power system is schematically shown in Figure 4-2. The components include wind turbines, PV panels, diesel genset, battery, primary load and converters (e.g. rectifiers, inverters). Figure 4.3 and Table 4-1 show the primary load profile used in this study.

Table 4-1. Primary AC load profile

Data source:	Synthetic
Daily noise:	9%
Hourly noise:	8%
Scaled annual average:	1,800 kWh/d
Scaled peak load:	259 kW
Load factor:	0.289

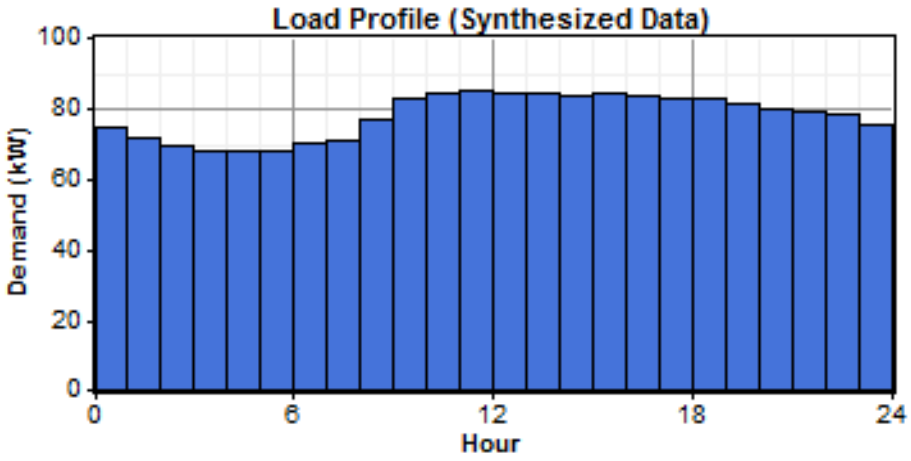

Figure 4-3. AC Load daily profile

PV capital cost and replacement cost are assumed as $6,000/KW, respectively. The operating and maintenance cost is relatively negligible. The lifetime of the photovoltaic panels is assumed to be 40 years. A derating factor of 90% approximates some uncertainties that reduce electrical output. The solar resource data of Ontario area ($43°23'N\ 79°59'W$) can be obtained from the NASA Surface Meteorology and Solar Energy [47]. The annual average solar radiation of Ontario area is about 3.59 $kwh/m^2/day$. Figure 4-4 and Table 4-2 show the solar resource profile, namely the clearness index and average radiation, over a period of 12 months.

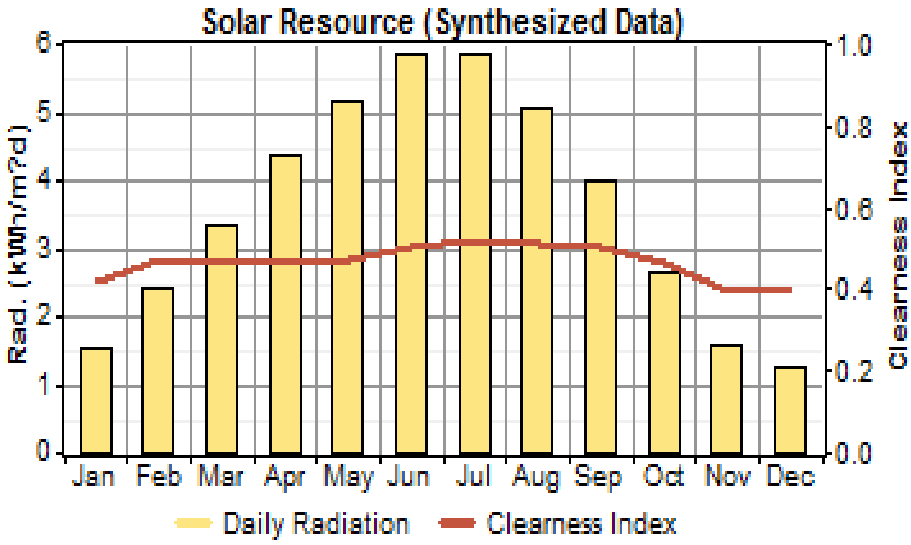

Figure 4-4. Solar Source Data (GMT -4:00)

Table 4-2. Clearness index and average radiation in Ontario over a period of 12 months

Month	Clearness Index	Average Radiation (kwh/m^2/day)
Jan	0.421	1.540
Feb	0.471	2.400
Mar	0.464	3.330
Apr	0.467	4.370
May	0.472	5.160
Jun	0.505	5.860
Jul	0.521	5.860
Aug	0.509	5.050
Sep	0.505	3.990
Oct	0.467	2.660
Nov	0.393	1.560
Dec	0.392	1.270

The wind statistics are obtained based on observations in the Ontario area taken between February 2007 - August 2009 daily from 7am to 7pm local time [48]. AOC 15/50 wind turbine is selected based on its power curve and capacity.

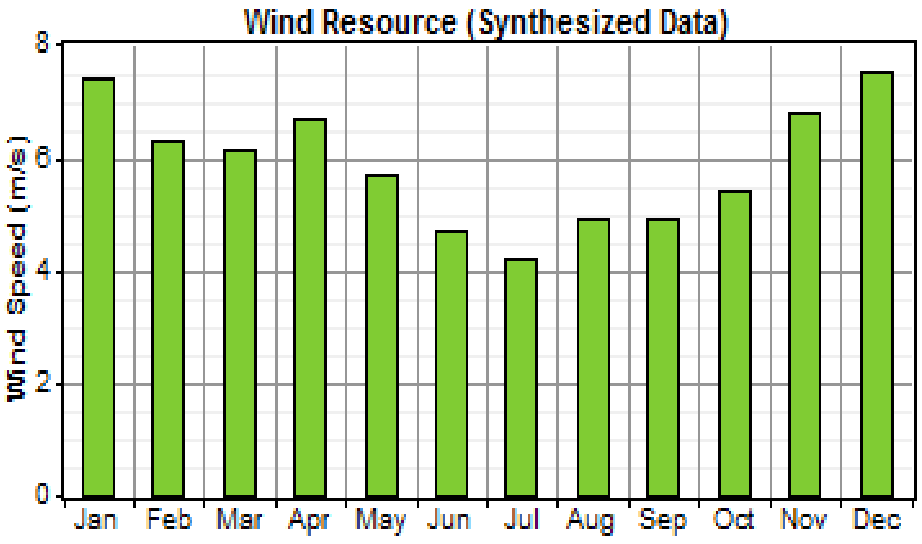

Figure 4-5. Wind statistics of Ontario, Canada over a period of 12 months

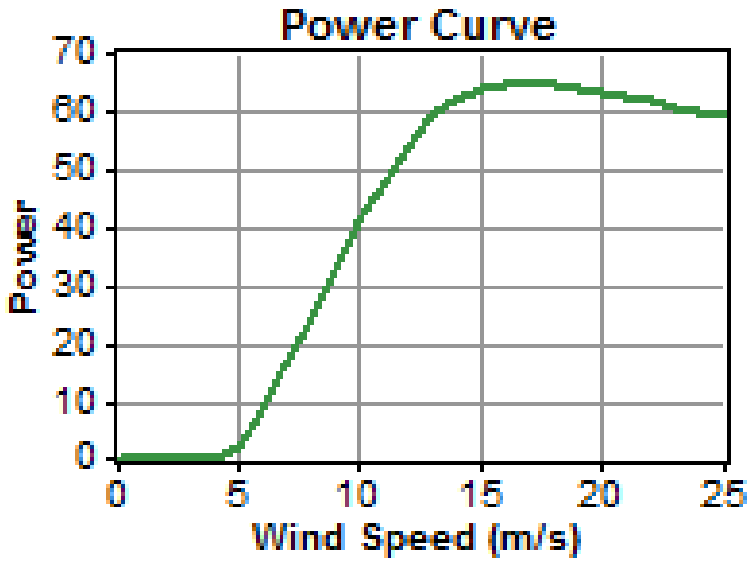

Figure 4-6. Power curve of AOC 15/30 wind turbine

The diesel price is roughly estimated at $0.7/L based on the market price. In order to evaluate the effect of fuel price changes on the optimal system configuration, the prices are also evaluated in increments of $0.1/L. In case study, the average diesel price ranges from $0.5/L - $1.0/L.

The inverter and converter efficiencies are both assumed to be 95%. In this case, the peak load is about 259 kW. A 300KW converter must be selected to meet the load for any hour. A series of converters below 300KW allows us to find out whether a smaller converter can reduce the overall system cost. Considering the available capacity and cost, Surrette 4KS25P is chosen. The battery provides bursts of power as a generator essentially when the load increases sharply at peak load period, while it absorbs the excessive energy at low load period. Basically an AC generator is not allowed to operate at less than 30% capacity. The capital cost and replacement cost are assumed to be $21,500/60KW and $20,000/60KW, respectively.

4.3 Economic Analysis in Microgrid Planning

The HOMER software, NREL's micropower optimization model, can evaluate a range of equipment options over varying constraints and sensitivities to optimize small power systems

[49]. In this chapter, an optimal combination of Microgrid components is found to meet the required electrical load with the least total net present cost (NPC). Economics play an important role in HOMER simulation. This single value NPC includes all costs and revenues that occur within the project lifetime, with future cash flows discounted to the present. The total net present cost includes the initial capital cost of the system components, the cost of any component replacements that occur within the project lifetime, the cost of maintenance and fuel, and the cost of purchasing power from the grid [45]. The NPC includes the initial cost, component replacements, maintenance, and miscellaneous costs [50].

$$NPC = C_0 + \frac{C_1}{1+r} + \frac{C_2}{1+r} + \frac{C_3}{1+r} + \cdots + \frac{C_n}{1+r} = C_0 + \sum_{n=1}^{t} \frac{C_n}{(1+r)^n} \qquad (4.1)$$

Where NPC is the net present cost; C_n is the total annual costs in any period; r is the interest rate; n is the project lifetime. At this moment, the annual interest rate is considered as 8%.

HOMER runs different cases with all the combinations of components. All the infeasible system configurations, which do not adequately meet the demand load, are automatically discarded.

The first fifteen most cost-effective system configurations of each combination are listed in Table I. Under the assumption of this analysis, adding wind turbines and battery banks would indeed reduce the life-cycle cost.

Table 4-3. Overall optimization table of the proposed hybrid system in Ontario, Canada

PV (kW)	15/50	D300 (kW)	S4KS25P	Conv. (kW)	Initial Capital	Operating Cost ($/yr)	Total NPC	COE ($/kWh)	Ren. Frac.	Diesel (L)	D300 (hrs)
	4	240	108	100	$ 734,800	226,674	$ 3,437,797	0.439	0.39	240,466	5,459
	5	240	144	100	$ 884,400	214,171	$ 3,438,301	0.439	0.47	218,091	4,931
	4	240	144	100	$ 774,400	223,887	$ 3,444,163	0.440	0.40	234,727	5,320
	5	240	108	100	$ 844,800	218,210	$ 3,446,866	0.440	0.46	225,272	5,106
	5	240	180	100	$ 924,000	211,629	$ 3,447,593	0.440	0.48	212,636	4,799
	4	240	180	100	$ 814,000	222,118	$ 3,462,672	0.442	0.40	230,190	5,209
	3	240	108	100	$ 624,800	239,773	$ 3,483,995	0.445	0.31	261,059	5,942
	4	240	72	100	$ 695,200	234,665	$ 3,493,488	0.446	0.38	251,670	5,734
	3	240	144	100	$ 664,400	238,014	$ 3,502,620	0.447	0.31	256,540	5,830
	5	240	72	100	$ 805,200	226,813	$ 3,509,855	0.448	0.45	237,015	5,392
100	4	240	144	100	$ 1,374,400	179,089	$ 3,509,968	0.448	0.56	181,805	4,131
100	4	240	180	100	$ 1,414,000	175,925	$ 3,511,834	0.448	0.56	175,638	3,982
	3	240	72	100	$ 585,200	245,661	$ 3,514,609	0.449	0.30	270,130	6,163
100	3	240	144	100	$ 1,264,400	189,550	$ 3,524,715	0.450	0.49	199,334	4,541
100	3	240	108	100	$ 1,224,800	193,588	$ 3,533,259	0.451	0.48	206,495	4,717

In this case study, a hybrid system with 4 wind turbine generators, 240KW diesel generator, 108 batteries and 100KW converters is preferable when the fuel price is $0.7/L and the annual average wind speed is around 5m/s. The cost of energy (COE) is $0.439/KWh, which is less than any other system design. The COE is defined as the ratio between total annualized cost in dollars and the total electrical energy output in kW/h per year.

Figure 4-7 displays a typical daily power output (kW) of the wind generation in the simulation scenario correlated to hours of a day over a period of 12-month. It is shown that the power output begins to increase shortly after 7am until 11pm. Wind power output during the day steadily varies in the similar way and the output reaches its maximum in the middle of a day. Due to seasonal variations, wind power output begins decreasing during the month of June, July, August, September and early October. Accordingly, Figure 4-8 shows the diesel genset's daily power output over a given year. With the load following dispatch regimes, the power output from the diesel generator will be higher in summer to compensate for wind energy shortfalls to meet required power demands. In addition, Figure 4-9 and Figure 4-10 show the converter output power and the battery State-Of-Charge.

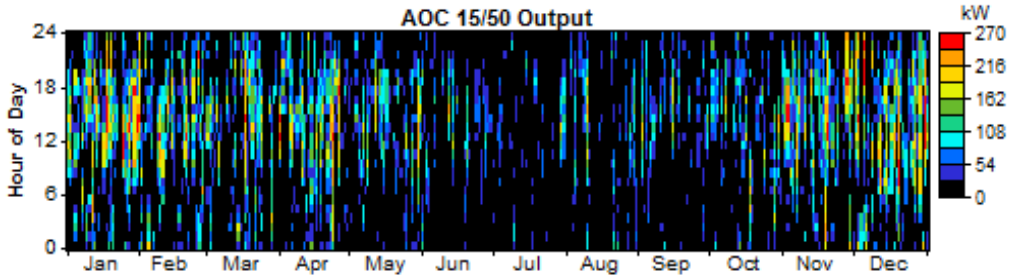

Figure 4-7. Daily power output of wind generators

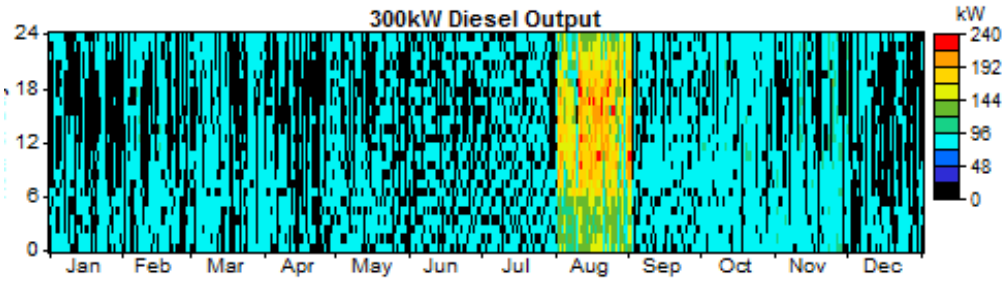

Figure 4-8. Daily power output of diesel genset

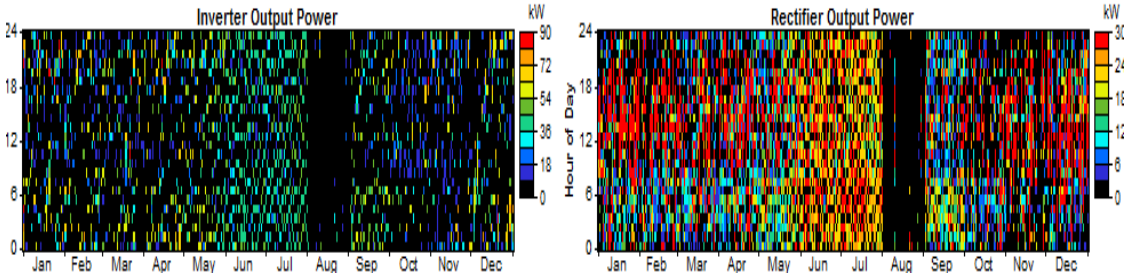

Figure 4-9. Daily inverter and rectifier output power

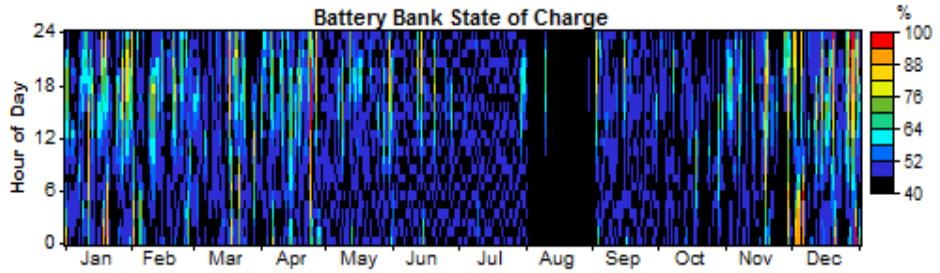

Figure 4-10. Daily battery state-of-charge

As the concept of Microgrid is becoming more pervasive, a mixed power system makes the best use of the different types of local generators. Obviously the electricity supply and demand is not always balanced at every instantaneous time. It tends to fluctuate depending on the time of the day and the time of a year. More specifically, overall wind speed changes in a predictable way with respect to time factors (e.g. day/night, seasons). Solar energy depends on the physical locations and the weather patterns. The energy storages implemented in Microgrid need to be able to store up sufficient electrical energy at low electricity consumption and provide the required power into the power system when demand increases. In this case study, the storage devices are represented by batteries.

The daily profiles of the excess electrical production over a period of 12 months are shown in Figure 4-11. The battery state-of- charge is affected by power output fluctuation. The storage device provides bursts of power as a generator essentially when the load increases sharply at peak load period, while it absorbs the excessive energy at low load period. The daily profiles of battery state-of-charge in Figure 4-12 show high correlations with the excess electrical energy.

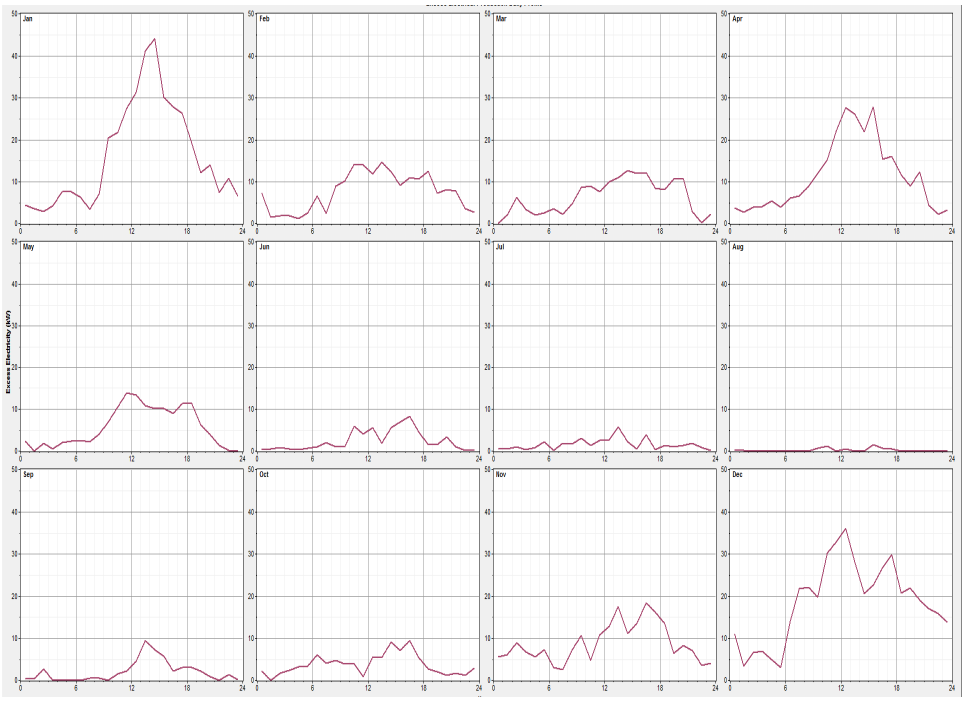

Figure 4-11. Excess Electrical Production Daily Profile Over a Period of 12 Months

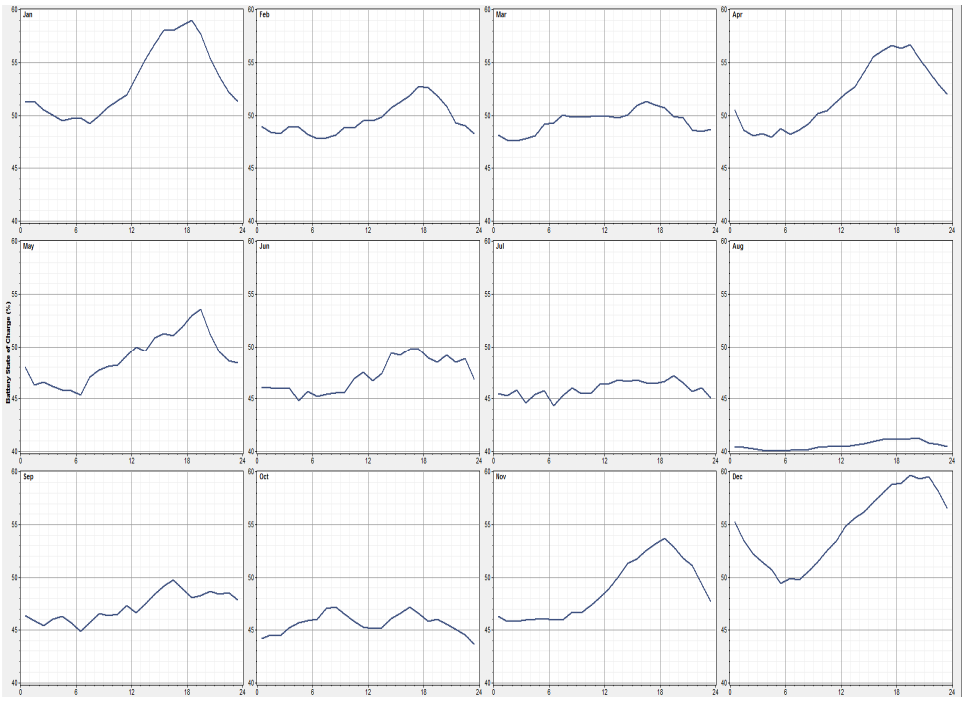

Figure 4-12 Battery State-of-Charge Daily Profile Over a Period of 12 Months

4.4 Sensitivity Analysis

At present, the market diesel price is roughly estimated at $0.7/L. In order to evaluate the effect of fuel price changes on the optimal system configuration, the prices are also evaluated in increments of $0.1/L. Thus the average diesel price ranges from $0.5/L - $1.0/L. Accordingly, the next question is coming up: how do changes in average wind speed and fuel price affect the optimal system configuration? The planners should consider this question especially in a long-term Microgrid planning. Sensitivity analysis are used in this paper to address this problem.

Figure 4-13 shows the result of the sensitivity analysis over a wide range of wind speed and diesel price. Regardless of the diesel price, Wind-Diesel-Battery systems are optimal when the annual average wind speed is no less than 5.5 m/s. At low wind speeds, the least-cost option changes to Diesel-Battery and finally diesel-only mode as the diesel price declines. Otherwise, the hybrid system with Wind-PV-Diesel-Battery is the optimal system type.

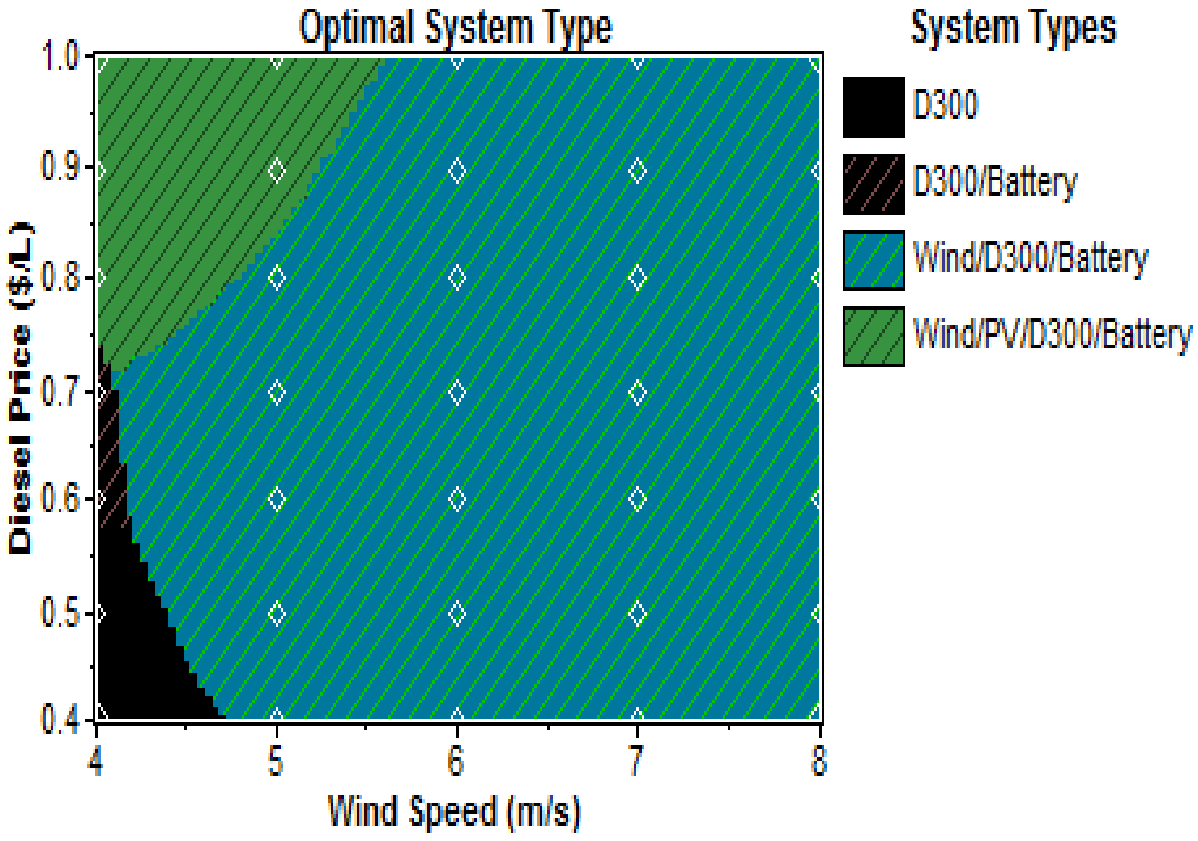

Figure 4-13. Sensitivity Analysis of Fuel Price and Wind Speed

On the Optimal System Type graph in Figure 4-13, we can see the results for all wind speeds and fuel prices. The optimal system configuration depends both on the wind speed and the fuel price. In performing the previous optimal analysis, it was assumed that the fuel price would be always $0.7/L over the project lifetime and the annual average wind speed remains the same. Obviously these assumptions might not be valid as time changes. We use sensitivity analysis to examine the effect of these uncertainties on the overall system performance.

Based on the simulation results, a energy planner might be informed to decide what type of distributed generators to use over a wide range of wind speeds and fuel price of each area. For example, at an annual average wind speed of 5.74m/s and the fuel price of $0.763/L, Wind-Diesel-Battery is the optimal configuration. At an annual average wind speed of 4.42m/s and the fuel price of $0.883/L, Wind-PV-Diesel-Battery outperforms any another combinations. At an annual average wind speed of 4.06m/s and the fuel price of $0.619/L, the optimal type changes to Diesel-Battery. But at an annual average wind speed of 4.22m/s and the fuel price of $0.523/L, Diesel-Only should be selected over the other systems.

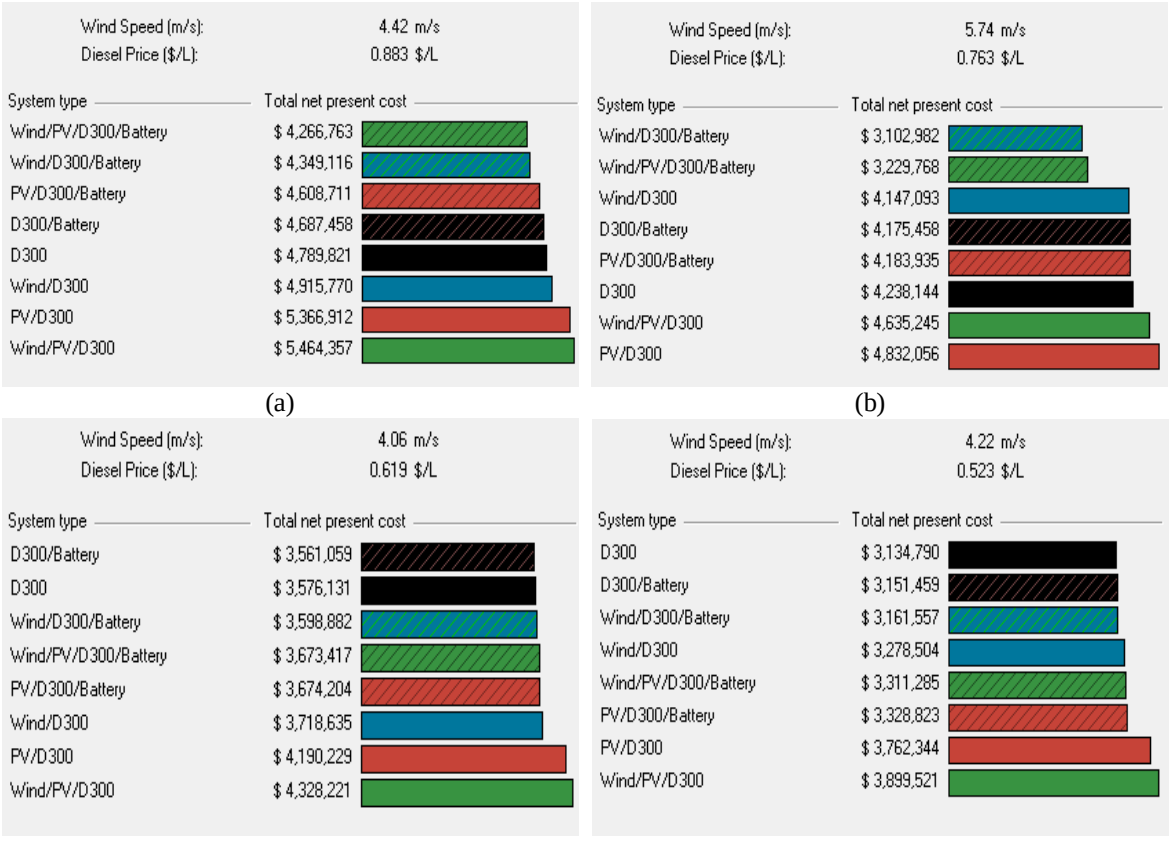

Figure 4-14. Optimal system configurations: (a) 4.42m/s,$0.883/L; (b) 5.74m/s,$0.763/L; (c) 4.06m/s,$0.619/L; (d) 4.22m/s,$0.523/L

The current annual average wind speed is 5.881m/s and the diesel price is approximate $0.78/L in the area of Ontario. At this point, Wind-Diesel-Battery is the optimal system. Five wind turbines, which reach the maximum limit of wind turbine capacity, are put into operation to reduce the overall system costs.

Table 4-4. Overall optimization table (5.881m/s and $0.78/L)

PV (kW)	15/50	D300 (kW)	S4KS25P	Conv. (kW)	Initial Capital	Operating Cost ($/yr)	Total NPC	COE ($/kWh)	Ren. Frac.	Diesel (L)	D300 (hrs)
	5	240	180	100	$ 924,000	173,587	$ 2,993,957	0.382	0.68	150,246	3,355
	5	240	144	100	$ 884,400	179,856	$ 3,029,110	0.387	0.66	159,028	3,568
	4	240	180	100	$ 814,000	186,496	$ 3,037,894	0.388	0.60	168,547	3,777
	4	240	144	100	$ 774,400	191,528	$ 3,058,294	0.390	0.59	176,019	3,961
	5	240	108	100	$ 844,800	187,837	$ 3,084,689	0.394	0.65	169,358	3,820
	4	240	108	100	$ 734,800	197,617	$ 3,091,301	0.395	0.58	184,584	4,170
	5	240	180	200	$ 1,014,000	175,071	$ 3,101,654	0.396	0.68	150,126	3,349
	5	300	180	100	$ 945,500	183,444	$ 3,132,993	0.400	0.67	160,688	2,963
	5	240	144	200	$ 974,400	181,333	$ 3,136,731	0.400	0.66	158,901	3,562
100	4	240	180	100	$ 1,414,000	144,692	$ 3,139,391	0.401	0.72	124,305	2,787
	4	240	180	200	$ 904,000	187,836	$ 3,143,868	0.401	0.60	168,279	3,767
100	5	240	180	100	$ 1,524,000	136,482	$ 3,151,490	0.402	0.77	110,960	2,478
	4	240	144	200	$ 864,400	193,015	$ 3,166,035	0.404	0.59	175,894	3,956
	3	240	144	100	$ 664,400	210,356	$ 3,172,813	0.405	0.49	200,498	4,532
100	4	240	144	100	$ 1,374,400	151,306	$ 3,178,669	0.406	0.71	133,469	3,009
	3	240	180	100	$ 704,000	207,774	$ 3,181,630	0.406	0.49	195,586	4,411
	5	300	144	100	$ 905,900	191,188	$ 3,185,747	0.407	0.65	170,424	3,152
	4	300	180	100	$ 835,500	197,578	$ 3,191,540	0.407	0.59	180,207	3,331
	4	240	72	100	$ 695,200	209,377	$ 3,191,943	0.407	0.56	198,100	4,500
	3	240	108	100	$ 624,800	215,352	$ 3,192,791	0.408	0.48	207,937	4,711
	5	240	72	100	$ 805,200	200,341	$ 3,194,185	0.408	0.63	183,703	4,168
	5	240	108	200	$ 934,800	189,500	$ 3,194,520	0.408	0.65	169,390	3,820
100	5	240	144	100	$ 1,484,400	143,520	$ 3,195,823	0.408	0.76	120,535	2,710
	4	240	108	200	$ 824,800	199,207	$ 3,200,265	0.408	0.58	184,556	4,169
100	3	240	180	100	$ 1,304,000	159,612	$ 3,207,308	0.409	0.64	144,708	3,262

To some extent, wind source is one of the most effective renewable energy in Ontario. According to the simulation results, as many wind generators as possible should be used. In fact, Ontario is at the forefront of wind generators in Canada with almost 1,100 MW of installed capacity on the transmission system. Seven large-scale wind farms are in operation. Ontario is well-positioned for considerable growth in wind generation with a good selection of sites across the province [51]. The following wind projects are currently under development. The simulation results reflect the actual scenarios in Ontario energy usages.

Table 4-5. Expected Date of Wind Farm in Ontario, Canada [51]

	Expected date of commercial operation
Byran Wind Project (64.5 MW)	2010
Gosfield Wind Project (50 MW)	2012
Greenwich Wind Farm (99 MW)	2011
Kruger Energy Chatham Wind Project (101.2 MW)	2011
Raleigh Wind Centre (78 MW)	2010
Talbot Wind Farm (99 MW)	2011

Figure 13 implies that PV energy does not seem to contribute to the least-cost configuration too much. An explanation is that the intensity of sunlight at ground level varies with latitude and the input data is coming from Ontario area of high latitude.

Solar radiation is unevenly distributed throughout the world. In term of latitude, we can roughly define three zone: the most favorable belt (15-35° N), the moderately favorable belt (0-15° N), and the least favorable belt (35-45° N) [13]. Ontario area is at a location of 43°N, which is included in the least favorable belt. As you can see in the solar source data of Ontario area, the average solar radiation value 3.59 $kwh/m^2/day$ is quite low. The cloudiness index is another important factor that can affect the solar radiation significantly. Although solar energy is one of the most popular renewable energy with an ample supply, it might not be a good option in this specific area due to the economic issues. Thus, more photovoltaic panels probably cannot offer financial benefits in the area of Ontario. An energy planner should take the uncertainties in key variables (e.g. wind speed and fuel price) into account.

4.5 Environmental Issues in Microgrid Planning

The growing need of reducing Carbon emissions makes the concept of Microgrid even more attractive. Microgrid has the ability to reduce emissions compared to centralized utility systems. The air emissions of the proposed Microgrid system on Ontario area of Canada are estimated in Table 4-6. The data can be used to explore the effect of emission penalties on Microgrid planning.

Table 4-6. Air emissions produced from the proposed system

Pollutant	Emissions (kg/yr)
Carbon dioxide	633,227
Carbon monoxide	1,563
Unburned hydocarbons	173
Particulate matter	118
Sulfur dioxide	1,272
Nitrogen oxides	13,947

In previous simulations, the emission penalties for a particular pollutant are not taken into consideration. However, under the latest update to the Canada federal climate-change plan, the price in all cases would start at $15 per ton of carbon and rise in steps to $65 by 2018 [52]. Thus we applied a specific carbon dioxide emission penalty $30/ton, $50/ton and $70/ton to reschedule the dispatchable energy source. The emission cost appears in addition to the operating and maintenance costs. For the systems with identical or similar configurations, carbon dioxide penalty index will be an important factor. As shown in Figures 4-15, 4-16 and 4-17, the renewable energy fraction keeps increasing as the carbon dioxide emission penalty changes from $30/ton to $70/ton. Accordingly, the renewable energy fraction goes up to 62.1% starting from 39.4%. Figures. 18 and 19 show the monthly average electric production with various carbon dioxide penalties. The environment efficiency is significant. All air emissions have been reduced by a considerable amount. Table 4-7 and 4-8 show the air emissions reduction with Carbon penalties. On the other hand, conventional generators like the diesel gensets are playing a less important role to obtain emission-reduction benefits.

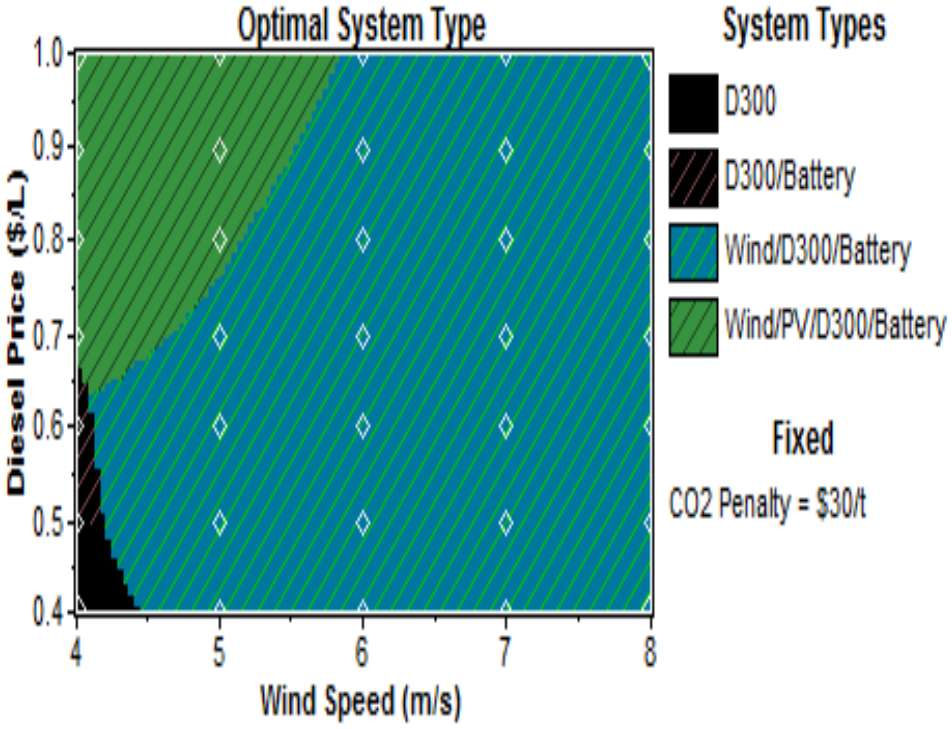

Figure 4-15. Optimal system configuration with $30/t carbon emission penalty

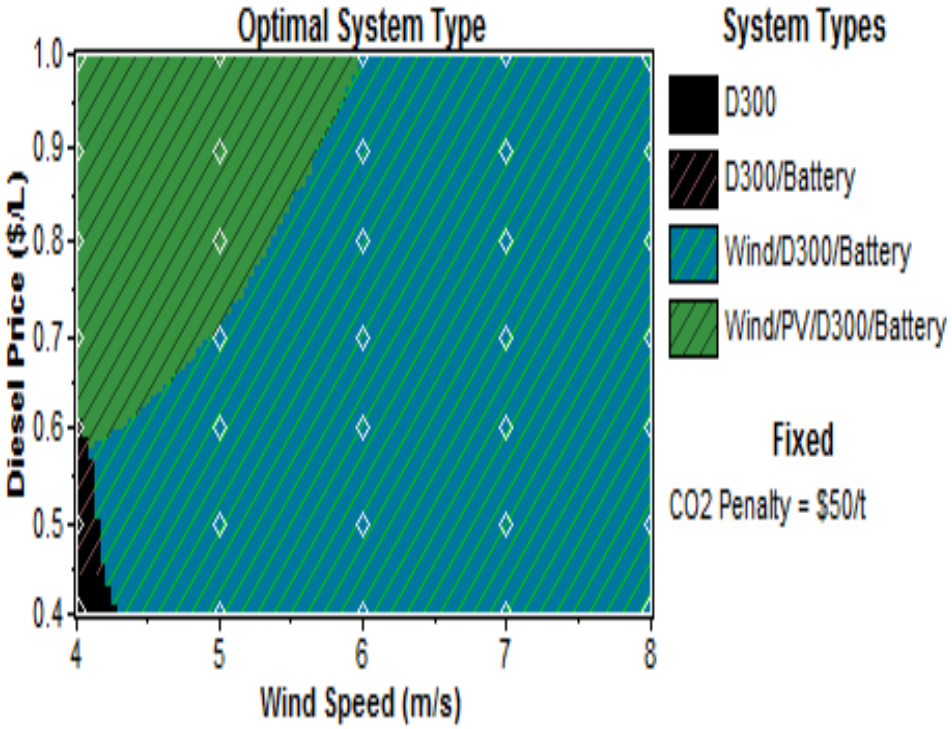

Figure 4-16. Optimal system configuration with $50/t carbon emission penalty

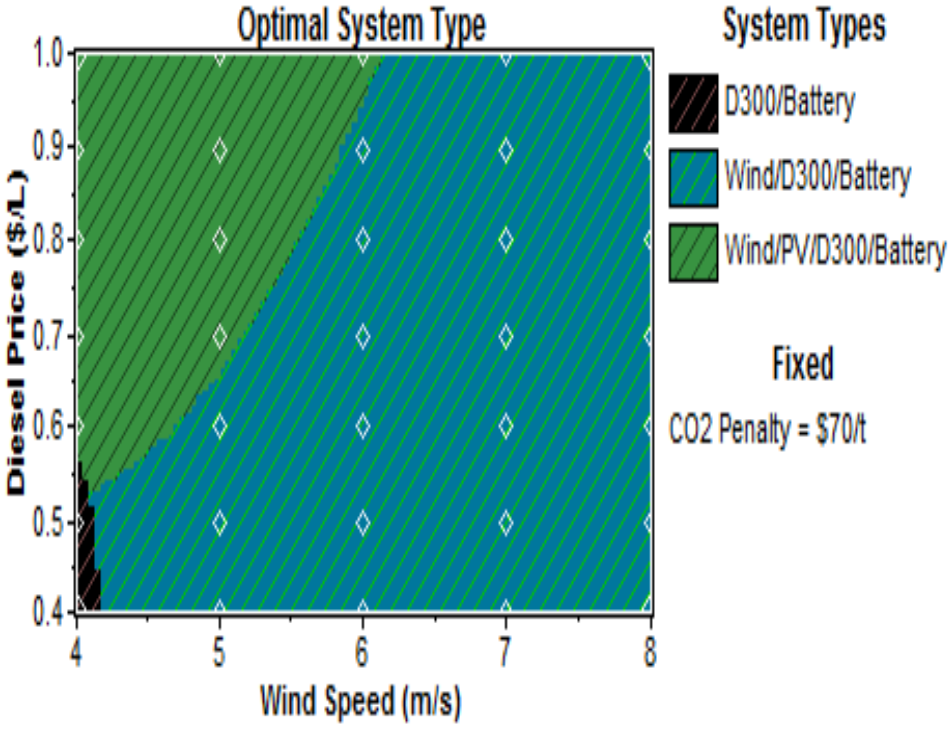

Figure 4-17. Optimal system configuration with $70/t carbon emission penalty

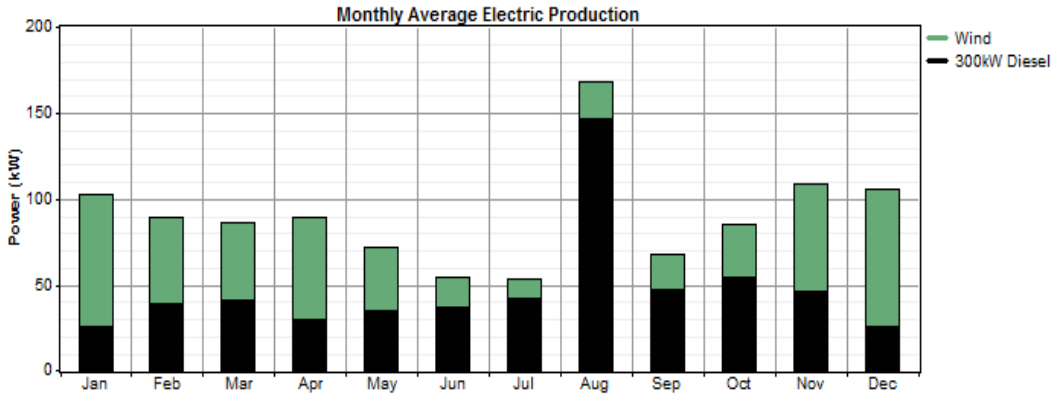

Figure 4-18. Monthly average electric production with $30/ton carbon penalty

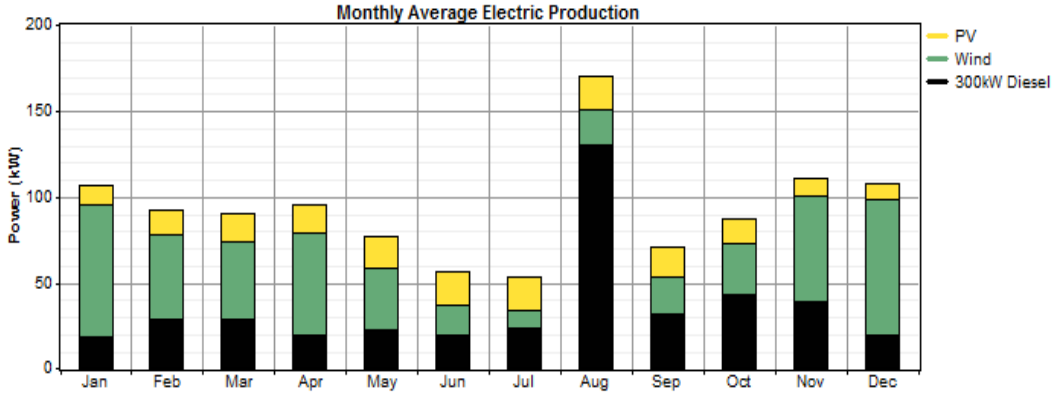

Figure 4-19. Monthly average electric production with $70/ton carbon penalty

Table 4-7. Air emissions with $30/t penalty

Pollutant	Emissions(kg/yr)	Reduction(%)
Carbon Dioxide	574,304	9.31
Carbon Monoxide	1,418	9.28
Unburned Hydrocarbons	157	9.25
Particulate Matter	107	9.32
Sulfur Dioxide	1,153	9.36
Nitrogen Oxides	12,649	9.31

Table 4-8. Air emissions with $70/t penalty

Pollutant	Emissions(kg/yr)	Reduction(%)
Carbon Dioxide	426,462	32.65
Carbon Monoxide	1,053	32.63
Unburned Hydrocarbons	117	32.37
Particulate Matter	79.4	32.71
Sulfur Dioxide	856	32.7
Nitrogen Oxides	9,393	32.65

In future, other emission factors (e.g. carbon monoxide, unburned hydrocarbons, particulate matter, sulfur dioxide, nitrogen oxides) will be specified to further take the environmental issues into account. More and more countries have developed emissions-trading schemes to impose a cost on energy generators that produce carbon dioxide, favoring renewable generation. For example, tax changes would give a financial incentive for installing distributed generations that mainly rely on renewable energy. Utilities are also highly encouraged to reduce carbon emissions so as to obtain financial benefits from the long-term view. Eventually, the customers will be highly encouraged to switch to the most efficient forms of energy generation with less carbon emissions if the price of the carbon emissions is fully factored into the energy price.

Chapter 5
Demand Side Management

5.1 Introduction

Demand Response (DR) is defined by Department of Energy (DOE) as “Changes in electric usage by end-use customers from their normal consumption patterns in response to changes in the price of electricity over time, or incentive payments designed to induce lower electricity use at times of high wholesale market prices or when system reliability is jeopardized.” [53] In several published reports [54-55], DR is divided into two main categories:

Incentive Based Programs (IBP)

1. Direct Load Control (DLC)
2. Interruptible/Curtailable Programs (I/C)
3. Demand Bidding
4. Emergency Demand Response Program (EDRP)
5. Capacity Market Program (CAP)
6. Ancillary Services Market (A/S)

Time Based Programs (PBP)

1. Time-of-Use (TOU)
2. Real-time Pricing (RTP)
3. Critical Peak Pricing (CPP)
4. Extreme Day CPP (EDCPP)
5. Extreme Day Pricing (EDP)

In the following chapter, I will briefly introduce some DR methods I mentioned above and focus on Emergency Demand Response Program (EDRP), Time-of-Use (TOU) and Real-time Pricing (RTP).

Real-time Pricing (RTP) :

It is a dynamic price to reflect the real cost of electric energy cost. Utilities change the retail price hourly beads on the usage information received from customers. RTP programs are the most efficient and direct DR programs.

Time-Of-Use (TOU) Program:

Generally speaking, the electricity price will be cheap in the low load period, and will be high in the peak period. Thus the customers can adjust their consumption pattern with the various prices. TOU programs simplify the DR process, but limit the real role of market price.

Emergency Demand Response Program (EDRP):

Based on historical demand, price data, and short term load forecasting, ISO tries to reduce peak demand. The ISO tries to prevent occurring spike prices, by running the EDRP.[56] The ISO will pay large customers a significant amount of incentives if they can reduce their electricity consumption in the peak period. As a result, the peak load demand is cut to relieve the potential electricity shortage.

5.2 Time-Of-Use and Real-Time-Pricing

Figure 5-1 shows the relationship between electricity market price and demand elasticity. Obviously a small reduction on demand side can induce a huge reduction of electricity market price. The reason behind it is that the generation cost is extremely high during peak load period.

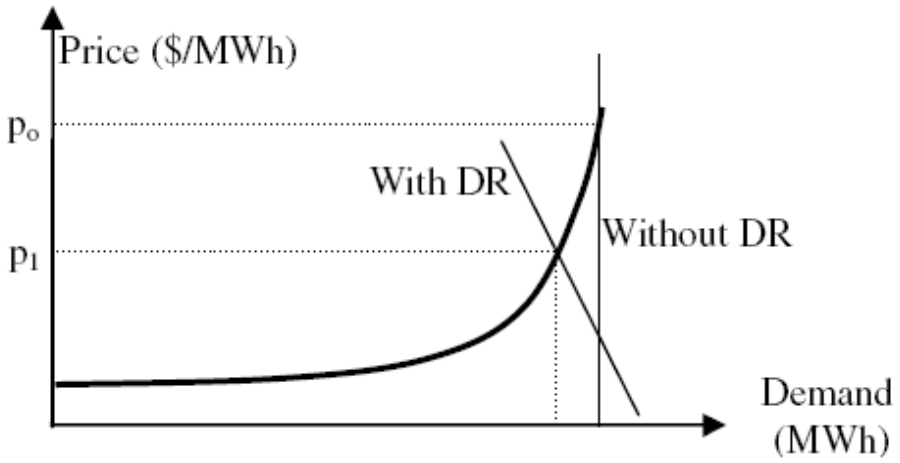

Figure 5-1. Simplified effect of DR on electricity market price [56]

Elasticity is defined as the demand sensitivity respect to the price [57]:

$$E = \frac{\partial d}{\partial p} = \frac{\Delta d / d_0}{\Delta p / p_0} \tag{5.1}$$

Where Δd and Δp are changes in demand and price respectively; d_0 and p_0 present the initial demand quantity and electricity price. The elasticity is an indicator of the effect of demand variation on the electricity price.

Basically there are two types of elasticity coefficients: self-elasticity (E_{ii}) and cross-elasticity (E_{jj}). Self-elasticity (E_{ii}) shows the effect of demand change on price in a single period. It is always a negative value. Cross-elasticity (E_{jj}) shows the effect of demand change on price in a multi-period. It is always a positive value.

$$E = \begin{pmatrix} E_{1,1} & \cdots & E_{1,24} \\ \vdots & \ddots & \vdots \\ E_{24,1} & \cdots & E_{24,24} \end{pmatrix} \tag{5.2}$$

In simulation part, hourly load profile is selected to model the demand variation on end-use customers' side. Thus the elasticity coefficients can be arranged in a 24 by 24 matrix. The diagonal elements are self-elasticity coefficients and the off-diagonal elements are cross-elasticity coefficients.

Considering the single period and multi period, the final model is presented by [58]

$$d(i) = \left\{ d_0(i) + \sum_{j=1}^{24} E_0(i,j) \cdot \frac{d_0(i)}{p_0(j)} \cdot \left[p(j) - p_0(j) + A(j) \right] \right\} \cdot \left\{ 1 + \frac{E(i) \cdot \left[p(i) - p_0(i) + A(i) \right]}{p_0(i)} \right\} \tag{5.3}$$

$i = 1, 2, ..., 24$

Where A(i) represents the incentive in the i-th hour ($/MWh).

The above equation shows how much should be the customer's demand in order to achieve maximum benefit in a 24 hours interval. The detailed model shows how the maximum customers' benefits can be achieved by changing the demand pattern. EDRP and RTP programs have been run to analyze the effect of demand variation on the electricity price.

In order to validate the effect of demand response on the load curve, different case study is selected using EDRP and RTP programs.

All the market data is coming from public database established by The Independent Electricity System Operator (IESO). The IESO is a non-profit, corporate entity without share capital established in 1998 by the Electricity Act of Ontario. In the first case study, two sets of data are selected randomly and tested. Both weekday (August 26, 1009) and weekend (August 31, 1009) data points are picked.

Table 5-1. Hourly Ontario energy price on August 26, 2009 [59]

Hour	HOEP Price	Data Source
1	15.46	DSO-RD
2	7.60	DSO-RD
3	13.59	DSO-RD
4	17.20	DSO-RD
5	24.69	DSO-RD
6	27.72	DSO-RD
7	28.90	DSO-RD
8	24.62	DSO-RD
9	27.87	DSO-RD
10	27.66	DSO-RD
11	30.45	DSO-RD
12	30.03	DSO-RD
13	27.38	DSO-RD
14	28.81	DSO-RD
15	29.24	DSO-RD
16	26.70	DSO-RD
17	24.16	DSO-RD
18	24.22	DSO-RD
19	24.30	DSO-RD
20	25.90	DSO-RD
21	25.19	DSO-RD
22	16.00	DSO-RD
23	21.47	DSO-RD
24	15.49	DSO-RD

Table 5-2. Hourly Ontario energy price on August 31, 2009 [59]

Hour	HOEP Price	Data Source
1	6.63	DSO-RD
2	7.32	DSO-RD
3	7.58	DSO-RD
4	2.99	DSO-RD
5	8.02	DSO-RD
6	3.25	DSO-RD
7	14.16	DSO-RD
8	25.26	DSO-RD
9	21.39	DSO-RD
10	19.07	DSO-RD
11	21.64	DSO-RD
12	21.75	DSO-RD
13	24.17	DSO-RD
14	24.17	DSO-RD
15	24.17	DSO-RD
16	24.71	DSO-RD
17	24.17	DSO-RD
18	25.08	DSO-RD
19	21.29	DSO-RD
20	26.14	DSO-RD
21	22.87	DSO-RD
22	22.87	DSO-RD
23	7.40	DSO-RD
24	2.54	DSO-RD

Where hour 1 represents the period from 0:00 to 1:00 (EST); HOPE price is the arithmetic average of the 12 five minute interval energy prices of the Ontario zone. The spot price is expressed in CAN$/MWh. DSO-RD - results of the Dispatch Scheduling process.

Table 5-3. Hourly Ontario demand on August 26, 2009 [60]

Ontario	Hour																							
	1	2	3	4	5	6	7	8	9	10	11	12	13	14	15	16	17	18	19	20	21	22	23	24
Ontario Demand	14127	13592	13213	13234	13813	14945	16224	17286	18059	18552	18860	18891	18904	18891	19004	19226	19093	18759	18204	18073	17859	16888	15330	14143

Table 5-4. Hourly Ontario demand on August 31, 2009 [60]

Ontario	Hour																							
	1	2	3	4	5	6	7	8	9	10	11	12	13	14	15	16	17	18	19	20	21	22	23	24
Ontario Demand	12253	11875	11622	12025	12726	13827	15075	16035	16709	17199	17538	17593	17519	17557	17724	17531	17480	17222	16849	16916	16676	15833	14499	13377

Based on the historical data of Ontario load profile in summer, the load curve is divided into two intervals as:

Peak load period: 7:00 a.m. – 10:00 p.m.

Low load period: 10:00 p.m. – 7:00 a.m.

Initially I considered 10 CAN$/MWh as an incentive in EDRP program and the potential for DR programs as 100%. Also Self-elasticity and cross-elasticity is set as table 1.

Table 5-5. Self Elasticity and Cross Elasticity

	Peak Period	Low Period
Peak Period	-0.1	0.01
Low Period	0.01	-0.1

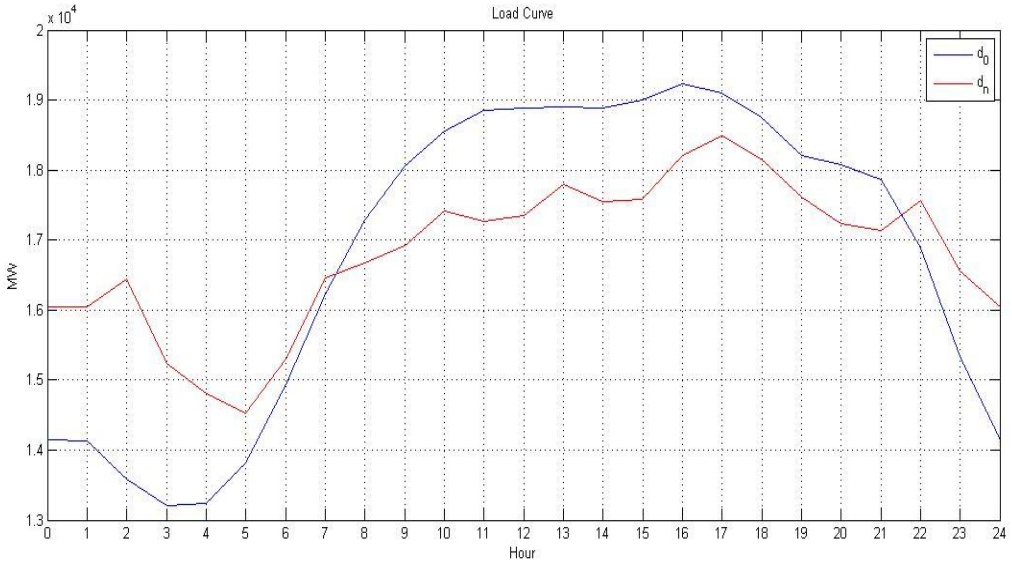

Figure 5-2. EDRP and RTP results (incentive 10 CAN$/MWh), August 26, 2009

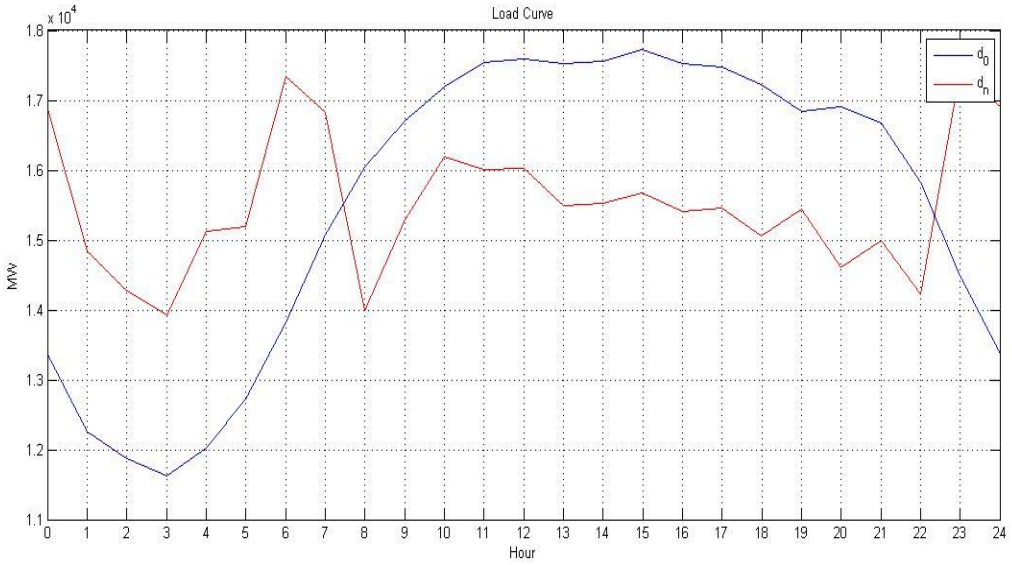

Figure 5-3. EDRP and RTP results (incentive 10 CAN$/MWh), August 31, 2009

As it could be seen in Fig. 5 and 6, the load curve after the optimization looks much flatter. The blue one is the original load curve. The load curve with DR programs is red colored. The customers have the abilities to reschedule the energy consumption. The peak demand has been reduced and loads are transferred from the peak period to low periods. It is obvious from RTP schedule that the customers benefit financially as long as the demand is flexible.

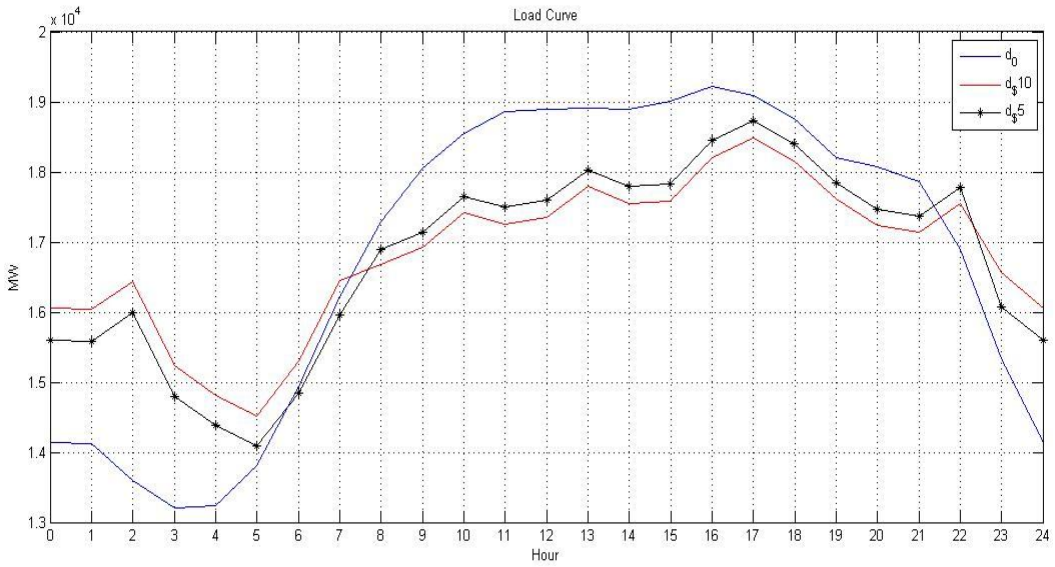

Figure 5-4. EDRP and RTP results with 5 CAN$/MWh and 10 CAN$/MWh incentives, Ontario, August 26, 2009

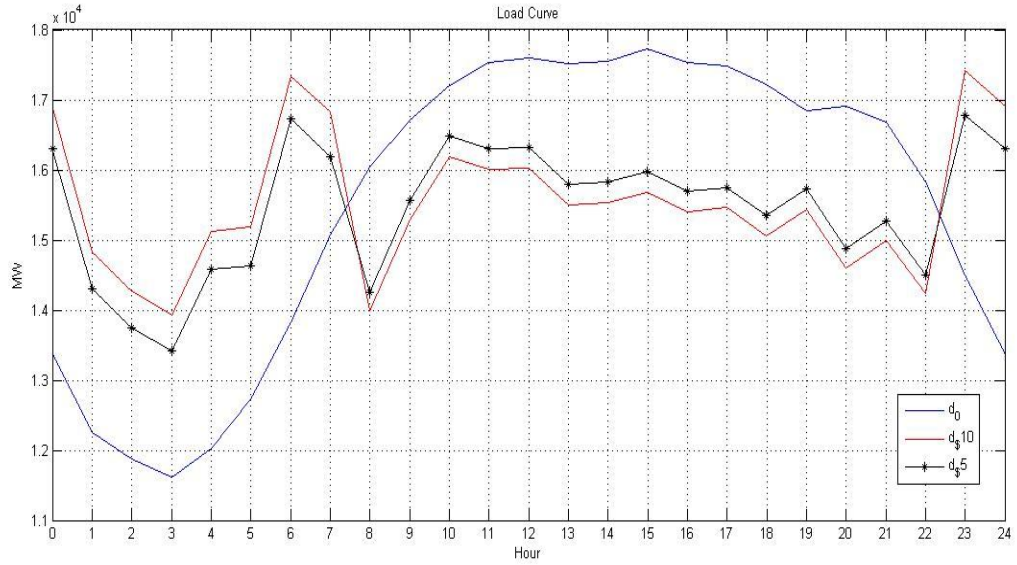

Figure 5-5. EDRP and RTP results with 5 CAN$/MWh and 10 CAN$/MWh incentives, Ontario, August 31, 2009

The load curve with a lower incentive is black colored and star marked. It is evident that the peak load reduction is smaller if a lower incentive is paid. So the customers are less interested in participating in this program.

For utilities, they also benefit financially by cutting down the extremely high generation cost in the peak period. In other words, the load demand at the peak period declines significantly

so as to reduce the generation cost. Accordingly, the power system reliability will be improved as well. The numerical calculations of case study are presented in table 2 and 3. In these cases, the maximum load variations are reduced from 6013 MW to 3969 MW and from 6102 MW to 3482 MW respectively.

Table 5-6. Numerical calculations of load demand with DR programs on August 26, 2009

	Before DR Application	After DR Application
Maximum Load Demand	19226 MW	18490 MW
Minimum Load Demand	13213 MW	14521 MW
Maximum Load Variation	6013 MW	3969 MW
$\frac{\text{Maximum Load Variation}}{\text{Average load}}$	35.62%	23.56%

Table 5-7. Numerical calculations of load demand with DR programs on August 31, 2009

	Before DR Application	After DR Application
Maximum Load Demand	17724 MW	17413 MW
Minimum Load Demand	11622 MW	13931 MW
Maximum Load Variation	6102 MW	3482 MW
$\frac{\text{Maximum Load Variation}}{\text{Average load}}$	39.19%	22.51%

An intelligent module for performing automated demand response at the customer side was proposed in Reference [61]. In this paper, an intelligent structure has been used for the DR module that receives the DR signal from the utility, and based on the market rates and other local policies/considerations, generates the final signal as to whether or not comply with the request.

Chapter 6

Protection in Microgrid

6.1 Introduction

In general, a Microgrid can be operated in two main modes: grid-connected mode and islanded mode. The microgrid is interfaced to the main power system by a fast semiconductor switch called static switch, (SS) [62]. To protect the microgrid loads, the Microgrid should be isolated from the grid as fast as possible to avoid the fault on the main grid's side during the connecting operating mode. The smallest possible section of the radial feeder should be isolated to eliminate fault inside the microgrid. In Chapter 1, the detailed modeling of protection part was not been taken into consideration. It has to be mentioned that plug-and-play functionality is highly recommended in view of Microgrid protection. One of significant advantages Microgrid can bring us is Micro-source can be placed at any place close to the load. Plug-and-play implies that a protection unit can be placed at any point on the existing system without rearrange the Microgrid structure. But random application of individual distributed generators can cause as many problems. The existing distribution systems are not originally designed for the operation of a large number of small scale generations. Thus, a number of technical problems associated with protection systems arise. It implies that protection is a part of Micro-source. A standard protection model is necessary to be built to enhance the entire system reliability. In addition, a standard block can be reproduced easily to reduce the operating cost and errors.

It is necessary to protect a Microgrid in both operations against all types of potential fault, e.g. (overcurrent, overvoltage, undervoltage, overfrequency and underfrequency). The philosophy for overcurrent protection remains the same for both operating modes. In reference [62], the relay protection implemented in a simple microgrid with sources in series is shown in Figure 6-1. The SS (static switch) separates the utility from the microgrid. The islanded part

contains two loads and the inverter based sources. The microgrid assumes that the sources have adequate ratings to meet the load demands while in island mode. This example shows two sources in series with impedances between the sources using a four-wire configuration with a common ground point and one source in parallel. Currently most of protection scenarios are based on current sensors. Basically the power can flow in either direction through current sensors when the distributed generations are added or removed instantaneously. But there are no bi-directional flows on most existing radial systems. A more subtle difference between Microgrid and traditional grids is that Microgrid will experience a significant change in short circuit capability when they switch from grid-connected to island operation. This change in short circuit capability will have a profound impact on the vast majority of protection schemes used in today's systems, which are based on short-circuit current sensing [63]. In the chapter of microgrid modeling, no special current limiting functions are implemented in Matlab/Simulink.

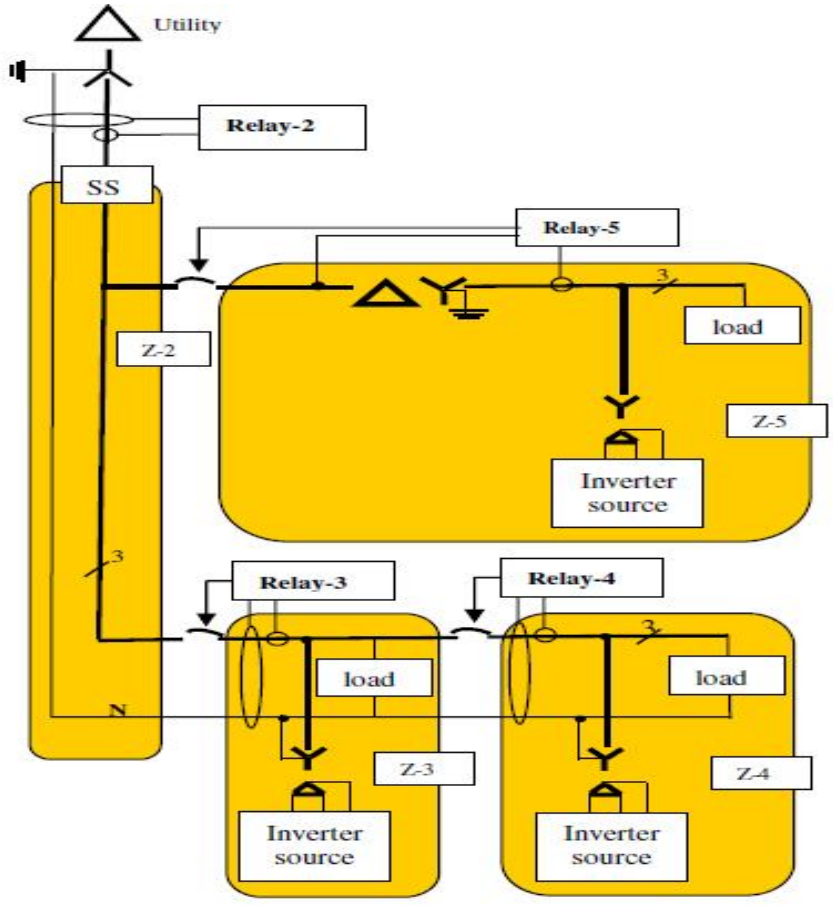

Figure 6-1. A simplified Microgird diagram with relay protection [62]

6.2 Overcurrent Protection

In this chapter, a protection scheme based on instantaneous overcurrent and time-delay overcurrent will be proposed and tested. In case study, a 1-phase fault current was applied in the different locations of the sample system. Existing power system protective devices are designed and applied for the fault conditions which normally prevail on a power system: maximum fault current levels of two to 20 or more times the maximum load to be served [63]. The sample system is based on the same concept. The time setting and other parameter setting are derived from the specific project requirements which will not be presented in this thesis. The simulation results are good as expected.

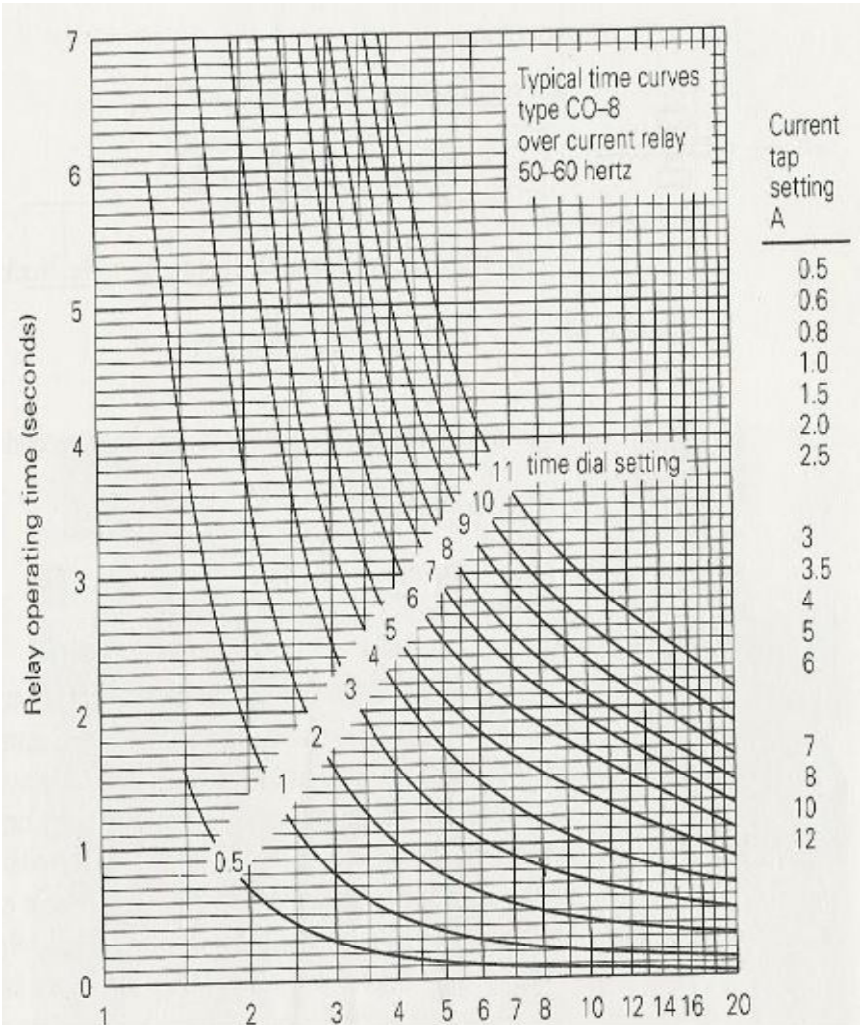

Figure 6-2. CO-8 time-delay overcurrent relay characteristics (Courtesy of Westinghouse Electric Corporation) [64]

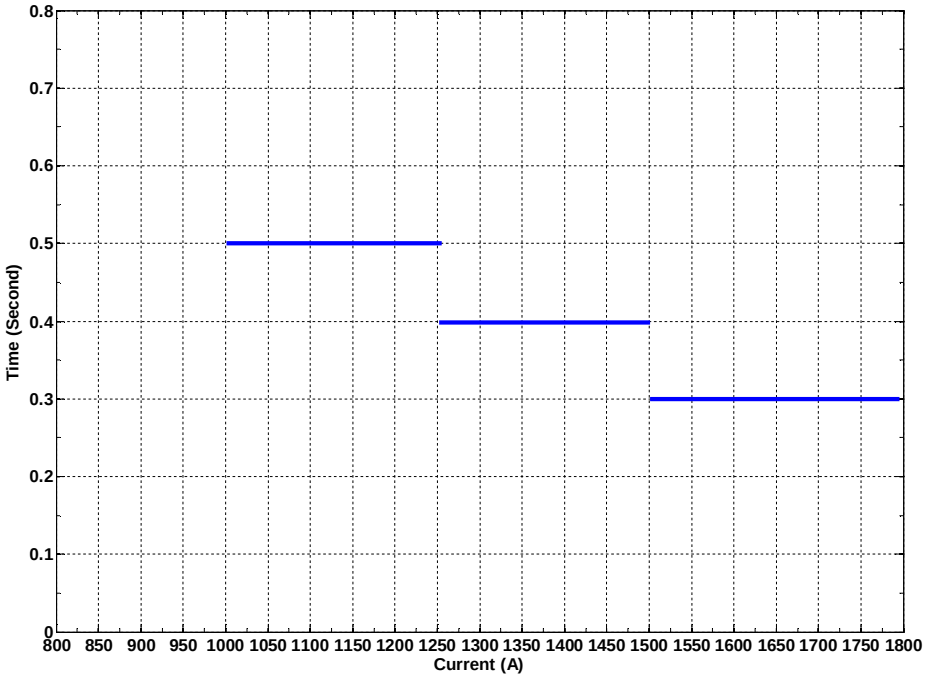

Figure 6-3. A simplified **t**ime-delay overcurrent setting

The protection devices have to accurately define the boundary between an abnormal and a normal operating mode of the power system. The speed of reaction ~~is~~ dependents on the specific properties of the relays. Figure 6-2 displays that there is an inverse relationship between the relay operating time and fault current. The greater the fault current is, the less time the time-delay overcurrent relay takes to take action. In practice, the shape of the curve totally depends on the specific manufacturer's curve for the relay. In simulation part, the test is implemented to verify the solution based on simulated IEDs. The high accuracy of time-delay setting is not the priority at this moment. Thus, to simplify the non-linear inverse relationship, it is common to linearize it by applying the first setting time intervals and applying some simple transformation to the model. The simplified time-delay overcurrent setting is shown in Figure 6-3.

The time-delay overcurrent protection devices are connected in series. The over-current protection devices closest to the fault location operate first and the breaker opens first. In other words, the tripping time is roughly proportional to the physical distance that they are from the disturbances. Although the upstream over-current protection devices are also able to detect the disturbances, they are in standby mode due to the prescribed delay time. In such coordination, if

the fault is not cleared by the first breaker, the upstream one should trip. As a result, if the fault is within the Microgrid, the protection coordinator isolates the smallest possible section of the radial feeder to eliminate the fault.

The proposed philosophy for time-delay overcurrent protection is good for both islanded and grid-connected operation. Note that the protection functions are important parts of the Microgrid and tend to have plug-and-play functionality. This work makes some progress, but further study is needed. Reference [63] states that the microgrid is not likely to appear as an infinite bus on the MV side of the LV transformer. In fact the apparent impedance of the microgrid source may be much higher than that of the transformer. Therefore the current may change by relatively small amounts as the fault moves further into the LV system. In an over-current coordinated system as mentioned above, the change from utility connected to an isolated microgrid has the potential to slow fault clearing and quite likely limit backup protection.

Chapter 7
Conclusion and Future Work

7.1 Conclusion

In this thesis, detailed analysis on different distributed generations and short-term storage is conducted to analyze the dynamic performance of Microgird components. All the models derived from theoretical equations or experimental data have been built in MATLAB/SIMULINK. A set of case studies were performed to validate the accuracy of each component. In addition to the extensive analysis of individual Microgrid components, several sample systems have been carried out to examine the dynamic behavior of the hybrid power as well as the steady-state behavior.

A detailed description of Microgrid models with moderate complexity is presented. Matlab/Simulink models of DG units, short-term storage, loads, utility grid and transmission lines are summarized as follows:

1. Load and Utility Grid:

- Utility grid
- Three phase constant load
- Three phase dynamic load

2. Transmission Line:
3. Distributed Generators:

- Photovoltaic Cell (PV Cell)
- Micro Gas Turbine
- Diesel Generator
- Wind Farm
- Fuel Cell

4. Short-term Storage:

- Flywheel
- Pumped Hydro Storage
- Battery Storage
- Supercapacitor

Some improvements on modeling and simulation are introduced to enhance the simulation performance. For example, the selected models are modified to fit a real-time simulator, which can run Simulink model down to 5 us. The interface developed between Matlab/Simulink and PSS/E allows the models to be used directly in PSS/E dynamic simulation. The developed models might be co-simulated by PLECS and Matlab/Simulink to reduce the running time.

Simulation results show a case study of an optimal microgrid configuration on Ontario area in Canada. Sensitivity variables are specified to examine the effect of uncertainties (e.g. diesel price and average wind speed), especially in a long-term planning. HOMER allows the modeler to compare many different design options based on their technical and economic merits. Many other factors have been taken into consideration such as the cost of Carbon emissions and thermal energy onsite when combined heat and power (CHP) is employed. The effect of air emission penalties on Microgrid planning is also well presented.

Also demand side management is playing an important role in the operation of Microgrid. It is obvious from RTP schedule that the customers benefit financially as long as the demand is flexible. For utilities, they also benefit financially by cutting down the extremely high generation cost in the peak period. In other words, the load demand at the peak period declines significantly so as to reduce the generation cost. Accordingly, the power system reliability will be improved as well. Based on raw data from Ontario area, case studies are carried out to investigate and validate the demand response methods.

Despite the significant benefits Microgrid can bring us, many technical challenges can reduce the operating efficiency. Microgrid protection is considered as one of important issues that has to be addressed. Finally, the philosophy for Microgrid protection, especially Time-delay overcurrent protection, has been briefly introduced in both gird-connected and islanding modes.

7.2 Future Work

Further analysis can be performed on the developed Microgrid models. More microgrid models, like thermal load, biomass genset, might be modeled later. The behavior of different sample systems consisting of DG and short-term storage can be investigated in more detail. The transient response to different disturbances is of my most interest in future work. A hybrid system with wind farm, pumped hydro storage and dynamic load are developing. Further work will also focus on the planning of small-scale generations and storage devices. The interface between various simulation platforms will be studied and implemented in future work.

References

[1] R. H. Lasseter, "Microgrids and distributed generation," *Journal of Energy Engineering-ASCE*, vol. 133, pp. 144-149, Sep 2007.

[2] "Pilot Microgrid Projects: CESI RICERCA DER Test Facility". [Online] Available: www.microgrids.eu/index.php?page=kythnos&id=6

[3] Department of Energy (DOE), GE Global Reseach, GE Energy (NRPS), GE C&I (Multilin), Rocky Research and National Renewable Energy Laboratory, "Microgrid Design, Development & Demonstration," March 2006.

[4] A. Akhil, R. Lasseter, C. Marnay, J. Stephens, J. Dagle, R. Guttromson, A. Sakis Meliopoulous, R. Yinger, and J. Eto, "Integration of Distributed Energy Resources: The CERTS Microgrid Concept," Energy Systems Integration Program, Public Interest Energy Research, California Energy Commission, 2002.

[5] B. Hurley, "Where does the wind come from and how much is there," presented at the *Claverton Energy Conference*, Bath, 2008.

[6] "Mapping the global wind power resource," [Online] Available: http://www.ceoe.udel.edu/windpower/ResourceMap/index-world.html

[7] "BP MSX 60-Watt Multicrystalline Photovoltaic Module," BP Solar, [Online] Available: http://www.directpower.com/products/modules/solarexbritishpetroleum/MSX60.pdf

[8] W. D. Soto, "Improvement and Validation of a Model for Photovoltaic Array Performance"," Master Thesis, Solar Energy Laboratory, University of Wisconsin-Madison, 2004.

[9] G. S. Stavrakakis and G. N. Kariniotakis, "A General Simulation Algorithm for the Accurate Assessment of Isolated Diesel - Wind Turbines Systems Interaction .1. A General Multimachine Power-System Model," *Ieee Transactions on Energy Conversion*, vol. 10, pp. 577-583, Sep 1995.

[10] B. Kuang, Y. Wang and Y. L. Tan, "An H controller design for diesel engine systems," *Power System Technology, International Conference Proceedings*, pp. 61-66, 2000

[11] S. Roy, O. P. Malik and G. S. Hope, "A Least-Squares Based Model-Fitting Identification Technique for Diesel Prime-Movers with Unknown Dead-Time," *Ieee Transactions on Energy Conversion*, vol. 6, pp. 251-256, Jun 1991.

[12] S. Roy, O. P. Malik and G. S. Hope, "An Adaptive-Control Scheme for Speed Control of Diesel Driven Power-Plants," *Ieee Transactions on Energy Conversion,* vol. 6, pp. 605-611, Dec 1991.

[13] S. Krishnamurthy, T, M. Jahns and R. H. Lasseter, "The Operation of Diesel Gensets in a CERTS Microgrid," *2008 Ieee Power & Energy Society General Meeting, Vols 1-11*, pp. 1829-1836

[14] A. Al-Hinai and A. Feliachi, "Dynamic Model Of A Microturbine Used As A Distributed Generator," in *34th Southeastern Symposium on system Theory*, Huntsville, Alabama, pp. 209-213, March, 2002.

[15] L. N. Hannett and A. Khan, "Combustion Turbine Dynamic-Model Validation from Tests," *Ieee Transactions on Power Systems,* vol. 8, pp. 152-158, Feb 1993.

[16] L. M. Hajagos and G. R. Berube, "Utility experience with gas turbine testing and modeling," *2001 Ieee Power Engineering Society Winter Meeting, Conference Proceedings, Vols 1-3*, pp. 671-677

[17] S. R. Guda, C. Wang and M. H. Nehrir, "A Simulink-based microturbine model for distributed generation studies," *37th North American Power Symposium, Proceedings,* pp. 269-274, 2005.

[18] F. Jurado and J. R. Saenz, "Adaptive control of a fuel cell-microturbine hybrid power plant," *Ieee Transactions on Energy Conversion,* vol. 18, pp. 342-347, Jun 2003.

[19] W. I. Rowen, "Simplified Mathematical Representations of Heavy-Duty Gas-Turbines," *Journal of Engineering for Power-Transactions of the Asme,* vol. 105, pp. 865-869, 1983.

[20] J. Wood, *Local Energy: Distributed generation of heat and power*. The Institution of Engineering and Technology, London, 2008.

[21] "Image description of Proton exchange membrane fuel cell," [Online] Availbale: http://en.wikipedia.org/wiki/File:PEM_fuelcell.svg

[22] R. F. Mann, J. C. Amphlett, M. A. Hooper, H. M. Jensen, B. A. Peppley and P. R. Roberge, "Development and application of a generalised steady-state electrochemical model for a PEM fuel cell," *Journal of Power Sources,* vol. 86, pp. 173-180, Mar 2000.

[23] J. C. Amphlett, R. M. Baumert, R. F. Mann, B. A. Peppley, P. R. Roberge and T. J. Harris, "Performance Modeling of the Ballard-Mark-Iv Solid Polymer Electrolyte Fuel-Cell .1. Mechanistic Model Development," *Journal of the Electrochemical Society,* vol. 142, pp. 1-8, Jan 1995.

[24] "NedStack PS100 Product Data," NedStack, [Online] Available: http://www.fuelcellmarkets.com/content/images/articles/ps100.pdf

[25] J. Padulles, G. W. Ault and J. R. McDonald, "An integrated SOFC plant dynamic model for power systems simulation," *Journal of Power Sources,* vol. 86, pp. 495-500, Mar 2000.

[26] Y. Zhu and K. Tomsovic, "Development of models for analyzing the load-following performance of microturbines and fuel cells," *Electric Power Systems Research,* vol. 62, pp. 1-11, May 28 2002.

[27] J. G. Slootweg, S. W. De Haan, H. Polinder and W. L. Kling, "Modeling wind turbines in power system dynamics simulations," *2001 Power Engineering Society Summer Meeting, Vols 1-3, Conference Proceedings,* pp. 22-26

[28] S. Heier, *Grid Integration of Wind Energy Conversion Systems*, John Wiley & Sons Ltd, 1998.

[29] M. Seyedi, "Evaluation of the DFIG Wind Turbine Built-in Model in PSS/E," Master of Science Thesis, the Programme of Electric Power Engineering, Division of Electric Power Engineering, Department of Environment and Energy, Chalmers University of Technology, Göteborg, 2009.

[30] R. Pena, J. C. Clare and G. M. Asher, "Doubly fed induction generator using back-to-back PWM converters and its application to variable-speed wind-energy generation," *Iee Proceedings-Electric Power Applications,* vol. 143, pp. 231-241, May 1996.

[31] V. Akhmatov, H. Knudsen, A. H. Nielsen, J. K. Pedersen and N. K. Poulsen, "Modelling and transient stability of large wind farms," *International Journal of Electrical Power & Energy Systems,* vol. 25, pp. 123-144, Feb 2003.

[32] V. Akhmatov and H. Knudsen, "An aggregate model of a grid-connected, large-scale, offshore wind farm for power stability investigations - importance of windmill mechanical system," *International Journal of Electrical Power & Energy Systems,* vol. 24, pp. 709-717, Nov 2002.

[33] N. W. Miller, J. J. Sanchez-Gasca, W. W. Price and R. W. Delmerico, "Dynamic modeling of GE 1.5 and 3.6 MW wind turbine-generators for stability simulations," *2003 Ieee Power Engineering Society General Meeting, Vols 1-4, Conference Proceedings,* pp. 1977-1983

[34] O. Tremblay, L. A. Dessaint and A. I. Dekkiche, "A generic battery model for the dynamic simulation of Hybrid Electric Vehicles," *2007 Ieee Vehicle Power and Propulsion Conference, Vols 1 and 2,* pp. 284-289

[35] I. P. GAJDŮŠEK, "Programable Laboratory Inverter and Space Vector PWM," Doctoral Dissertation, Dept. of Electrical Power Engineering, FEEC, VUT.

[36] "Electric double-layer capacitor" *Wikipedia,* (Cited on Oct 12, 2009) [Online] Available: http://en.wikipedia.org/wiki/Supercapacitor

[37] P. Johansson and B. Andersson, "Comparison of Simulation Programs for Supercapacitor Modelling," Master of Science, Department of Energy and Environment, Chalmers University of Technology, Gothenburg, Sweden, 2008.

[38] "Pumped Storage diagram at TVA's Racoon mountain," *wikipedia,* [Online] Available: http://en.wikipedia.org/wiki/File:Pumpstor_racoon_mtn.jpg

[39] C. Dufour and J. Belanger, "A PC-based real-time parallel simulator of electric systems and drives," *International Conference on Parallel Computing in Electrical Engineering,* pp. 105-113

[40] "RT-LAB Version 8.1 User Guide," Opal-RT, 2005.

[41] "RT-LAB Professional Overview," Opal-RT, (Cited on Oct 10, 2009) [Online] Available: http://www.opal-rt.com/product/rt-lab-professional

[42] M. P. Kazmierkowski, R. Krishnan, F. Blaabjerg and J. D. Irwin, *Control in Power Electronics Selected Problems,* 1st ed.: Academic Press 2002.

[43] M. Ciobotaru, T. Kerekes, R. Teodorescu and A. Bouscayrol, "PV inverter simulation using MATLAB/Simulink graphical environment and PLECS blockset," *IECON 2006 - 32nd Annual Conference on IEEE Industrial Electronics, Vols 1-11,* pp. 3375-3380

[44] J. Schonberger, "A single phase multi-string PV inverter with minimal bus capacitance," presented at the Power Electronics and Applications, 2009. EPE '09. 13th European Conference Barcelona, Spain, 2009.

[45] T. Lambert, P. Gilman and P. Lilienthal, "Micropower System Modeling with HOMER," in *Integration of Alternative Sources of Energy*. vol. 1, F. Farret and M. Simões, Ed. John Wiley & Sons Inc., 2006.

[46] "Map of Ontario, Canada," [Online] Available: http://ontario.alarmforce.com/blog/wp-content/uploads/ontario.jpg

[47] "NASA Surface Meteorology and Solar Energy," NASA, (Cited on Sep 10, 2009) [Online] Available: http://eosweb.larc.nasa.gov.sse

[48] "Wind Statistic in Ontaio area," *Windfinder*, (Cited on Sep 5, 2009) [Online] Available: http://www.windfinder.com/windstats/windstatistic_toronto_island.htm#

[49] T. Givler and P. Lilienthal, "Using HOMER® Software, NREL's Micropower Optimization Model, to Explore the Role of Gen-sets in Small Solar Power Systems Case Study: Sri Lanka," National Renewable Energy Laboratory, Rep. NREL/TP-710-36774, 2005.

[50] P. N. Bailey, O. Chotimongkol and S. Isono, "Demand Analysis and Optimization of Renewable Energy - Sustainable Rural Electrification of Mbanayili, Ghana," Master of Science Thesis, Dept. of Natural Resources and Environment, University of Michigan, April 2007.

[51] "Wind Power in Ontario," IESO, (Cited on Oct 1, 2009) [Online] Available: http://www.ieso.ca/imoweb/marketdata/windpower.asp

[52] P. Gorrie, "Ontario catches break on coal plants," in *TheStar*, ed, 2008.

[53] U. S. Department of Energy, *Energy Policy Act of 2005*.

[54] International Energy Agency, *Strategic Plan 2004-2009 for the IEA Demand-side Management program* .

[55] Federal Energy Regulatory Commission, *Federal Enery Regulatory Commission Survey on Demand Response and Time Based rate Programs/Tariffs and Advanced Metering Infrastructure Glossary*, General Information Section, FERC-727 and FERC-728

[56] M. Fahrioglu and F. L. Alvarado, "Designing incentive compatible contracts for effective demand management," *Ieee Transactions on Power Systems*, vol. 15, pp. 1255-1260, Nov 2000.

[57] A. H. Albadi and E. F. EI-Saadany, "Demand response in electricity markets: An overview," *2007 Ieee Power Engineering Society General Meeting, Vols 1-10*, pp. 1665-1669

[58] D. S. Kirschen and G. Strbac, *Fundamentals of power system economics*, 1 ed.: John Wiley & Sons Inc., 2004.

[59] The Independent Electricity System Operator (IESO), *Hourly Ontario Energy Price*. [Online] Available: http://www.iemo.com/imoweb/marketdata/hoep.asp

[60] The Independent Electricity System Operator (IESO), *Adequacy Report*. [Online] Available: http://www.iemo.com/imoweb/marketdata/adequacy.asp

[61] Q. B. Dam, S. Mohagheghi and J. Stoupis, "Intelligent Demand Response Scheme for Customer Side Load Management," *2008 Ieee Energy 2030 Conference*, pp. 158-164, 2008.

[62] H. Nikkhajoei and R. H. Lasseter, "Microgrid protection," *2007 Ieee Power Engineering Society General Meeting, Vols 1-10*, pp. 2123-2128, 2007

[63] W. E. Feero, D. C. Dawson and J. Stevens, "White Paper on Protection Issues of the Microgrid Concept," *Consortium for Electric Reliability Technology Solutions*, March 2002.

[64] J. D. Glover and M. S. Sarma, *Power System Analysis and Design*, 3rd ed.: Thomson-Engineering, Dec 2002.